

**CONTACT STRESS ANALYSIS OF THE NATIVE RADIAL HEAD
AND RADIAL HEAD IMPLANTS**

by

Sunghwan Kim

B. S. in Mechanical Engineering, Sogang University, Korea, 1999

M. S. in Mechanical Engineering, University of Southern California, 2006

Submitted to the Graduate Faculty of
Swanson School of Engineering in partial fulfillment
of the requirements for the degree of
Doctor of Philosophy

University of Pittsburgh

2014

UNIVERSITY OF PITTSBURGH
SWANSON SCHOOL OF ENGINEERING

This dissertation was presented

by

Sunghwan Kim

It was defended on

April 29, 2014

and approved by

Richard Debski, Ph.D., Associate Professor, Department of Bioengineering

Rakié Cham, Ph.D., Associate Professor, Department of Bioengineering

Patrick Smolinski, Ph.D., Associate Professor, Department of Mechanical Engineering

Dissertation Director: Mark Miller, Ph.D., Associate Research Professor, Department of

Mechanical Engineering

Copyright © by Sunghwan Kim

2014

**CONTACT STRESS ANALYSIS OF THE NATIVE RADIAL HEAD
AND RADIAL HEAD IMPLANTS**

Sunghwan Kim, PhD

University of Pittsburgh, 2014

A radial head fracture is a common fracture of the elbow joint most frequently caused by a fall on an outstretched arm. When the radial head is comminuted and reconstruction is not viable, radial head replacement is often the preferred option. There are basically two choices for the radial head implants: monoblock and bipolar. However, little research examining the performance of available radial head implants has been conducted. In this study, a finite element model for the intact elbow joint extracted from CT scans of a cadaveric elbow was created. The constructed FE model was validated with cadaveric experiments using Fuji pressure sensitive film. Then, two different implant models were generated by replacing the radial head with monoblock and bipolar implants. Contact stress and area for each model were calculated and compared under various loading conditions in the contact areas between the radial head and the capitellum of the humerus, and between the radial head and the radial notch of the ulna. A significant difference was found in both maximum contact stress and contact area between the native elbow and two types of implants. Contact stress for monoblock was higher than that for bipolar and vice versa for contact area. FE predictions showed the same pattern as measurements from Fuji analysis did although they overestimated the maximum contact stress and underestimated the contact area compared to the Fuji film experimental results.

TABLE OF CONTENTS

PREFACE.....	XII
1.0 INTRODUCTION.....	1
2.0 BACKGROUND	3
2.1 ANATOMY AND BIOMECHANICS OF THE ELBOW	3
2.1.1 Radial head.....	7
2.1.2 Capitellum	8
2.2 BONE	9
2.3 ARTICULAR CARTILAGE	10
2.4 LIGAMENT	12
2.5 RADIAL HEAD FRACTURES.....	12
2.6 TREATMENTS FOR RADIAL HEAD FRACTURE	13
2.6.1 Radial head excision	14
2.6.2 Open reduction and internal fixation [ORIF].....	14
2.6.3 Radial head arthroplasty	15
2.7 RADIAL HEAD IMPLANTS.....	16
2.8 FINITE ELEMENT ANALYSIS	19
2.8.1 Contact analysis.....	20
2.8.2 FE contact parameters	22
2.8.2.1 FKN and FKT.....	22
2.8.2.2 FTOLN and SLTO.....	23
2.8.2.3 PMAX and PMIN.....	23

2.9	FUJI PRESSURE SENSITIVE FILM.....	23
3.0	BACKGROUND REVIEW OF CONTACT ANALYSIS	25
3.1	JOINT PRESSURE AND CONTACT AREA	25
3.2	MONOBLOCK VS BIPOLAR.....	29
3.3	CLINICAL OUTCOMES OF RADIAL HEAD REPLACEMENT	31
3.4	FE MODELING OF HUMAN JOINTS	32
3.5	CARTILAGE THICKNESS.....	34
4.0	NATIVE RADIAL HEAD FE ANALYSIS	35
4.1	CREATION OF THE 3-D ELBOW MODEL	35
4.2	FE MODEL DESCRIPTION	37
4.3	CONVERGENCE.....	39
4.4	SENSITIVITY STUDY	47
4.4.1	Cartilage thickness	47
4.4.2	Cartilage material properties	55
4.4.3	Bone material properties.....	62
4.4.4	Ligament stiffness	66
5.0	RADIAL HEAD IMPLANT FE ANALYSIS	70
5.1	MONOBLOCK IMPLANT MODEL	71
5.2	BIPOLAR IMPLANT MODEL	75
6.0	VALIDATION OF THE FE MODEL	79
6.1	EXPERIMENTAL SETTING	79
6.2	FUJI FILM ANALYSIS.....	82
6.3	COMPARISON BETWEEN FE AND FUJI FILM	85

7.0	DISCUSSION	89
8.0	CONCLUSION AND FUTURE WORK	95
	APPENDIX A	97
	APPENDIX B	100
	BIBLIOGRAPHY	110

LIST OF TABLES

Table 1. Fuji film pressure ranges.....	24
Table 2. Material properties of the bone and soft tissues	39
Table 3. Number of elements for 6 different meshes.....	41
Table 4. Maximum contact stress and contact area calculated from Fuji film	84

LIST OF FIGURES

Figure 1. Anatomy of the elbow joint.....	4
Figure 2. Elbow flexion and extension	5
Figure 3. Supination and pronation of the forearm.....	5
Figure 4. MCL complex of the elbow joint	6
Figure 5. LCL complex of the elbow joint	7
Figure 6. Anatomy of the radial head	8
Figure 7. Anisotropic behavior of cortical bone in tension in four directions.....	10
Figure 8. Structure of articular cartilage.....	11
Figure 9. Broberg-Morrey modified radial head fracture classification.....	13
Figure 10. Incision for radial head replacement	16
Figure 11. Various radial head prostheses (first row from left; Swanson, Ascenson, Solar, second row; Judet, Evolve, rHead, third row; Katalyst, Liverpool).....	18
Figure 12. 3-D solid model of the elbow	36
Figure 13. Front (left) and side view (right) of native elbow FE model mesh	38
Figure 14. Maximum contact stress with different mesh size in (a) humeroradial and (b) radioulnar joints	42
Figure 15. Contact area with different mesh size in (a) humeroradial and (b) radioulnar joints..	43
Figure 16. Average pressure with different mesh size in (a) humeroradial and (b) radioulnar joints	44
Figure 17. Contact stress distribution of capitellum under 50N (top), 100N (middle), and 200N (bottom).....	45

Figure 18. Contact stress distribution of radial head (medial side) under 50N (top), 100N (middle), and 200N (bottom)	46
Figure 19. Maximum contact stress with different cartilage thickness on capitellum in (a) humeroradial and (b) radioulnar joints	49
Figure 20. Contact area with different cartilage thickness on capitellum in (a) humeroradial and (b) radioulnar joints.....	50
Figure 21. Average pressure with different cartilage thickness on capitellum in (a) humeroradial and (b) radioulnar joints	51
Figure 22. Maximum contact stress with different cartilage thickness on radial head in (a) humeroradial and (b) radioulnar joints.....	52
Figure 23. Contact area with different cartilage thickness on radial head in (a) humeroradial and (b) radioulnar joints.....	53
Figure 24. Average pressure with different cartilage thickness on radial head in (a) humeroradial and (b) radioulnar joints	54
Figure 25. Maximum contact stress with different Young's modulus in (a) humeroradial and (b) radioulnar joints.....	56
Figure 26. Contact area with different Young's modulus in (a) humeroradial and (b) radioulnar joints	57
Figure 27. Average pressure with different Young's modulus in (a) humeroradial and (b) radioulnar joints.....	58
Figure 28. Maximum contact stress with different Poisson's ratio in (a) humeroradial and (b) radioulnar joints.....	59
Figure 29. Contact area with different Poisson's ratio in (a) humeroradial and (b) radioulnar joints	60
Figure 30. Average pressure with different Poisson's ratio in (a) humeroradial and (b) radioulnar joints	61
Figure 31. Max. contact stress with different bone material property in (a) humeroradial and (b) radioulnar joints.....	63
Figure 32. Contact area with different bone material property in (a) humeroradial and (b) radioulnar joints.....	64

Figure 33. Average pressure with different bone material property in (a) humeroradial and (b) radioulnar joints.....	65
Figure 34. Maximum contact stress with different ligament stiffness in (a) humeroradial and (b) radioulnar joints.....	67
Figure 35. Contact area with different ligament stiffness in (a) humeroradial and (b) radioulnar joints	68
Figure 36. Average pressure with different ligament stiffness in (a) humeroradial and (b) radioulnar joints.....	69
Figure 37. Front (left) and side view (right) of monoblock implant FE model mesh.....	72
Figure 38. Maximum contact stress in humeroradial joint with different size of monoblock implant	72
Figure 39. Contact area in humeroradial joint with different size of monoblock implant.....	73
Figure 40. Average pressure in humeroradial joint with different size of monoblock implant....	73
Figure 41. Contact stress distribution of capitellum with rHead implant under 50N (top), 100N (middle), and 200N (bottom).....	74
Figure 42. Front (left) and side view (right) of the bipolar implant FE model mesh	76
Figure 43. Maximum contact stress in humeroradial joint with different size of bipolar implant	76
Figure 44. Contact area in humeroradial joint with different size of bipolar implant	77
Figure 45. Average pressure in humeroradial joint with different size of bipolar implant	77
Figure 46. Contact stress distribution of capitellum with Katalyst implant under 50N (top), 100N (middle), and 200N (bottom).....	78
Figure 47. Fuji film packet (super low)	80
Figure 48. Experimental setup: cadaveric elbow mounted into MTS Bionix 858, side view (left) and front view (right).	81
Figure 49. Scanned image of Fuji film (super low)	83
Figure 50. Maximum contact stress comparison	87
Figure 51. Contact area comparison	87
Figure 52. Average pressure comparison.....	88

PREFACE

First off, I would like to thank my advisor Dr. Mark C. Miller for numerous invaluable pieces of advice and immense knowledge about biomechanics. I truly appreciate the opportunities you have given me. I also appreciate my committee members, Dr. Patrick Smolinski, Dr. Rakié Cham and Dr. Richard Debski, for suggesting various approaches to finite element analysis and experimental design. I am thankful to Dr. Laurel Kuxhaus for teaching me preparing cadaveric specimens for the testing, giving me lessons for CMM and MTS, and inviting my wife and me for the quintet. We really enjoyed your music. I would like to thank Dr. Muturi Muriuki for teaching me everything about Fuji pressure sensitive film from making packets to analyzing them. Your Matlab programs were crucial for the success of this project. I am grateful to all of my former and current lab mates, Pat, Brandon, Bradley, Dave, Amin, Collin, Mandy, and Will. It has been a pleasure to work with you all.

I would like to deeply thank my lovely wife for her love, patience and support. Most of all, I would like to say thank you for giving a birth to our precious daughter, Avery who has become my refreshment when I was tired. I would also like to express my gratitude for my families in Korea for their support, prayer, and love.

1.0 INTRODUCTION

A radial head fracture, first described in 1905, is a common fracture, and accounts for about 30% of fractures of elbow joint and 1.7 to 5.4% of all fractures [1, 2]. Approximately 10% of elbow dislocations are associated with radial head fracture [3]. The most common cause of the radial head fracture is a fall on an outstretched arm. However, the radial head can be fractured by the direct impact or high energy trauma, as well [4].

Radial head fractures were classified by Mason [5] into three types (types I, II, and III) based on the number and the displacement of fractured fragments as well as the extent of fracture. This classification has been useful for treatment. Minimally damaged radial head fractures (Type I) can be managed by nonsurgical treatment. Surgical treatments such as radial head excision, open reduction and internal fixation (ORIF), and radial head arthroplasty can be conducted for more serious fractures (Type II, Type III and dislocated elbow with radial head fracture).

Radial head arthroplasty is recommended when the radial head is comminuted and is associated with a joint dislocation or instability. Various implants are available with different design features such as monoblock, bipolar, modular, cemented, and uncemented. Silicone implants were the preferred option until metal prostheses replaced them due to many reported complications such as prosthesis failure, adverse tissue reaction, and poor load transfer [6-8]. Recently metal implants have been popular with good short to mid-term results [9-11]. Most metal implants are manufactured from either titanium or cobalt-chrome alloy because they are strong,

low in density, highly corrosion resistant, and biocompatible. Basically, there are two choices for the radial head implant; monoblock and bipolar. Monoblock implants have larger radius curvature for the top surface of the implant head which contacts with capitellum of the humerus than bipolar ones. A monoblock radial head is known to be more stable and resistant to valgus load. A bipolar radial head was developed with the expectation that stress can be reduced by providing more congruent contact with the capitellum. However, the performance of each design concept has not yet been fully evaluated.

The goal of this study was to examine the performance of the two different types of radial head implants compared to the native radial head by investigating the contact stress and the contact area provided by the constructed FE models. Finite element models for the intact and radial head replaced elbow joints with two different implants were created from CT scans of a cadaveric elbow and validated with experimental work using Fuji pressure sensitive film. Using custom FE models contact pressure and contact area were calculated and compared.

2.0 BACKGROUND

2.1 ANATOMY AND BIOMECHANICS OF THE ELBOW

The elbow joint consists of three long bones; two bones (ulna and radius) are in the forearm and the humerus is in the upper arm (See Figure 1). There are three joints involved in the elbow: humeroulnar, humeroradial, and radioulnar joints. The olecranon process and the coronoid process of the ulna form the humeroulnar joint, which is a hinge joint, with the trochlea of the humerus. The joint where the humerus meets the radius is the humeroradial joint which is formed by an almost spherical joint surface that fits into the shallow concave top surface of a cylinder. The humeroradial joint is a ball and socket joint. The sphere on the distal end of the humerus is called the capitellum, which fits into the proximal end of the radius, called head of the radius or radial head. The radioulnar joint is a trochoid or pivot joint which is the articulation formed by the medial side of the radial head and radial notch of the ulna (ulnar notch). Flexion is the bending of the arm which increases the angle between the humerus and the forearm and extension is the opposite of the flexion which decreases the angle (Figure 2). Supination of the forearm is the rotation which brings the palm of the hand facing anteriorly with the thumb directed laterally and pronation is the opposite of supination (Figure 3). The humeroradial and humeroulnar articulations allow the arm flexion/extension and the proximal radioulnar articulation is necessary for supination/pronation of the forearm. The normal range of flexion and extension is from 0° (full extension) to 146° (full flexion) and the average range of motion for supination and pronation of the forearm are 81° and 71° respectively [12]. The angle between the long axes of the humerus and the ulna in the anteroposterior (coronal) plane with the elbow fully extended and the forearm supinated is known

as the carrying angle. The carrying angle averages from 10° to 15° and is greater in females than children and males [13]. The three major muscles for flexion are the biceps, brachioradialis, and brachialis. The brachialis contributes the most force and the brachioradialis the least in resistance to an extension moment [14]. The primary extensor is the triceps. The biceps brachii is the primary muscle for supination but also effects flexion. The pronator quadratus and the pronator teres are involved in pronation of the forearm. According to one study [15], pronation strength was 86% of supination strength and extension strength was about 60% of flexion strength in normal individuals, which is consistent with the moment arms and cross-sectional areas of the muscles of each movement.

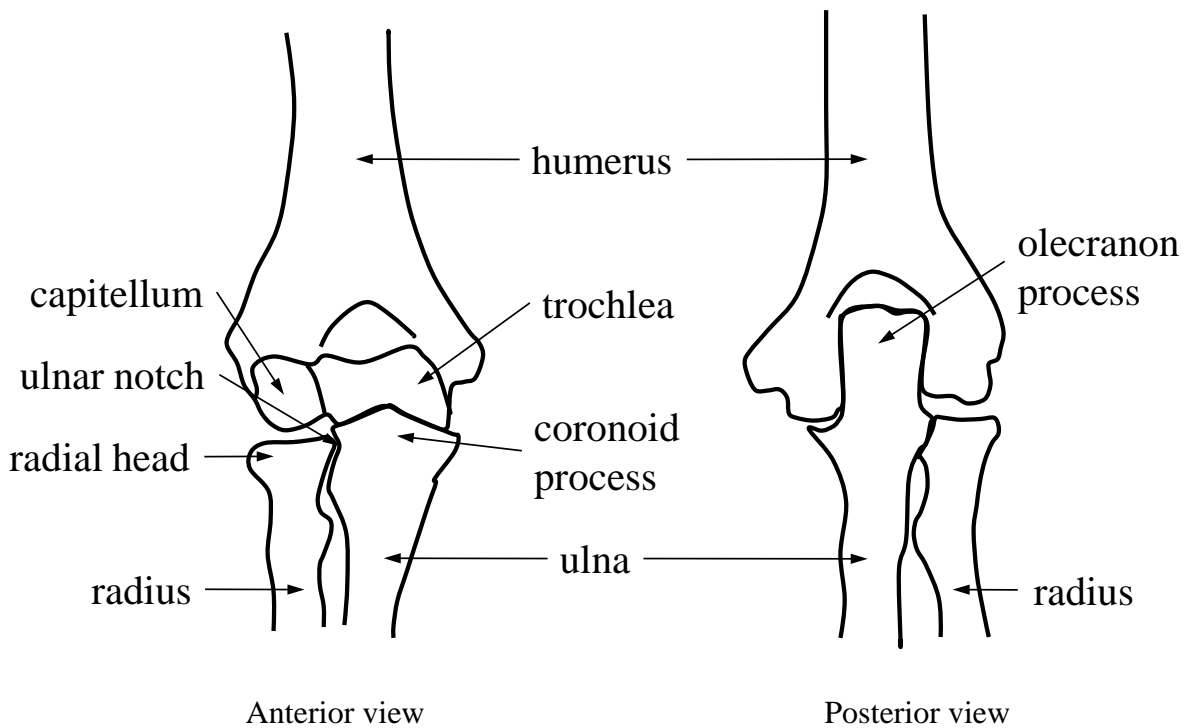


Figure 1. Anatomy of the elbow joint

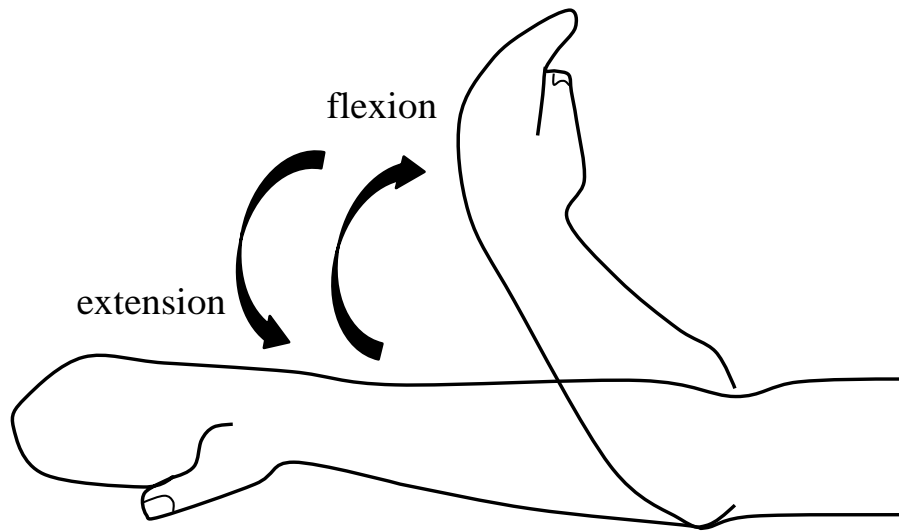


Figure 2. Elbow flexion and extension

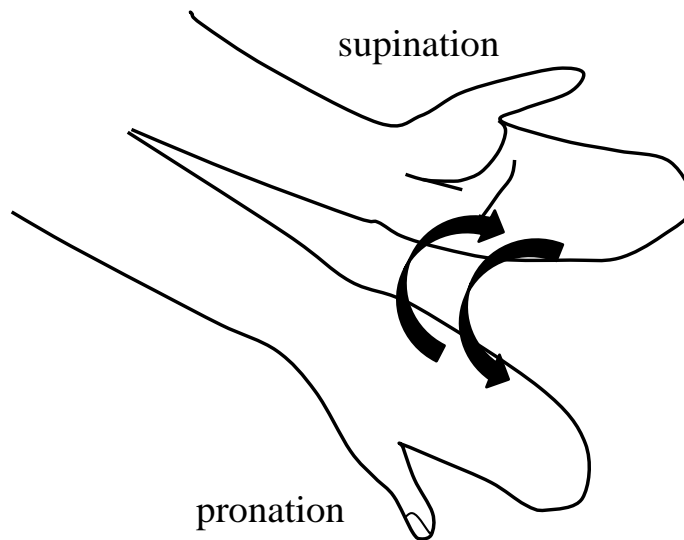


Figure 3. Supination and pronation of the forearm

The three bones in the elbow joint are connected to each other by the medial collateral ligament (MCL) complex and the lateral collateral ligament (LCL) complex. The MCL complex consists of anterior and posterior bundles and transverse ligament (Figure 4). The anterior bundle is divided into two bands: the anterior and posterior bands. The anterior band is taut from full extension to 60° of flexion while posterior band is taut 60° to 120° of flexion [16]. The LCL complex is composed of the lateral ligament, the lateral ulnar collateral ligament, the annular ligament and the accessory collateral ligament (Figure 5). The annular ligament encompasses and holds the radial head in position. The MCL is the primary constraint of the elbow joint against valgus load [13, 17] and the LCL is an important stabilizer of the humeroulnar joint against varus stress and posterolateral rotation [18-24]. The radial head is also an important stabilizer for valgus load with MCL. When MCL is disrupted or dissected, the radial head becomes the primary stabilizer for valgus stress [17, 25].

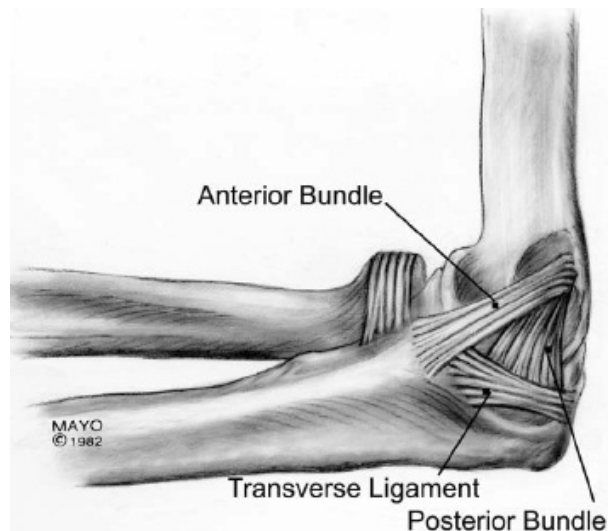


Figure 4. MCL complex of the elbow joint [26]

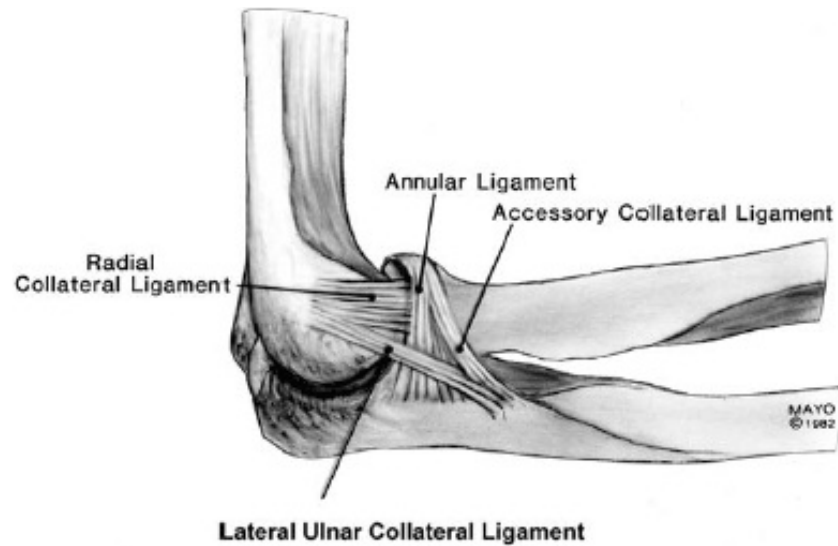


Figure 5. LCL complex of the elbow joint [26]

2.1.1 Radial head

The anatomy of the radial head, articulating with capitellum of the humerus and radial notch of the ulna, is highly complex and variable [27, 28] (Figure 6). Most of radial heads are elliptical although some people have almost round radial head [27, 29] and four fifths of the radial head is covered by hyaline cartilage [30]. The radial neck is angulated about 15° from the long axis of the radius away from the tuberosity [30]. Up to 60% of the load across the elbow is transferred through the radiocapitellar articulation in full extension [31]. It has been reported that 3 times body weight can be applied to this joint during strenuous activities [32, 33].

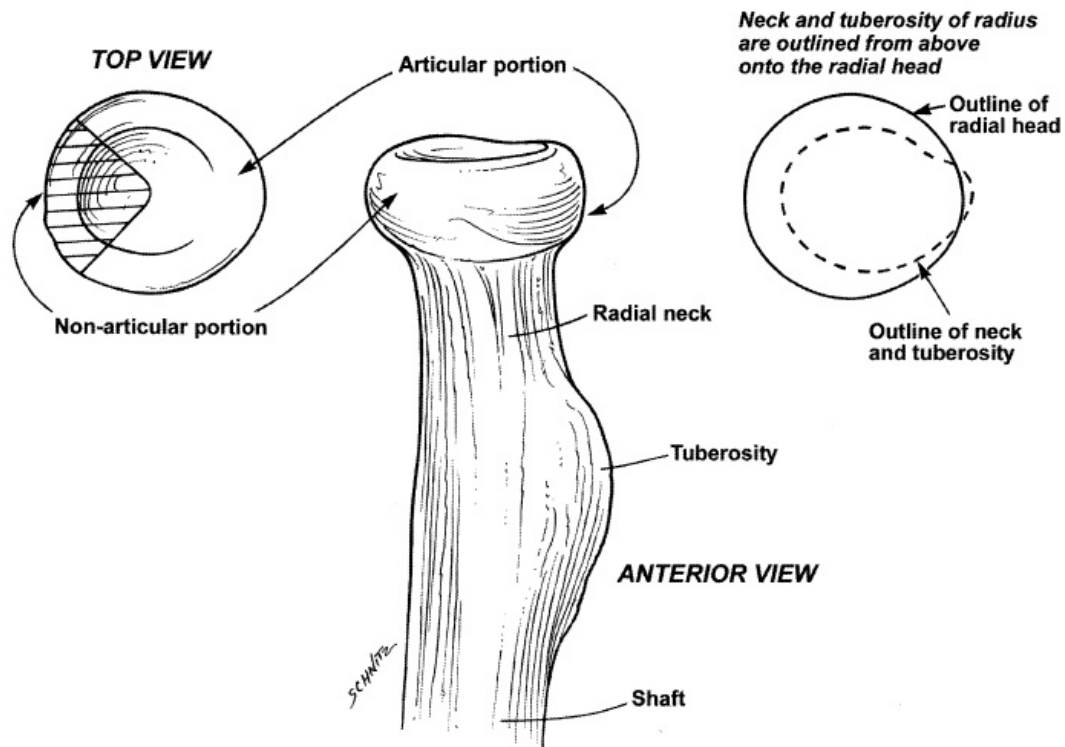


Figure 6. Anatomy of the radial head [34]

2.1.2 Capitellum

The distal humerus is divided into two columns: medial and lateral (Figure 1). The medial column consists of medial epicondyle and medial condyle including trochlea which articulates with trochlea notch of the ulna. The lateral column consists of lateral epicondyle and lateral condyle including capitellum which articulates with the radial head of the radius. The capitellum is covered by hyaline cartilage and its shape can be described by two radii of curvatures (sagittal and transverse) [35].

2.2 BONE

Bone is the hardest structure in the body, supporting the body and protecting internal organs. It also produces the red and white blood cells and stores minerals. A bone consists of cellular component and extracellular matrix (ECM). The cellular component includes osteoblasts, (bone forming cells), osteoclasts, (bone resorbing cells), and osteocytes, (bone maintaining cells). The ECM is composed of collagen fibers and mineral. Unlike other connective tissues, a bone has high content of inorganic materials such as calcium and phosphate, which make the bone hard and rigid, while the organic component provides flexibility.

Macroscopically there are two types of bones: cortical and cancellous. The outer layer of the bone is composed of hard compact tissue called cortical bone and the inside of the bone is typically filled with cancellous bone (trabecular or spongy bone), which is an open cell, porous network that makes the bone lighter and allows space for blood vessels. The border between the cortical bone and cancellous bone is not distinct and the transition is continuous [36]. The relative quantity of each type of bone varies among bones. Cortical bone is an anisotropic material, which means that material properties vary according to the loading direction (Figure 4), and is stiffest when loaded in the longitudinal direction. The elastic modulus for the cortical bone is approximately 11.5 GPa [37] in the longitudinal direction in compression. For this reason cortical bone is often considered as an orthotropic material [38, 39] characterized by three different elastic moduli, three shear moduli, and three Poisson's ratios. Cancellous bone is more complex than cortical bone. The elastic modulus for the cancellous bone is a function of density. A literature survey about the elastic modulus of the cancellous bone was carried out by Rho et al. [36] who showed that it ranged from 0.76 to 20 GPa.

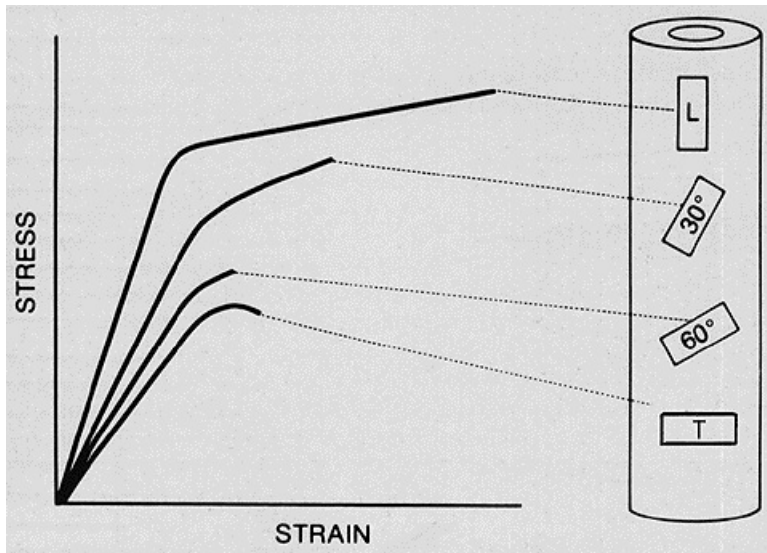


Figure 7. Anisotropic behavior of cortical bone in tension in four directions [40]

2.3 ARTICULAR CARTILAGE

Articular cartilage is a flexible but stiff connective tissue found in synovial joints between bones. Its function is to distribute the load applied to the joint without failure. Cartilage is composed of ECM, chondrocytes, water and organic compounds, such as proteoglycans. In normal articular cartilage, water content ranges from 60 to 80% of the total wet weight of the cartilage. The ECM is a dense network of collagen Type II fibers and proteoglycans. Articular cartilage shows a layered structure with four primary zones: a superficial tangential zone (STZ), a middle zone, a deep zone and a calcified zone (Figure 6). Water and collagen decrease from the STZ to the deep zone. The middle zone has the most proteoglycan. Collagen fibrils are arranged parallel to the articular surface in the STZ, randomly in the middle zone and perpendicularly to the bone-cartilage interface in the deep zone connecting the cartilage to the bone. Cartilage thickness varies with

joints, age, and location within joint. It has been measured with several different techniques such as a needle probe system [41, 42], X-ray [43], CT [44], MRI [45, 46], and ultrasound [47].

Cartilage is inhomogeneous, nonlinear, and anisotropic [48] but the first models for the cartilage were linearly elastic [49-52], which was sufficient for predicting static and instantaneous loading conditions. These models did not take into account time dependent behavior of the cartilage. Thus, viscoelastic models were proposed [53, 54]. However, the effect of fluid inside the cartilage was not explained until a biphasic model was introduced by Mow [55] and McCutchen [56]. In this model cartilage was treated as a material consisting of two incompressible, immiscible and distinct phases [55, 57]: a fluid phase representing water and dissolved electrolytes and a solid phase representing collagen fibers, chondrocytes, and proteoglycans. Under compression fluid exudation occurs through the solid phase which is porous and permeable.

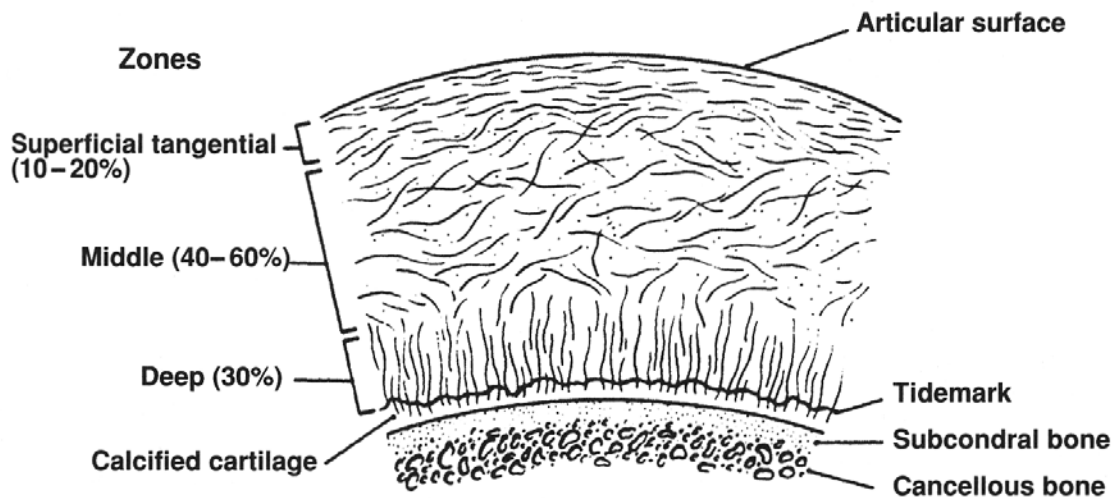


Figure 8. Structure of articular cartilage [58]

2.4 LIGAMENT

A ligament is a dense fibrous tissue that connects bones to other bones to form a joint. It consists of 20% of cellular material (fibroblast) and 80% of noncellular material. Approximately 70% of the noncellular material is water and remaining 30% is solids which are composed of an ECM of collagen, ground substance and a small amount of elastin [13].

Ligaments are viscoelastic, exhibiting rate dependent behavior under loading. Material properties of ligaments also vary depending on the rates of loading. The stiffness of ligaments becomes greater with higher strain rates [59]. When tensile load is applied to a ligament, it gradually elongates and then returns to its original length when the applied load is removed. However, ligaments cannot maintain their original shape when they are stretched past a certain point or for a long period of time. This can cause joint instability and lead to wear of cartilage over time.

2.5 RADIAL HEAD FRACTURES

The radial head can fracture from a direct impact as well as from the indirect force resulting from a fall on an outstretched hand. Since Mason [5] classified radial head fractures into three types, a number of modifications have been developed. Figure 6 shows the Broberg-Morrey modified classification of radial head fractures. Type I is a radial head fracture which is undisplaced or displaced no more than 2 mm. A radial head fracture is Type II when the radial head is displaced greater than 2 mm and 30% of the surface of the radial head is involved in the fracture. Type III is the comminuted fractures of the radial head and Type IV is any type of radial head fracture with

elbow dislocation [60]. Although this modified classification is useful for treatments of radial head fractures, it can still be problematic to distinguish between Type II and Type III [34].

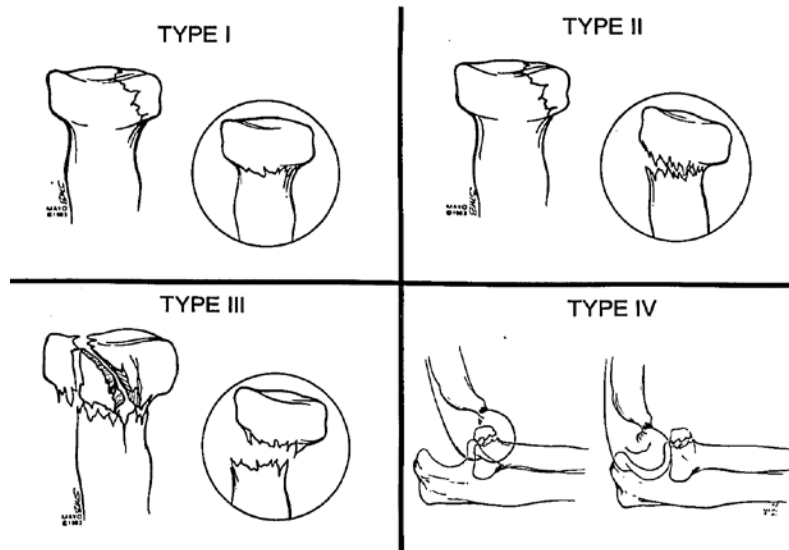


Figure 9. Broberg-Morrey modified radial head fracture classification [60]

2.6 TREATMENTS FOR RADIAL HEAD FRACTURE

The first goal of treatment is to restore the stability and range of motion of the elbow joint. When deciding how to treat radial head fractures, the number of fragments, the amount of displacement, and associated injuries should be considered. Nonsurgical and surgical treatments are available for radial head fractures. Immobilization using a collar and cuff sling and early motion are used for minimally damaged nondisplaced radial head fractures and have been reported with good results [61, 62]. The sooner patients start motion after immobilization, the better results they get. Comminuted displaced radial head fractures can be managed by surgical treatments such as excision, ORIF, or radial head arthroplasty. ORIF is recommended when the radial head is

fractured and displaced but not comminuted and bone quality is good. Small screws can be used for partial radial head fracture and plates are useful for more complex fractures [63]. For comminuted fractures of the radial head, excision is optimal only when the fracture is isolated [64]. However, comminuted fractures are usually not isolated and excision can cause altered kinematics and instability of the elbow joint [65, 66]. Radial head arthroplasty is performed when the radial head is comminuted and displaced with associated elbow joint instability due to soft tissue injuries.

2.6.1 Radial head excision

Radial head excision was the treatment of choice for displaced radial head fractures in the early twentieth century before reliable methods of internal fixation were developed. Although recently performed less frequently, this can be recommended when a radial head fracture is isolated, displaced, and comminuted and when ORIF is not possible. Following the excision of the radial head, if there is evidence of medial or lateral elbow instability, radial head replacement should be performed [64].

2.6.2 Open reduction and internal fixation [ORIF]

ORIF is a method for repairing fractured bones. Bone fragments are moved into position using a dental pick or K-wire after the fractured bone is exposed. Then, screws are used to join fragments. More complex fractures can be fixed with plates and an intramedullary rod can be used for the stability of the bone. Displaced but not comminuted radial head fractures can be handled with ORIF and good results have been reported [67, 68]. Radial head fractures with multiple fragments can be treated successfully by ORIF if stable internal fixation is achieved [67, 69-71]. Ring et al.

[71] reported complications after ORIF of radial head fracture with more than 3 fragments and suggested other surgical methods for more comminuted fractures. Tenuous fixation should be avoided if the radial head fracture is associated with ligamentous injuries [67] [71]. Failed surgical reconstruction can cause articular injury to the capitellum and the ulnar notch [34].

2.6.3 Radial head arthroplasty

Radial head replacement surgery is conducted when the radial head is comminuted and there is an associated loss of joint stability. The surgical procedure is as follows. A patient lies supine with the injured arm internally rotated toward the center of the body. A tourniquet is placed under the arm. An incision is made longitudinally from the lateral epicondyle to the radial head (Figure 7). A surgeon must be careful not to cut the lateral collateral ligament. Through the incision, the radial head is exposed and removed. An appropriately sized head and stem for the prosthesis are chosen and inserted into the radius. After the replacement of the radial head with the implant, range of motion should be checked to ensure that there is no binding between the radial head prosthesis and the capitellum throughout the entire flexion/extension range of motion. Before the incision is closed, damaged ligaments should be reconstructed. Radial head replacement surgery takes about one hour and, after the surgery, the arm is placed in a soft cast for approximately two weeks. Then, physical therapy starts to restore joint function. Full recovery from the radial head replacement surgery can take three to six months.

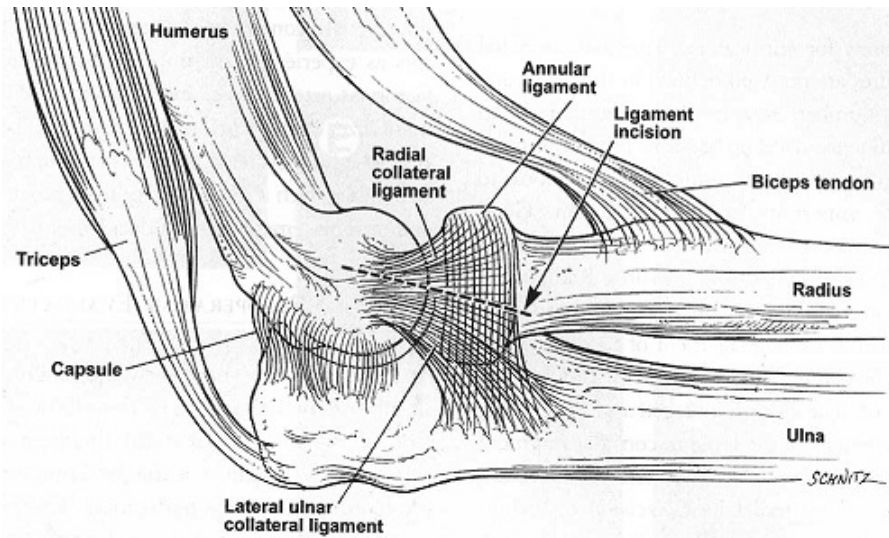


Figure 10. Incision for radial head replacement [4]

2.7 RADIAL HEAD IMPLANTS

The first radial head replacement made from vitallium was reported with three satisfactory cases in 1941 by Speed [72] as an alternative to excision to avoid the regrowth of bone at the proximal radius, which was one of the most feared complications after excision [73-76]. It was cast from the excised normal radial head and placed over the radius to prevent bone formation.

The Swanson silastic radial head prosthesis was developed in 1969. Biomechanical studies showed that elbow stability could be restored by radial head replacement [25, 77-79]. Cherry [80] introduced an acrylic resin radial head implant to prevent proximal movement of the radius, which could lead to change in carrying angle of the elbow and subsequent cubitus valgus. However, the use of the radial implant remained rare at that time [81]. However, the first complications of this implant were reported in 1979 by Mackay [82]; three out of eighteen implants with an average follow-up of 26 months were broken and one subluxed. A high number of complications have

also been described including painful motion, stem fracture, stem loosening, synovitis, and osteoporosis [6, 7, 83, 84]. Due to the complications with silastic implants there has been increasing interest in metallic implants [78].

The Judet floating (bipolar) radial head prosthesis was produced in 1988. The first version was made from titanium but replaced by cobalt-chrome alloy in 1994 [85]. Rotation and tilt of the head of bipolar implants allowed more congruent contact with the capitellum of the humerus and sought to reduce the contact stresses between the implant and the bone. However, complications including aseptic loosening and dislocation of the implants have been reported for bipolar radial head implants [86-88]. Radiocapitellar instability has been also reported as one of serious complications for bipolar implants [86, 89] and this may cause osteoarthritis and joint contracture [90].

There are a number of radial head prostheses with different features [4]. They have stems and radial heads of different shapes and most of them are made from titanium or cobalt-chrome alloys. Radial head prostheses can be classified by function and fixation 1) into monoblock (a one piece implant) and bipolar (a ball and socket type implant) based on the neck and head connection, and 2) into cemented and uncemented based on stem fixation technique. Some of the radial head prostheses currently used are shown in Figure 8. The Swanson (Wright Medical Technology, Arlington, TN) radial head is a monoblock uncemented titanium prosthesis available in five different sizes. The Ascension (Ascension Orthopedics, Austin, TX) radial head is a modular press fit (uncemented) monoblock cobalt-chrome implant which comes with six different sizes. The Solar (Stryker, Rutherford, NJ) radial head is a monoblock, cemented cobalt-chrome implant available in two different sizes. The Judet (Tournier SA, Saint-Ismier, France) radial head is a bipolar cobalt-chrome implant which comes with 2 different heads and stems: long cemented and

short press-fit stem. The rHead (Small Bone Innovations, New York, NY) radial head is a modular cemented monoblock cobalt-chrome implant with the head sizes from 18 to 24 mm. The Katalyst (Integra LifeSciences, Plainsboro, NJ) radial head is a bipolar modular cobalt-chrome implant with 3 head diameters (18, 21, and 24 mm) and 2 stem options. The Liverpool (Biomet, Warsaw, IN) radial head is a monoblock implant with two head sizes while the Evolve (Wright Medical Technology, Arlington, TN) radial head is a modular cobalt-chrome implant with 15 head and 10 stem sizes.



Figure 11. Various radial head prostheses (first row from left; Swanson, Ascenson, Solar, second row; Judet, Evolve, rHead, third row; Katalyst, Liverpool)

2.8 FINITE ELEMENT ANALYSIS

The finite element method (FEM) is a mathematical tool for calculating numerical solutions of partial differential equations and integral equations. The origin of FEM dated to the 1943 paper by a mathematician, Richard Courant [91]. In his work, a piecewise polynomial solution to a torsion problem was described, but at that time it did not draw much attention by engineers because the procedure was impractical without digital computers. In the 1950s, FEM was introduced to engineers in the aircraft industry and started to be used for solving partial differential equations. By 1963 FEM was validated mathematically and its use expanded from structural analysis to heat transfer, magnetic fields, and other areas. General purpose FE software began to appear in the 1970s and by the late 1980s commercial FE packages were available on microcomputers with color graphic pre- and post-processors.

FEM was adopted in the field of orthopaedic biomechanics in 1972 to calculate stresses in a human body [92]. FEM is a very effective computer-aided mathematical tool for orthopaedic research because it can handle highly complex irregular objects such as bones, ligaments and tendons. It is also easy to try different material properties or designs before manufacturing the actual products, thereby saving money in time and experimental setup. In the method, complex structures are divided into a number of smaller and simpler components called elements and connected at nodes, which are like mathematical pins holding elements together. This process of subdivision results in a set of algebraic equations. These equations are the equilibrium equations for the nodes in the stress analysis. The matrix form of this set of equations is expressed as equation (1), where \mathbf{K} is a known stiffness matrix, \mathbf{F} is a vector of known loads, and \mathbf{D} is an unknown vector of field quantity such as displacement at nodes.

$$[\mathbf{K}]\{\mathbf{D}\} = \{\mathbf{F}\} \quad (1)$$

Then, material properties are assigned to each of element and appropriate loading and boundary conditions are defined. Finally, the combined governing equations for each element are solved using iterative methods. Over an element, a field quantity is interpolated from values of the field quantity at nodes.

A calculated solution can be inaccurate if the solution is not converged. H- and P-methods are available to check the convergence of the solution. For H-method, simple shape functions and a large number of small elements are used. In order to obtain a more accurate solution, more elements must be used. On the other hand, complex shape functions and large elements are used for P-method. The higher complexity of the shape function, higher order of polynomial for example, is required to increase the accuracy of the solution. Thus, the mesh does not need to be refined for P-method.

2.8.1 Contact analysis

The goals for contact analysis are to obtain the stresses transmitted across a contacting interface and to calculate the area of contact. Contact analysis has been used in biomechanics for calculating joint pressure and is a very effective tool for developing implants. However, contact analysis is highly nonlinear and requires a significant computer resources. There are two difficulties in contact analysis. First, the contact region is not known prior to the analysis. Second, friction introduces additional nonlinearities. Due to these nonlinearities, convergence of the analysis could be very difficult without appropriate boundary and loading conditions (rigid body motion can occur easily unless the model is sufficiently constrained). There are several different algorithms

available to deal with contact problems. They are the Penalty method, the Lagrange multiplier method, and the augmented Lagrange method. For the penalty method, which uses springs to establish a relationship between two contact surfaces, the contact force is assumed in a similar manner as equation (1) and written as equation (2).

$$\mathbf{K}_{\text{contact}} \cdot \Delta \mathbf{D}_{\text{penetration}} = \Delta \mathbf{F}_{\text{contact}} \quad (2)$$

where $\mathbf{K}_{\text{contact}}$ is the contact stiffness, $\Delta \mathbf{D}_{\text{penetration}}$ is the gap or penetration between two contact surfaces and $\Delta \mathbf{F}_{\text{contact}}$ is the contact force. In this method, $\Delta \mathbf{D}_{\text{penetration}}$ is not equal to zero because $\mathbf{K}_{\text{contact}}$ would be infinite if it were. So, there is a finite amount of penetration between two contact surfaces. The advantage of this method is that it is simple and the displacement-based FE framework remains. The disadvantage is that the equation can be ill-conditioned if the stiffness is too high and consequently some iterative solvers may have difficulties with the ill-conditioned equations, requiring more iterations. This problem can be alleviated using the augmented Lagrange method to control the penetration to a given tolerance.

For the Lagrange multiplier method, the contact force is treated as a separate DOF as equation (3).

$$[\mathbf{K}]\{\mathbf{D}\} = \{\mathbf{F}\} + \{\mathbf{F}_{\text{contact}}\} \quad (3)$$

This gives the benefit of bypassing contact stiffness and penetration. However, the stiffness matrix can be considerably larger due to the additional DOF's; and abrupt changes in the contact status can occur despite the control by real constants such as the maximum allowable penetration

and maximum allowable tensile force. The augmented Lagrange method is a penalty method with penetration control which is the combination of the penalty method and the pure Lagrange multiplier method.

ANSYS 11.0 has five options for the contact analysis: penalty, augmented Lagrangian (default), Lagrange multiplier on contact normal and penalty on tangent, Lagrange multiplier on contact normal and tangent, and internal multipoint constraint (MPC). MPC algorithm is based on bonded contact and no separation between two contact surfaces is allowed.

2.8.2 FE contact parameters

There are several contact parameters used for contact analysis in ANSYS to control penetration and slip between two contact surfaces.

2.8.2.1 FKN and FKT

FKN and FKT are normal and tangent contact stiffnesses which determine the penetration and the slip. High stiffness leads to less penetration and slip which is desirable but may cause ill conditioning of the stiffness matrix. Low stiffness reduces the computation time but can produce the inaccurate results. Thus, it is important to choose a high enough stiffness so that the penetration and slip are acceptably small, but a low enough stiffness that avoids long computation time due to convergence difficulties. The default value for FKN is 1 (default value) which is appropriate for bulk deformation. A smaller value (0.1) is recommended when bending is dominant.

2.8.2.2 FTOLN and SLTO

FTOLN and SLTO are tolerance factors in the directions normal and tangential to the contact surface. FTOLN is used to determine contact compatibility which is satisfied when the penetration is within an allowable tolerance (FTOLN times the depth of underlying elements). The depth is the average depth of contact elements. If any penetration larger than this tolerance is detected, the global solution is considered unconverged, even though the forces and displacement increments have met convergence criteria. SLTO is used to control maximum sliding distance. A larger value of SLTO will increase convergence speed but lower accuracy.

2.8.2.3 PMAX and PMIN

Any part without appropriate constraints in a static analysis can result in a rigid body motion. In order to avoid a rigid body motion, the contact and target surfaces should be in just touching position (slight penetration or gap should exist in the initial geometry). PMAX and PMIN can be used to establish initial contact status. PMAX and PMIN specify an initial allowable penetration range. If initial penetration is larger than PMAX or smaller than PMIN, ANSYS reduces penetration or ensures initial contact by moving the target surface.

2.9 FUJI PRESSURE SENSITIVE FILM

Fuji pressure sensitive film (Fuji Photo Film Co. Ltd., Tokyo, Japan) has been used to measure contact pressures and contact areas within the hip [93], the patellofemoral [94, 95], tibiofemoral [95, 96], the ankle [95], the distal radio-ulnar [97], and the humeroulnar [98] joints. Fuji film consists of two sheets: A-film and C-film. Each film has an active coating on one side. A-film

has a layer of micro-bubbles containing colorless liquid on the active surface. C-film has a color developing layer reacting with the micro-bubbles of A-film on the active surface. The active surfaces of A and C-films must contact each other to measure pressure. When a load is applied to the film, pink stain appears. The intensity of the stain is proportional to the magnitude of the applied load and can be converted to applied pressure using either the manufacturer's or laboratory quantified optical comparison charts. Six grades of Fuji film are available and each of them covers a different range of pressure. The pressure range for each film grade is given in Table. 1.

Table 1. Fuji film pressure ranges (Pressurex[®] film, SPI sensor products Inc.)

Film grade	Pressure Range (MPa)
Ultra Low	0.2 – 0.5
Super Low	0.5 – 2.5
Low	2.5 – 10
Medium	10 – 50
High	50 – 130
Super High	130 – 300

3.0 BACKGROUND REVIEW OF CONTACT ANALYSIS

Analysis of contact pressure and contact area is fundamental for the understanding of the biomechanics of human joints and joint arthroplasty. Human joints have been investigated by examining both contact pressure and contact area, which have been measured using various techniques including pressure sensitive film and tactile sensors. The relevant literature can provide guidance in the choice of methods and in the understanding of the outcomes of analyses.

3.1 JOINT PRESSURE AND CONTACT AREA

Contact areas and pressures at the hip, knee, ankle, wrist, and elbow joints have been measured using pressure sensitive films and tactile sensors. A contact study of the hip joint was performed by Miyanaga et al. [99] to understand the load deformation pattern under compressive loading. Pressure sensitive film was used to measure the contact pressure distribution and the contact area from five normal cadaveric hip joints. Loads (500, 1000, 1500, and 2000 N) were applied to the femoral head at cross head speeds of 1, 3, and 5 mm/min to obtain load deformation curves. Joint pressure was quantified with a densitometer, and contact area was measured using a casting method with silicone rubber usually used for dental impressions. They found that pressure distribution patterns were neither uniform nor symmetrical and pressure was mainly distributed over the anterior and posterior parts of the acetabulum. The peak pressure recorded was approximately 2 MPa at the centers of the anterior and posterior parts under loading of 1000 N. Peak pressure values at higher loads were not described. The average measured contact areas were

8.6 cm² at 1000 N, and 12.7 cm² at 2000 N. The maximum contact area was 14 ~ 16 cm². Afoke et al. [93] measured hip joint pressure in five cadaveric hip joints using Fuji film at three different flexion/extension angles (27° flexion, 0° neutral, and 18° extension) under three different loads (3.3 BW, 1.3 BW, and 4 BW) simulating gait cycle. They found that the maximum stress was approximately 10 MPa in 27° flexed hip with 3.3 BW and 18° extended hip with 4 BW. High pressure was detected in the antero-superior surface of the cartilage.

Patellofemoral joint pressures were measured by Haut [94] in the flexed knee to examine whether impact without bone fracture could damage cartilage. Loads were delivered on the patella by free flight of a 4.5 kg inertial mass shot from a high pressure pneumatic accelerator. They increased the velocity of the flying mass until bone fracture was observed at three different joint flexion angles (60°, 90° and 110°) and at two different impact conditions (rigid and padded). They then used two different grades of pressure sensitive film to measure the joint pressure (high range film, 25 ~ 70 MPa) and contact area between the impactor and the knee (medium range film, 7 ~ 25 MPa). Fracture of the patella of the femur occurred at approximately 8.5 kN of the impact load and the average patellofemoral joint pressure was 25 MPa on the 90° flexed joint. Without padding, the peak stresses averaged approximately 15 MPa at 3 kN impact load and 25 MPa at 8 kN for 90° joint flexion. With padding, average contact area was 54.6 cm² and for rigid interface 115.1 cm².

Fukubayashi [96] measured the contact area and the peak stress in the tibiofemoral joint with and without a meniscus at 0° of the knee joint flexion angle. Fuji film and a casting method with silicon rubber were used for measuring pressures and contact area respectively. They reported that the peak pressure was 3 MPa with a meniscus and 6 MPa without a meniscus at a load of 1000 N. Contact area was decreased from 11.5×10^2 mm² with a meniscus to 5.2×10^2 mm² without one under the same applied load.

Wang et al. [100] investigated pressure distribution and contact area of the subtalar joint with various foot positions. They used nine amputated lower legs. Each foot was mounted onto a material testing machine and tested with three different loads (600, 1200, and 1800 N) in a neutral position and with 600 N in different foot positions (plantar/dorsiflexion and inversion/eversion). Lower grade pressure sensitive film was inserted into the joint to measure the pressure and contact area. They found that the average contact area of the subtalar joint where the contact pressure exceeded 2.45 MPa was 1.18 cm² and accounted for only 12.7% of the whole articular surface (9.31 cm²). The average peak pressure was 3.2 MPa under 600 N of applied load and the pressure in the anterior articulation was a little higher than that in the posterior articulation.

The distal radioulnar joint pressure was measured by Werner [97] before and after radial shortening and ulnar lengthening, which are treatments for Kienbock's disease. They used pressure sensitive film to measure the pressure in six cadaveric elbows and found that the average peak pressure was 2.5 MPa before treatments and increased by up to 3.3 MPa after treatment.

Takatori et al. [101] measured humeroradial joint contact stresses using pressure sensitive film and a tactile sensor with the arm positioned in neutral, full pronation, and full supination under axial loads of up to 50 kg. They used five formalin preserved cadaveric elbows for the loading experiment instead of fresh frozen elbows due to the difficulties getting specimens in Japan and created an FE model from one of the arms' CT scans. Peak contact stresses of 0.55 MPa, 1.13 MPa, 1.72 MPa, 2.29 MPa, and 2.86 MPa were measured in the neutral arm position under loads of 10 kg, 20 kg, 30 kg, 40 kg, and 50 kg, respectively. There was a linear relationship between the peak contact stresses and the applied load. However, since they tested formalin preserved elbows instead of fresh frozen elbows, which resulted in altered elastic properties for soft tissues, the peak

stresses might be lower than actual pressures. Additionally, some of the loads were distributed through the humeroulnar joint as well as humeroradial joint.

Chantelot et al. [102] measured intra-articular stress and contact area of the elbow in extension using Fuji film. From 1 to 10 kg of loads in steps of 1 kg were applied to the proximal humerus with the distal radius and ulna fixed. Thirty formalin-preserved cadaveric elbows were tested in three forearm rotations (neutral, pronation, and supination). They reported that the maximal pressure of the radial head occurred in neutral forearm position and minimal pressure occurred on the supination position. They did not provide the absolute values of either articular pressure or contact area. Diab et al. [103] also measured radiocapitellar joint pressure and contact area before and after the radial shortening osteotomy of 2 to 3 mm. Five fresh frozen elbows were tested in full extension with three different loads (45, 90, and 135 N) and three forearm positions (neutral, pronation and supination). They found that the mean radiocapitellar force and contact area decreased significantly for all cases after radial shortening except pronation at 45 and 90 N of applied load. They did not also provide contact pressure.

Moungondo et al. [104] investigated the change in contact area before and after bipolar radial head replacement. Using molding material, six frozen elbows were examined at three flexion angles (30°, 60°, and 90°) and three forearm positions (supination, neutral, and pronation). Total 98 N of load was applied to the tendons of biceps, brachialis, and triceps. They found that the average contact area was 82 mm², decreasing with elbow flexion and pronation, whereas the average contact area after radial head replacement was 62 mm². Liew et al. [105] tested eight elbows to determine the effect of radial head replacement and implant size on the radiocapitellar contact area using impression material. They tried three different sizes of implant (Evolve) with three flexion angles at neutral forearm rotation under compressive load of 100 N. They reported

that the contact area decreased after radial head replacement by approximately two thirds relative to the native elbow, and smaller implants produced slightly larger contact areas. In addition, the contact area decreased with larger flexion angle, which concurs with the work of Mounghondo et al [104].

Sabo et al. [106] examined the effect of the capitellar arthroplasty on elbow contact area. They used eight elbows flexed 45° in neutral forearm rotation under compressive load of 85 N to compare spherical and anatomical capitellar implants relative to the native joint and found that the contact areas for anatomical and spherical implants were 59 and 51% of the native articulation.

Van Glabbeek et al. [107] measured radiocapitellar contact pressure using pressure sensitive film to assess the effect of radial head lengthening and shortening. They tested six cadaveric medial collateral ligament deficient upper extremities at four flexion angles (0° 30°, 60°, and 90°) and three forearm rotations (pronation, neutral, and supination) and found significant increase in contact pressure after 2.5 mm of lengthening of the radial head.

3.2 MONOBLOCK VS BIPOLAR

There are two basic types of radial head implants based on different concepts: a loose monoblock implant and a bipolar implant. Most monoblock implants with a smooth polished stem are intentionally loose in the intramedullary canal, which would allow small movement of the stem inside the bone and provides more congruent contact between the implants and the capitellum of the humerus [88, 108]. On the contrary, bipolar implants are constrained in the radius and its ball

and socket type joint provides additional DOF which possibly makes the implant contact the capitellum more congruently [88].

The orthopaedic literature contains several clinical reports concerning the midterm or long term results of radial head arthroplasty with either monoblock [109] or bipolar implants [86, 88]. However, there is little information about direct biomechanical as well as clinical comparison between the monoblock and bipolar implants. There were a couple of studies where two different implants were compared in terms of elbow joint stability. Pomianoski et al. [110] examined the valgus stability using nine cadaveric elbows with no medial collateral ligament treated with three different radial head implants: the Wright monoblock titanium implant, the KPS bipolar cobalt-chrome alloy implant, and the Judet bipolar cobalt-chrome implant. An electromagnetic tracking device was used for quantification of valgus stability. Their study showed that there was no difference in valgus stability in an MCL deficient elbow between monoblock and bipolar radial head implants. None of them, however, were as effective as the native radial head. Moon et al. [90] tested radiocapitellar joint stability with monoblock and bipolar radial head implants, using twelve cadaveric elbows without soft tissues. Subluxation forces for native radial head, monoblock implant, and bipolar implant were measured at three different flexion angles (30°, 60°, and 90°) under three different compressive loads (25, 50, and 75 N). They found that the native radial head and the monoblock implant resisted subluxation whereas the bipolar implant did not. It was also reported that the monoblock implant was not as good as the native radial head in resisting subluxation. There were some limitations to this study because they used only a specially constrained bipolar implant and assumed it to be a monoblock implant. Thus, the difference in geometry such as radius of curvature between a monoblock and bipolar implants was not

considered. Furthermore there were no soft tissue constraints such as joint capsule, annular ligament, UCL, and LCL in the experiments.

3.3 CLINICAL OUTCOMES OF RADIAL HEAD REPLACEMENT

There have been several studies of clinical outcomes of radial head replacement from short to long-term. All of them concluded that radial head replacement was successful in the treatment of irreparable radial head fractures despite major complications such as prosthetic loosening, heterotopic bone formation, neuropathy, and wrist pain.

Harrington et al. [9] reviewed 20 patients with a mean follow-up of 12.1 years (6 to 29 years) using a modified Mayo Clinic functional rating index system. Patients expressed subjective satisfaction in terms of pain, motion, elbow strength, and functional index. Scores ranged from 67 to 100 and showed excellent in 12, good in 4, fair in 2, and poor in 2 patients.

Lim et al. [111] assessed 6 patients with mean follow up of 29.7 months (13 to 54 months) using American Shoulder and Elbow Surgeons (ASES) score, Disabilities of Arm, Shoulder and Hand score (DASH) and Broberg and Morrey Performance Index. Results were excellent for 1, good for 3, fair for 1 and poor for 1 patient based on Broberg and Morrey Performance Index, which corresponded well with DASH score.

Chien et al. [112] investigated 13 patients with mean follow up of 38 months (20 to 70 months). Based on the Mayo Elbow Performance Score, 8 patients had excellent results (good for 3 and fair for 2).

Brinkman et al. [86] reviewed 11 patients who were treated with a bipolar radial head implant. Outcome was assessed clinically by two standardized elbow function assessment scales

and radiographically after 2 years of a mean follow-up. They reported that all the patients were clinically either excellent or good and there were no signs of loosening, fracture or heterotopic ossification.

Burkhart et al. [113] examined 17 patients after 106 months (78 to 139 months) based on Mayo Elbow Performance Score. All the patients were treated with Judet bipolar radial head implant. Results were excellent for 6, good for 10 and fair for 1 patient. Average flexion was 124° and extension deficit was 21° . Pronation and supination were 64° . Several complications were seen including dislocation, erosion, and degenerative change of capitellum.

Most of clinical outcome literature indicated that radial head replacement has been successful for most of patients even though there have been some major complications found.

3.4 FE MODELING OF HUMAN JOINTS

FEM has been used for calculating stresses in hip and knee joints more frequently than other joints and three examples can offer a brief overview of the basic premises in previous work. Huiskes et al. [114] evaluated interface stresses in the resurfaced hip. They created a two dimensional FE model which included bone, PMMA, and the acetabular cup using axisymmetric ring elements and found abnormal stress patterns in the femoral head and at the implant-bone interfaces. Contact stress analysis of the hip joint was conducted by Rapperport et al. [115] who constructed simplified a two dimensional FE model, which included the pubis, acetabulum, and ilium, and used contact elements to calculate contact stresses. They examined intraarticular pressures and principal stresses in three different sets of boundary conditions: 1) deformable pubic symphysis, 2) rigid pubic symphysis, and 3) simulations of experimental studies previously done by other researchers.

Hopkins et al. [116] examined changes on kinematics and potential cartilage damage in the knee joint after implantation of an Oxford Mobile Bearing unicompartmental knee arthroplasty (UKA). They developed three FE models, the intact knee, the medial UKA, and the lateral UKA model, and found additional posterior translation of the tibia for the lateral UKA model which might cause higher rates of bearing dislocation observed in some clinical studies.

FEM has been also used for elbow joint analysis even though the amount of the literature is not as extensive as that for the hip and knee joints. Wake et al. [117] constructed a two dimensional humeroulnar joint model including cartilage and applied axial displacement on the proximal end of the humerus with 0° , 30° , 60° , and 90° of flexion. Bones were divided into three volumes: cortical, cancellous, and subchondral and modeled separately. It was found in their study that areas of stress concentration moved from the coronoid process to the olecranon as the elbow flexed.

Takatori et al. [101] created a three dimensional bone model of the elbow joint from CT scans. All three bones were assumed to consist of only cortical bone; cartilage was not included in their FE model. Assigned displacements were applied at the distal ends of the radius and the ulna. They found that contact stress was concentrated laterally in supination and medially in neutral and pronation positions.

Recently Tarnita et al. [118] created a full upper extremity FE model. The model included ligaments, and muscles around the elbow joint as well as the three bones, but again cartilage was not included. The results from the FE model were not included.

3.5 CARTILAGE THICKNESS

Cartilage thickness varies depending on animals, joints and locations within joints. It has been measured in many ways including a needle probe system, MRI, and laser scanner to identify the characteristics of the cartilage. Cartilage thickness ranges from 0.023 mm (mouse ankle) to 6.25 mm (human knee) [119, 120]. It has been observed that cartilage thickness decreases with age [47] [121].

Schenck [41] and Springer [45] have investigated cartilage thickness in the elbow. Schenck et al. studied 12 cadaver elbows to identify the characteristics of the radiocapitellar cartilage. They isolated the radiocapitellar joint. The radius and capitellum were divided into five (anterior, posterior, central, medial, and lateral) and six sections (superolateral, superomedial, middlelateral, middlemedial, posterolateral, and posteromedial) respectively. The thickness of each section was measured using a needle probe system along with other mechanical properties, compressive stiffness, Poisson's ratio, and permeability. For the radial head, average cartilage thickness was approximately 1 mm. The center was somewhat thinner than other sections. Average cartilage thickness of the capitellum was 1.0 mm for the superior sections and 1.3 mm for middle and posterior sections, which was thicker than average cartilage thickness for the radial head. Springer et al. [45] measured cartilage thickness in the elbow joint using MR imaging. They reported the average thickness ranged from 0.9 (proximal part of the ulna) to 1.4 mm (capitellum) and the ulna had more inhomogeneous cartilage thickness distribution than the radius and humerus.

4.0 NATIVE RADIAL HEAD FE ANALYSIS

In order to examine the effect of radial head implant on the contact patterns in the elbow joint, an FE model for a native elbow was constructed and analyzed under various loading conditions. Contact stresses in the humeroradial and radioulnar articulations were investigated along with contact areas calculated using MATLAB (The MathWorks, inc., Natick, MA) from the FE results. An appropriate mesh size for cartilage was determined by the convergence of results from six different mesh sizes. Sensitivity studies of cartilage thicknesses, cartilage stiffness and material properties for ligaments were included.

4.1 CREATION OF THE 3-D ELBOW MODEL

An FE model for the elbow joint was created from CT (X-ray Computed Tomography) scans of a female 46 year old left cadaveric elbow. The elbow was in neutral supination/pronation position and flexed at 90°, which is the posture when one pushes and twists. All the CT images were exported into Mimics 12.0 medical imaging software (Materialise, Leuven, Belgium) to obtain the surface geometry of the three relevant bones (humerus, radius and ulna). Using predefined threshold for bones in Mimics, which is 226 to 2572 of Hounsfield units, only bones were selected in the CT scans. The Hounsfield unit is an arbitrary number of X-ray attenuation used for CT scans; water is 0. Each bone was then separated by manually removing erroneous connections between them in every slice of CT scans and selecting each bone one by one using different masks. The point cloud on the 3-D surface of each bone was generated by merging all the slices of CT

scans and saving the result as an IGES file. The point cloud for each bone was exported into Geomagic studio (Geomagic inc., Triangle Park, NC) and 3-D surfaces were generated and then smoothed by eliminating spikes and reducing noise. Volumes for each bone were generated based on the surfaces and exported into Solidworks 2009 (SolidWorks Corp, Concord, MA). Figure 12 shows a 3-D solid model of the three bones extracted from the CT scans. Cartilage was generated and added in the humeroradial and radioulnar articulations in SolidWorks because the exact shape of it could not be obtained from plain CT scans since cartilage does not absorb X-rays under normal in vivo conditions. However, CT arthrography can show good visualization of cartilage due to the contrast between low-density cartilage and high-density intra articular contrast medium [122]. Cartilage on the radial head and ulna was assumed to have 1.0 mm uniform thickness whereas cartilage on capitellum side assumed to be 1.2 mm uniform thickness. Zero offset surfaces were added over each bone where contact could take place and then thickened as needed. The bones far from the contact surfaces were excluded from the model for the efficiency of the computation. Each bone with cartilage was saved as separate IGES files for the exportation into Finite Element analysis program, ANSYS.

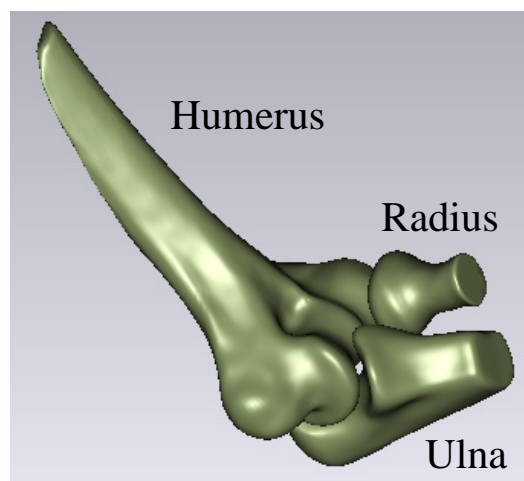


Figure 12. 3-D solid model of the elbow

4.2 FE MODEL DESCRIPTION

The finished 3-D solid model was exported into ANSYS 11.0 (ANSYS Inc., Canonsburg, PA) for meshing. The *X* axis (medial-lateral) was defined as the line connecting the medial and lateral epicondyles of the humerus. The *Z* axis (anterior-posterior) represented the loading direction from the radial head towards capitellum of the humerus. The *Y* axis (superior-inferior) was determined automatically by the *X* and *Z* axes, which was a little off from the long axis of the humerus. Bones and cartilage were meshed with 3-D 10 node tetrahedral elements. Annular and lateral ligaments were added using 2-D spring elements. Using automatic meshing, cartilage was first meshed with smaller elements and bones were then meshed with larger elements relative to the cartilage since the focus in this study was the contact stress of cartilage and bones are much stiffer material than cartilage. The bone immediately beneath the cartilage was refined to avoid any abrupt change of element size between the bone and cartilage interface. Six different element sizes for cartilage were tested to find the optimal element size.

For the calculation of normal contact stresses in the humeroradial articulation, a layer of 2-D contact elements was generated over the cartilage of the humerus and a 2-D target element layer was created over the cartilage of the radius. For the radioulnar articulation, contact and target element layers were added on the medial side of the radial head and ulnar notch respectively. The coefficient of friction was assigned to be zero for the contact region [77, 115, 123-125] since the friction coefficient between cartilages is low. Default values for normal penalty stiffness and penetration tolerance were used. The augmented Lagrangian algorithm was chosen for the contact algorithm, which is the default in ANSYS. Three straight line spring elements were used to model the annular and lateral ligaments (See Figure 13). All three bones were modeled as cancellous bone and linear elastic material properties were assigned. Ligaments and cartilage were modeled

as linear isotropic materials as well. All the material properties are shown in Table 2. As boundary conditions, the proximal end of the humerus was constrained in the Y (superior-inferior) direction and distal surface of the ulna was constrained in the Z (anterior-posterior) direction and three arbitrary nodes on both surfaces were constrained in all directions to prevent rigid body motion. All the nodes on the distal surface of the radius were coupled in the Z direction so that the surface did not rotate and remained perpendicular to the loading direction at all times. Loads were applied on the distal surface of the radial head. Contact stresses were calculated in the humeroradial and proximal radioulnar articulations. Figure 13 shows the FE model for the native elbow joint.

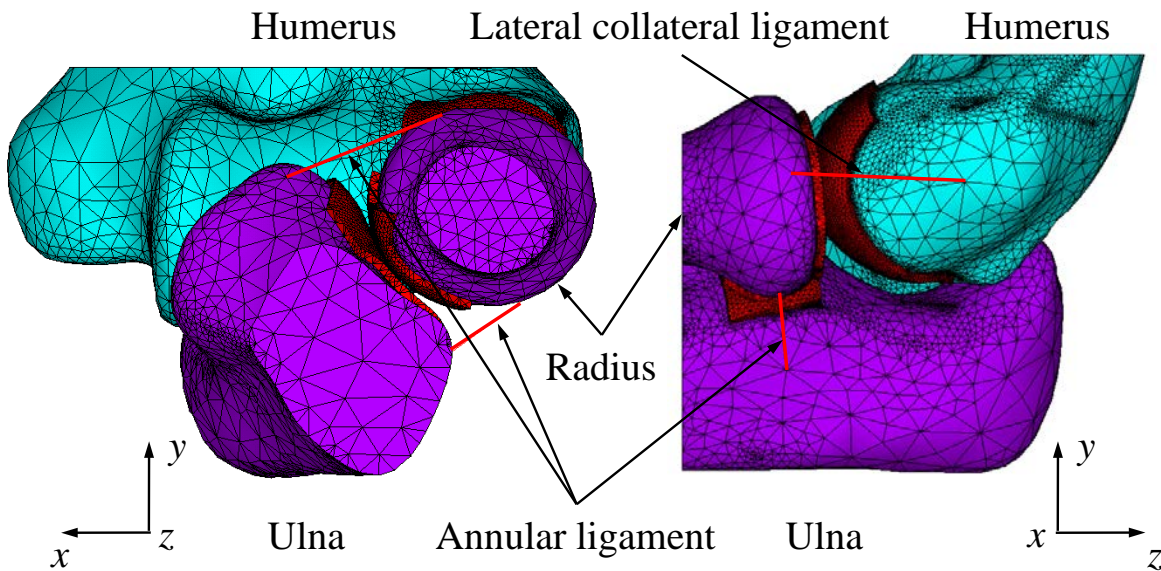


Figure 13. Front (left) and side view (right) of native elbow FE model mesh

Table 2. Material properties of the bone and soft tissues [37] [126]

Part	Elastic modulus (GPa)	Poisson's ratio
Cancellous bone	0.4	0.3
Cortical bone	$E_x=E_y=7.0, E_z=11.5,$ $G_{xy}=2.6, G_{yz}=G_{zx}=3.5$	$\nu_{xy}=\nu_{zy}=\nu_{zx}=0.4$
Cartilage	0.01	0.4
	Spring stiffness (N/mm)	
Annular ligament	28.5	
Lateral collateral ligament	15.5	

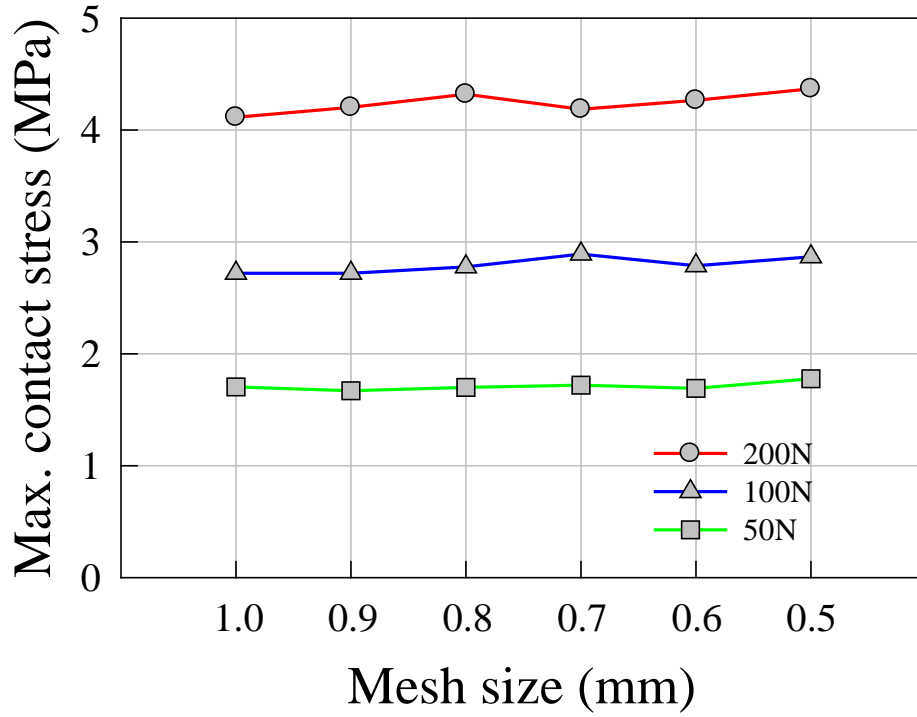
4.3 CONVERGENCE

For an initial evaluation, a native radial head was analyzed with an axial load with several different sizes of mesh and an optimal mesh size for cartilage was determined by examining convergence. In theory, FE results approach the analytical solutions as more elements are used. However, more computational resources and time are required as the model is refined. Thus, for an effective analysis, the appropriate mesh size from which reasonably good results can be obtained should be determined. Since the cartilage is a much softer material compared to the bone and stress is concentrated on the cartilage, mesh refinement was conducted mainly for the cartilage. In order to find the appropriate mesh size of the model, six different mesh sizes for the cartilage (1.0, 0.9, 0.8, 0.7, 0.6 and 0.5 mm) were tested under three axial loads, 50, 100, and 200 N. The number of the elements for six mesh refinements is shown in Table 3. The maximum contact stress was

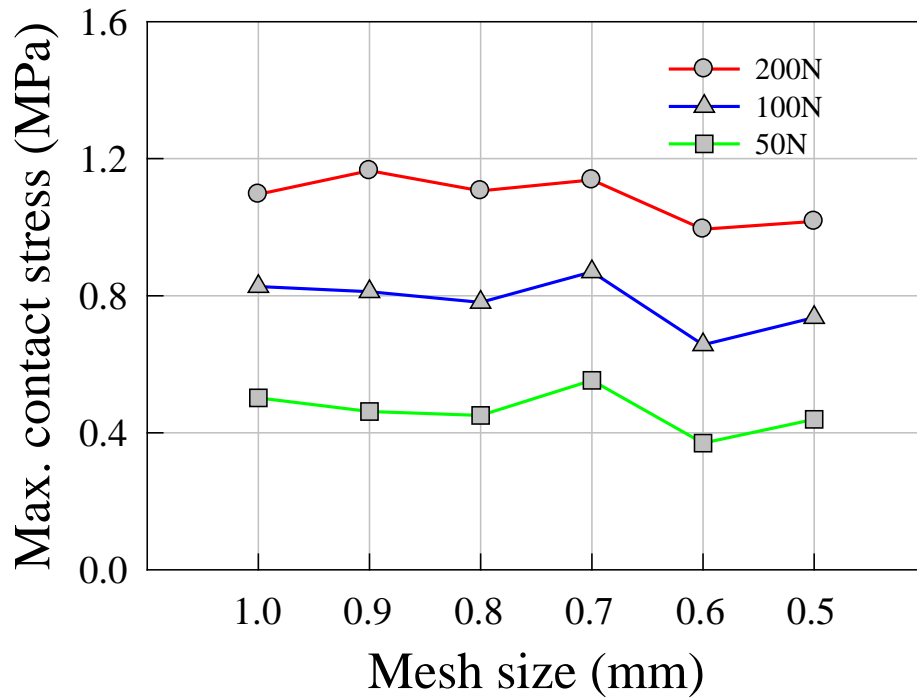
obtained directly from the FE analysis. Contact area and average pressure were calculated using a MATLAB code from FE results. The maximum stresses, contact areas and average pressures in the humeroradial and radioulnar joints with six different mesh sizes are shown in Figures 14, 15, and 16, respectively. The maximum contact stress increased from 1.7 MPa to 4.3 MPa for the humeroradial joint and from 0.4 MPa to 1.1 MPa for radioulnar joint as applied load increased from 50 N to 200 N. Contact area increased from 40 mm² to 77 mm² for the humeroradial joint and from 3 mm² to 8 mm² for the radioulnar joint. Average pressure ranged from 1.1 to 2.5 MPa for the humeroradial joint and from 0.3 to 0.6 MPa for the radioulnar joint. The maximum contact stresses, contact areas, and average stresses for the humeroradial joint did not exhibit much change whereas those for the radioulnar joint fluctuated as the mesh was refined. The FE model with 0.8 mm element size produced very similar results (maximum contact stress, contact area, and average pressure on the capitellum) to those from the finest mesh (0.5 mm), which can be considered as the closest to the analytical solution, with an average error of 2.14%. Results from 0.7 and 0.6 mm mesh sizes were slightly closer to results from 0.5 mm mesh model than those from 0.8 mm mesh model (errors were 2.06 and 1.74% respectively). Therefore, 0.8 mm was chosen to be an appropriate element size of the cartilage in terms of the convergence and analysis time and was therefore used for further analysis including sensitivity study. Contact stress distributions with 0.8 mm elements on the cartilage of the capitellum and radial head which contacted with ulnar notch are shown in Figures 17 and 18. An increase in contact area was observed as the applied load increased in both joints. The shape of the contact patches in both articulations was more elliptical, wider in the medial-lateral direction for humeroradial joint and wider in the anterior-posterior direction for radioulnar joint.

Table 3. Number of elements for 6 different meshes

Mesh size (mm) Element type		1.0	0.9	0.8	0.7	0.6	0.5
		3D tetrahedral	96987	102862	122919	146213	169491
Humeroradial joint	Target	1641	1875	2011	2477	2758	3225
	Contact	1095	1281	1614	1957	2629	3589
Radioulnar joint	Target	482	544	650	787	1018	1351
	Contact	1062	1311	1498	1756	2087	2692
Spring		3	3	3	3	3	3
Total		101270	107876	128695	153193	177986	244163

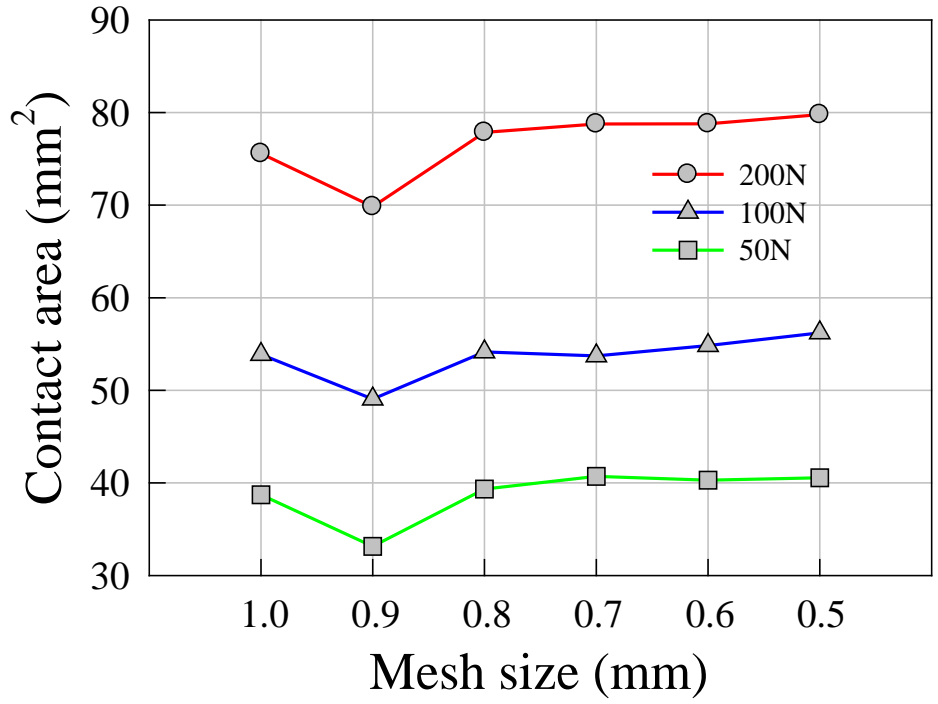


(a)

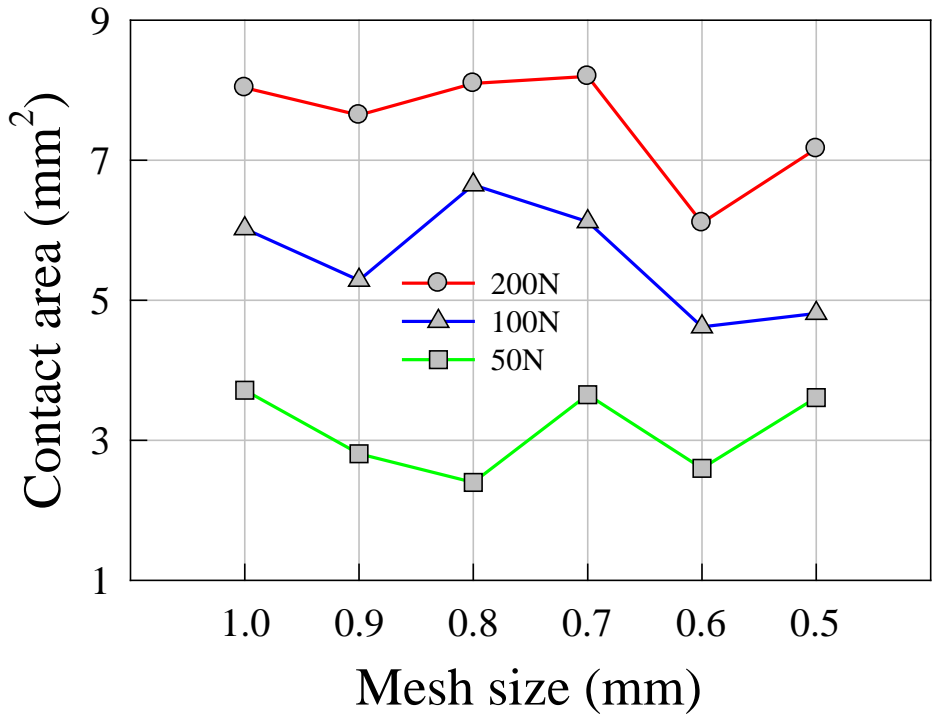


(b)

Figure 14. Maximum contact stress with different mesh size in (a) humeroradial and (b) radioulnar joints

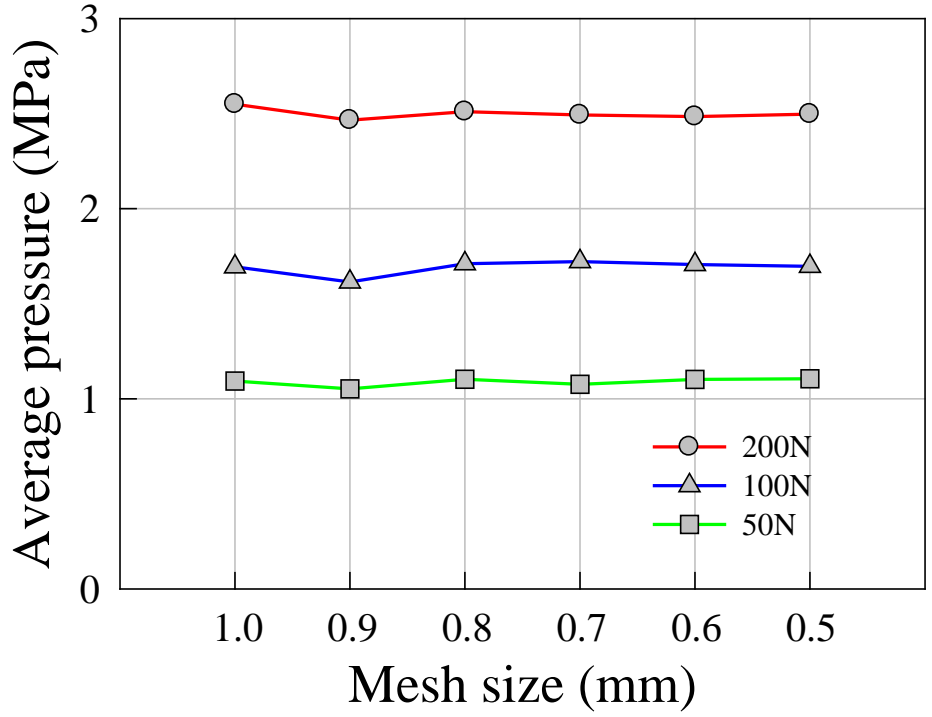


(a)

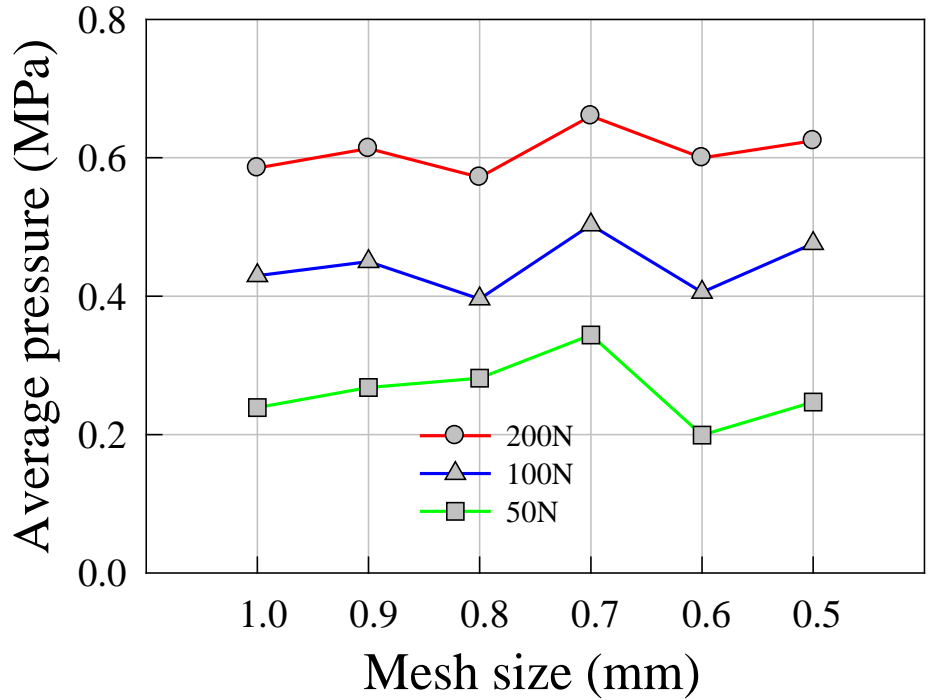


(b)

Figure 15. Contact area with different mesh size in (a) humeroradial and (b) radioulnar joints



(a)



(b)

Figure 16. Average pressure with different mesh size in (a) humeroradial and (b) radioulnar joints

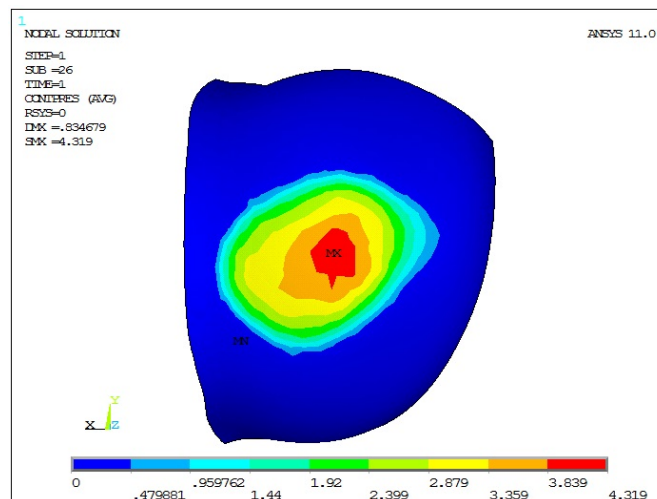
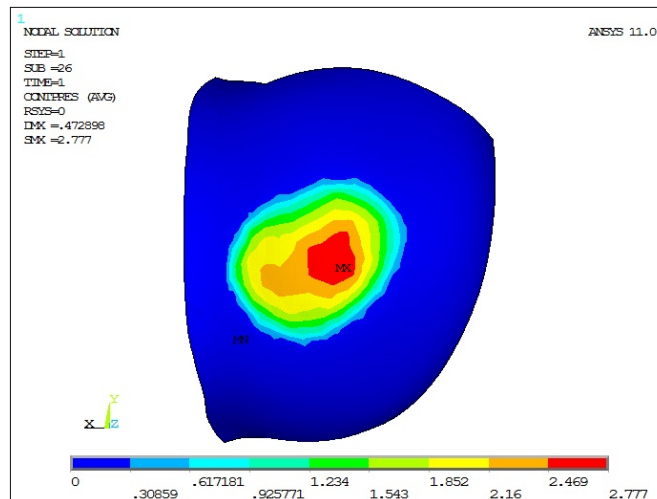
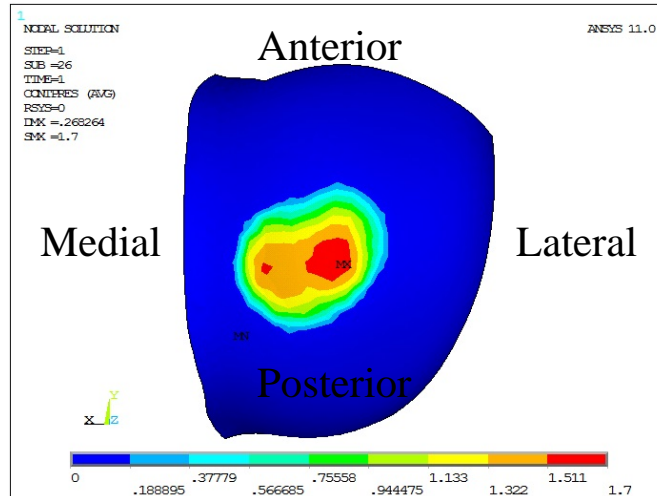


Figure 17. Contact stress distribution of capitellum under 50N (top), 100N (middle), and 200N (bottom)

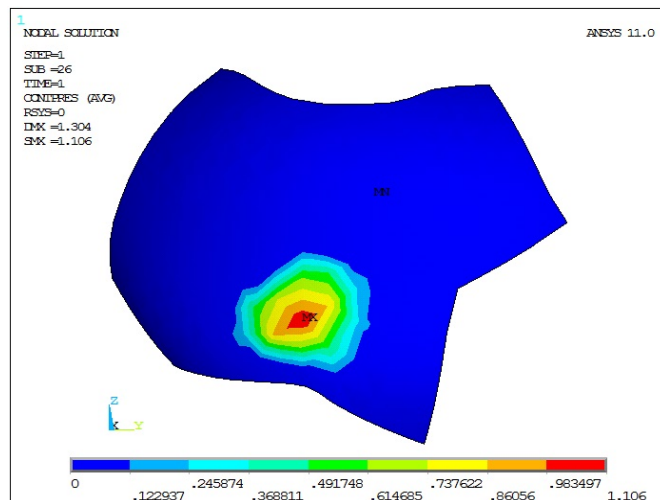
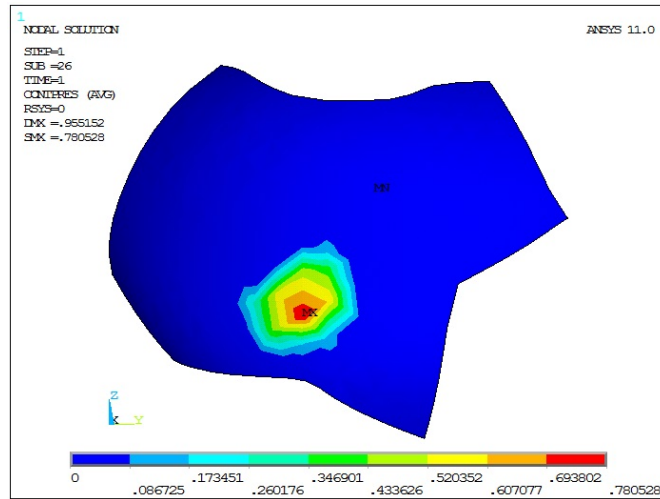
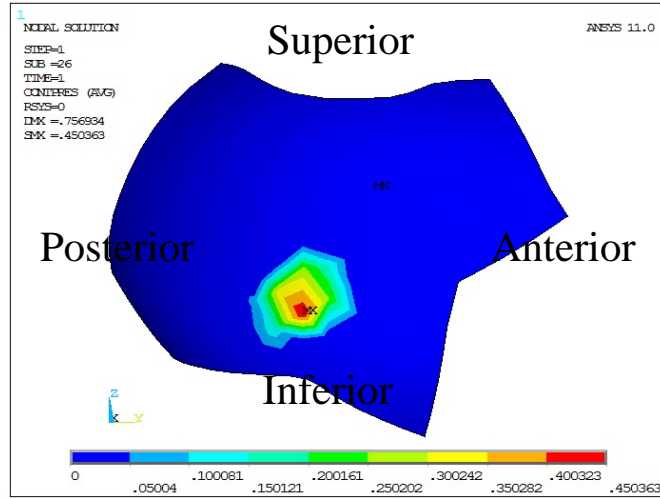


Figure 18. Contact stress distribution of radial head (medial side) under 50N (top), 100N (middle), and 200N

(bottom)

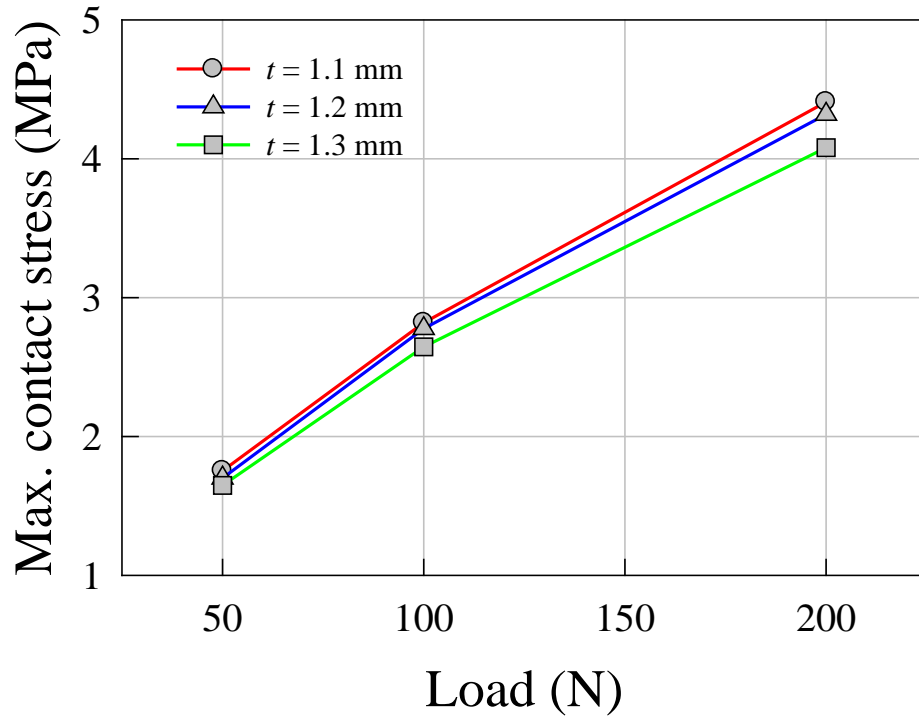
4.4 SENSITIVITY STUDY

Sensitivity analysis was performed to investigate how uncertainty in assumed inputs such as cartilage thickness, material properties for bone, cartilage, and ligament, affected predictions of cartilage contact mechanics.

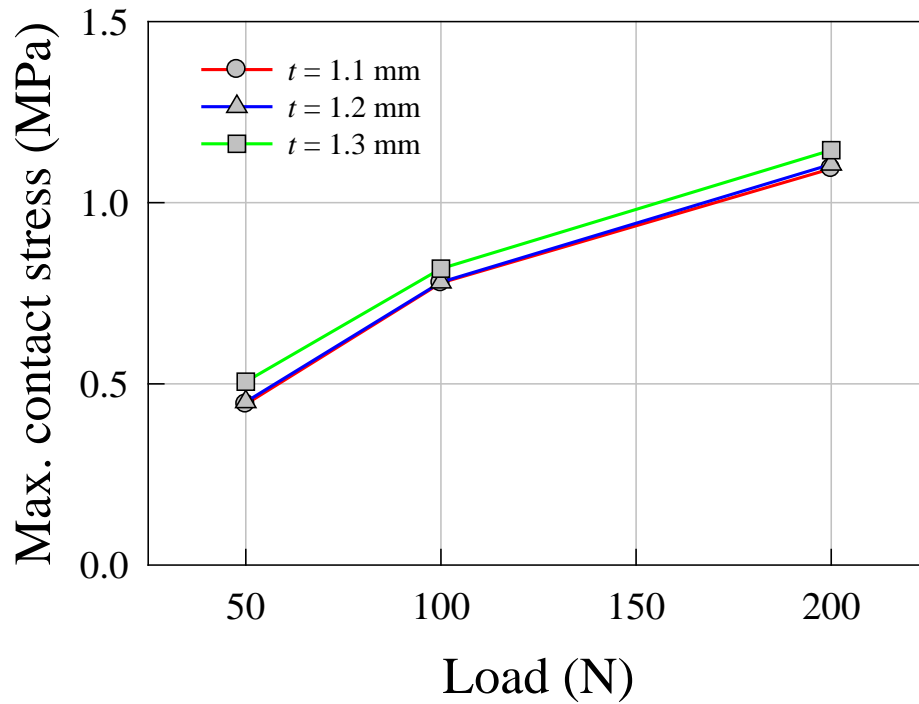
4.4.1 Cartilage thickness

One of the assumptions for the FE model in this study was that cartilage thickness was uniform. The thicknesses of 1.0 mm for radial head and ulna, and 1.2 mm for capitellum were assumed according to the findings by Schenck et al. [41] FE models with two other uniform cartilage thicknesses, 1.1 and 1.3 mm for capitellum and 0.9 and 1.1 mm for radial head, were created and analyzed to investigate the effect of the cartilage thickness on the contact stress and contact area. The maximum contact stress, contact area and average pressure in humeroradial and radioulnar joints with three different cartilage thicknesses of capitellum are compared in Figures 19, 20, and 21 respectively. With thicker cartilage on the capitellum, the maximum contact stress and average pressure for the humeroradial joint decreased and the contact area increased as expected. An increase of approximately 7% in maximum stress in the humeroradial joint was observed as cartilage thickness on the capitellum was decreased from 1.3 mm to 1.1 mm while contact area increased by 4.5%. Average pressure also increased by 5.6%. Unlike the maximum contact stress and average pressure in the humeroradial joint, those in the radioulnar joint increased with thicker cartilage. Contact areas in radioulnar joint did not change with different cartilage thickness for all three loading cases. Figures 22, 23, and 24 show the maximum contact stress, contact area, and average pressure in the humeroradial and radioulnar joints with three different cartilage

thicknesses of radial head respectively. The maximum contact stress and average pressure in the humeroradial joint increased by 7.5% and 3.8% respectively as cartilage thickness on the radial head decreased from 1.1 mm to 0.9 mm. Contact area in the humeroradial joint decreased by 3.54%. For the radioulnar joint, plots for the maximum contact stress, contact area, and average pressure did not show any trends especially with the change in cartilage thickness on the radial head side probably due to the change in initial contact region caused by different cartilage thickness in the radial head and movement of the radial head towards the capitellum during loading. Overall, change in cartilage thickness in capitellum and radial head produced similar differences in the maximum contact stress, contact area, and average pressure in humeroradial joint. Cartilage thickness reduction by 0.2 mm in either the humeral or radial sides caused approximately 7% increase in the maximum contact stress and less than 5% decrease in the contact area, which was not substantial.

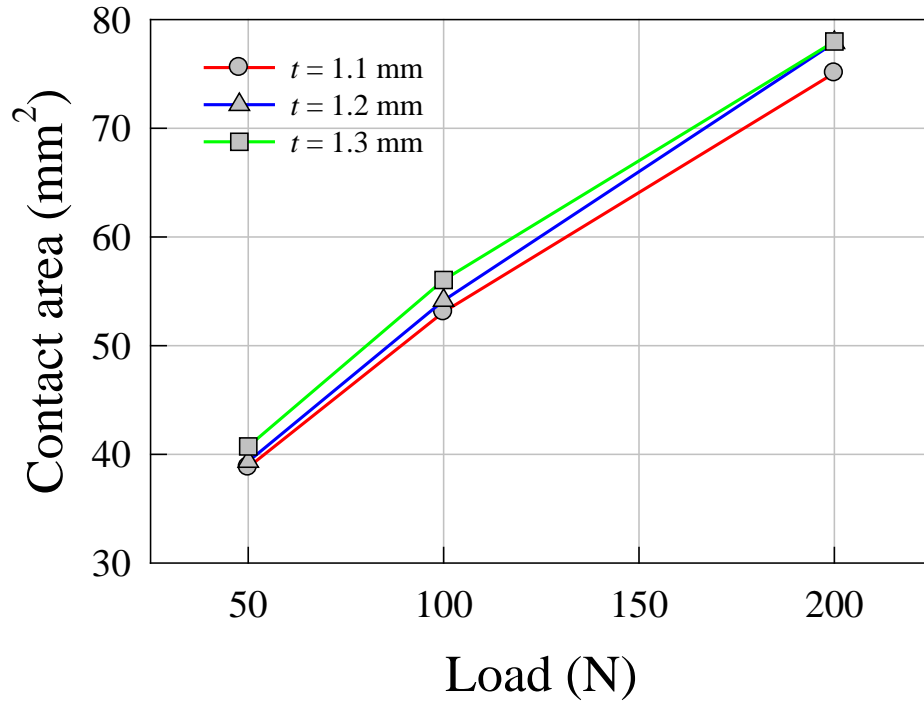


(a)

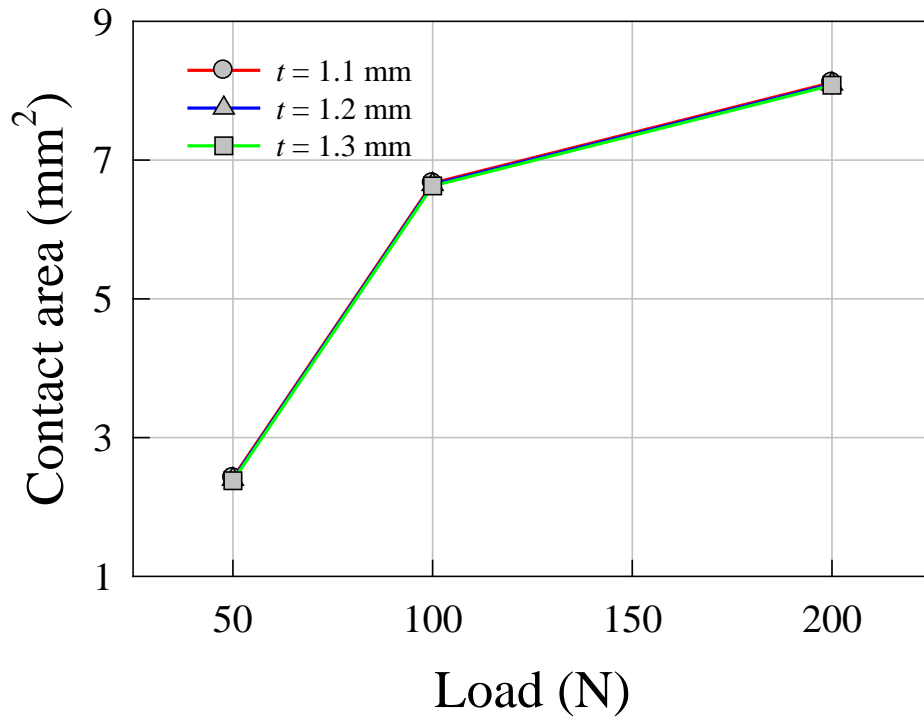


(b)

Figure 19. Maximum contact stress with different cartilage thickness on capitellum in (a) humeroradial and (b) radioulnar joints

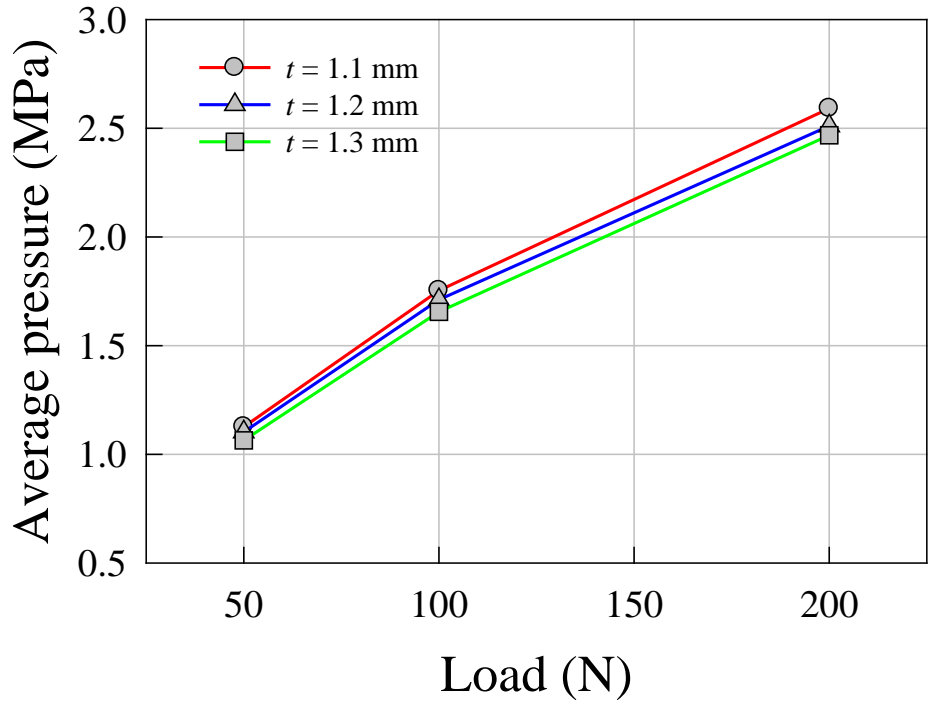


(a)

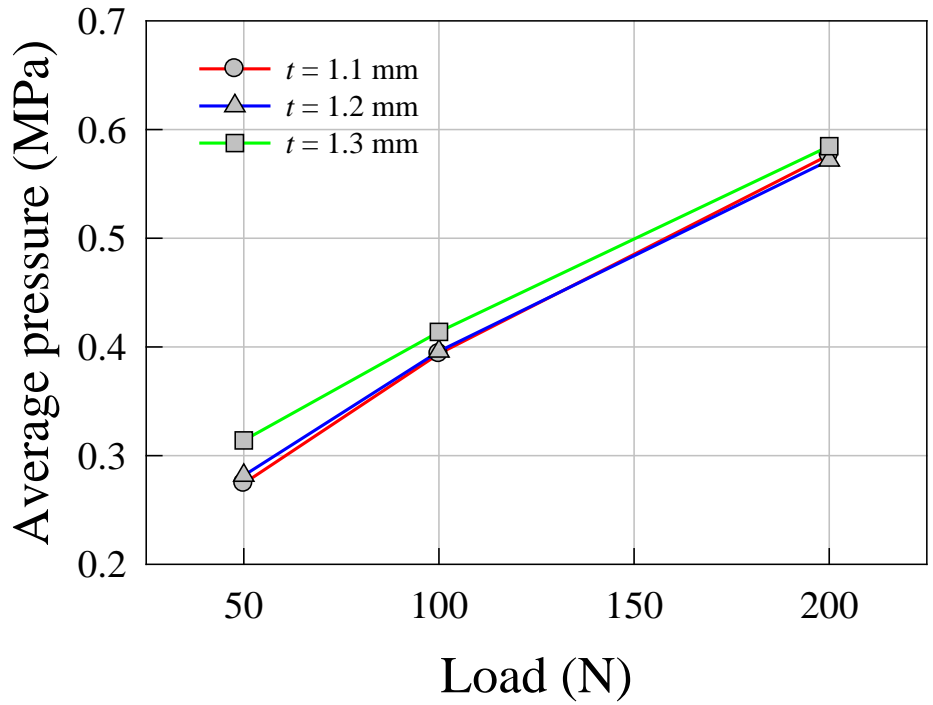


(b)

Figure 20. Contact area with different cartilage thickness on capitellum in (a) humeroradial and (b) radioulnar joints

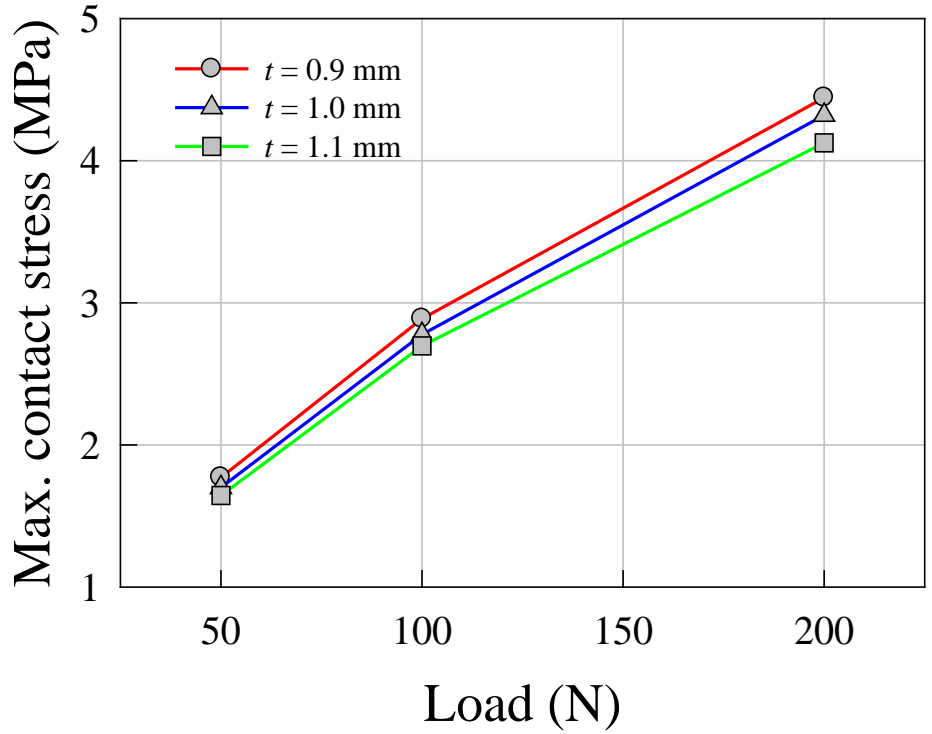


(a)

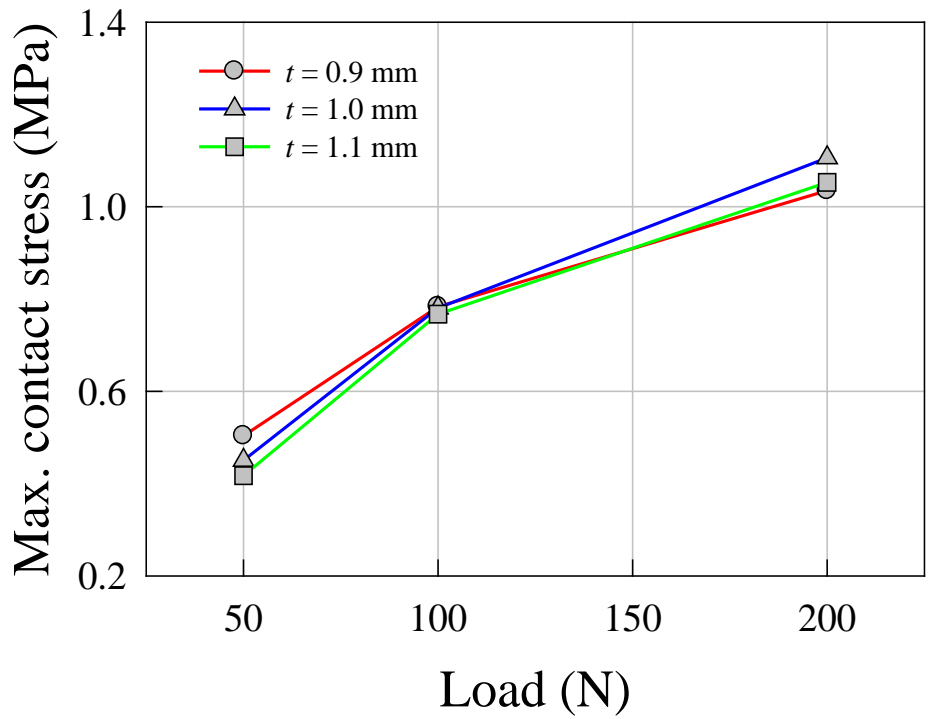


(b)

Figure 21. Average pressure with different cartilage thickness on capitellum in (a) humeroradial and (b) radioulnar joints

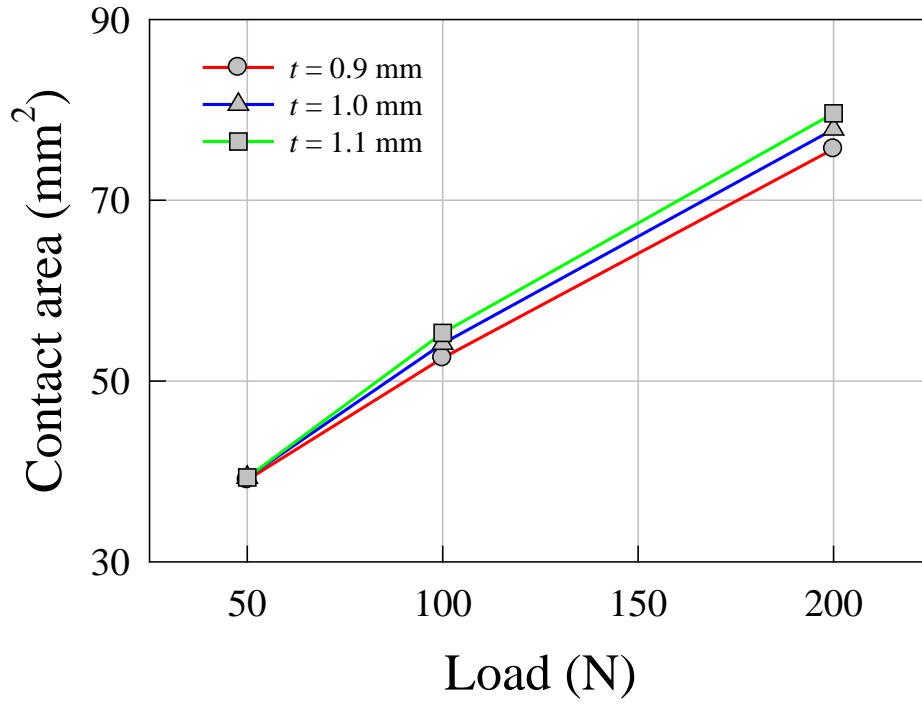


(a)

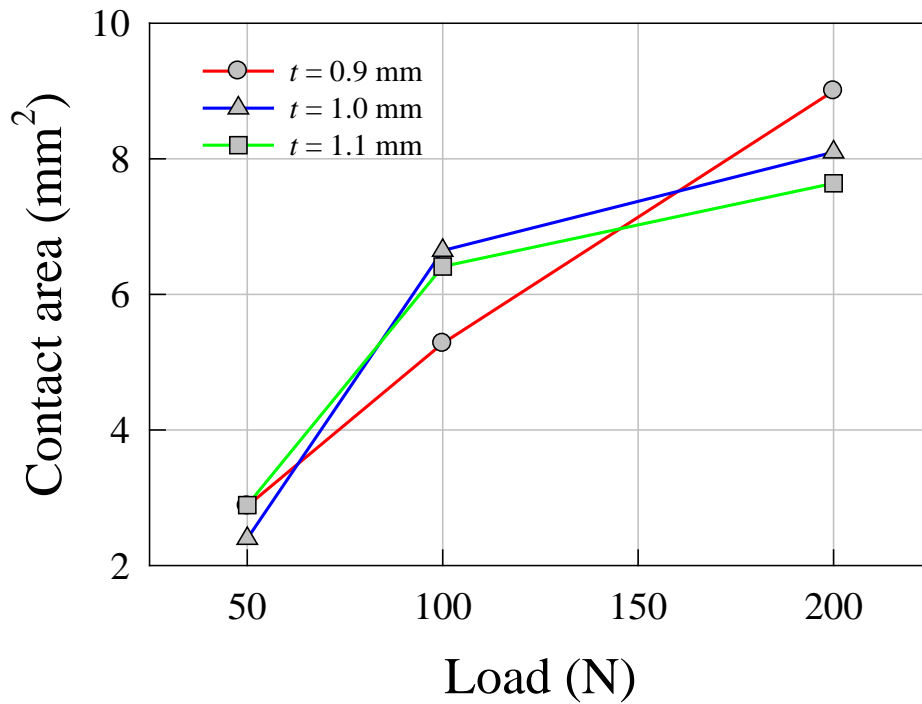


(b)

Figure 22. Maximum contact stress with different cartilage thickness on radial head in (a) humeroradial and (b) radioulnar joints

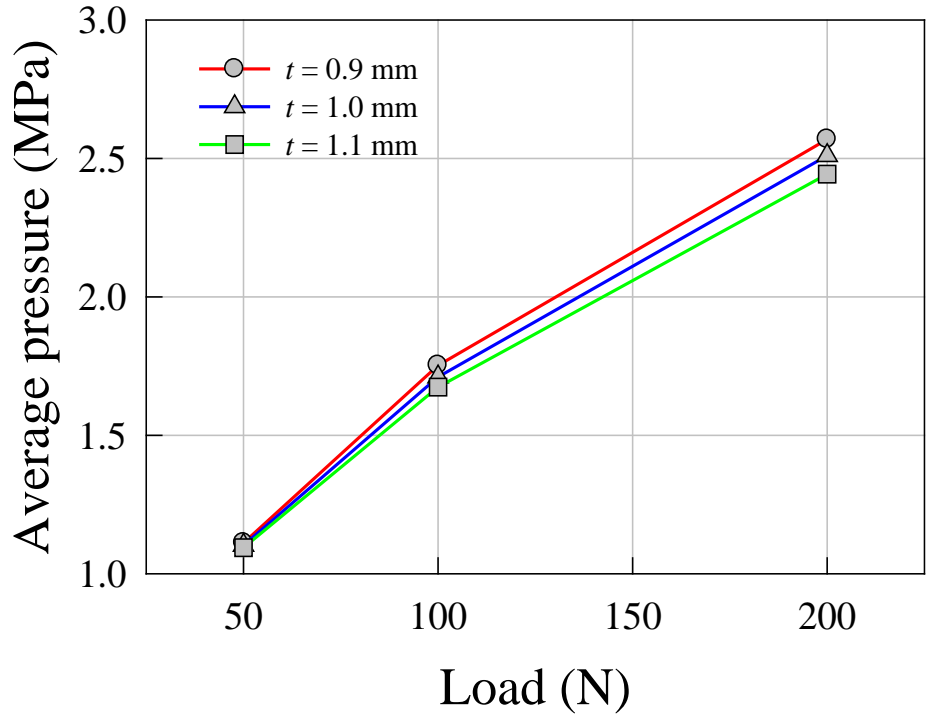


(a)

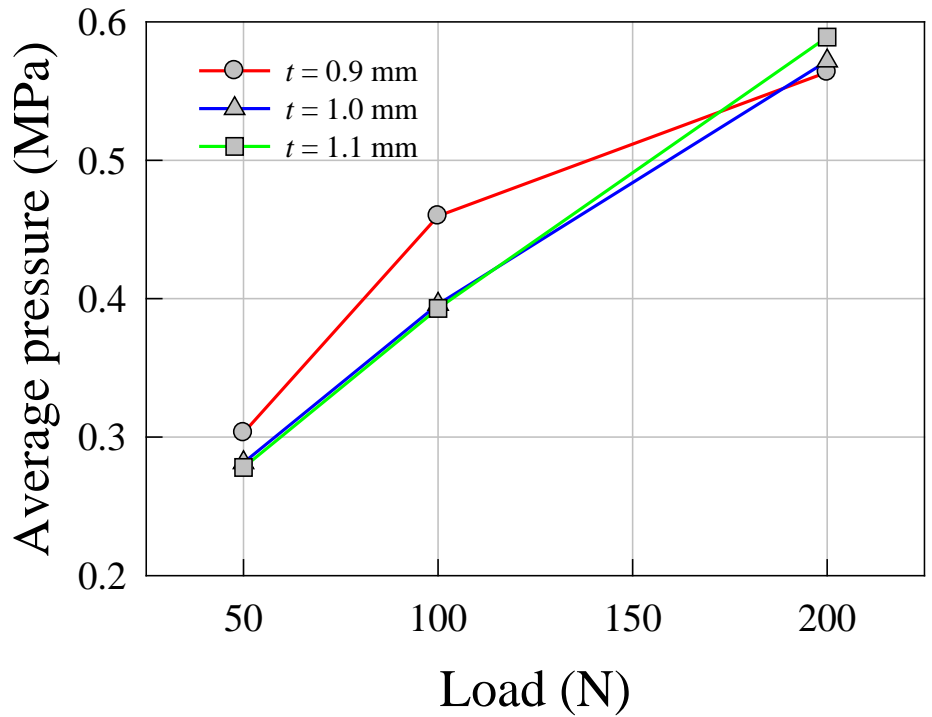


(b)

Figure 23. Contact area with different cartilage thickness on radial head in (a) humeroradial and (b) radioulnar joints



(a)

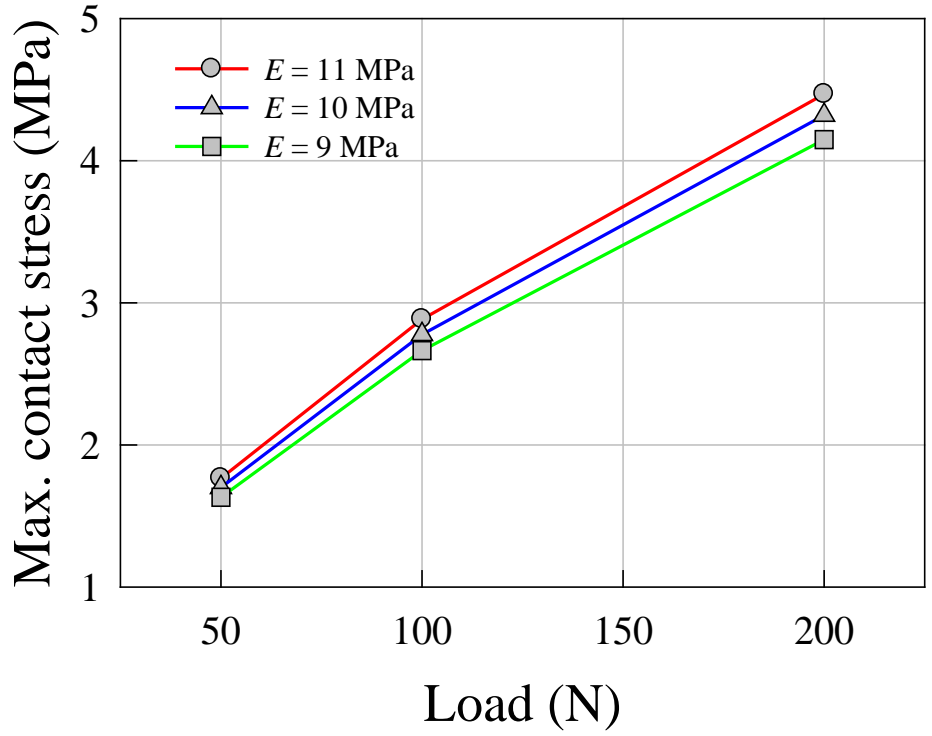


(b)

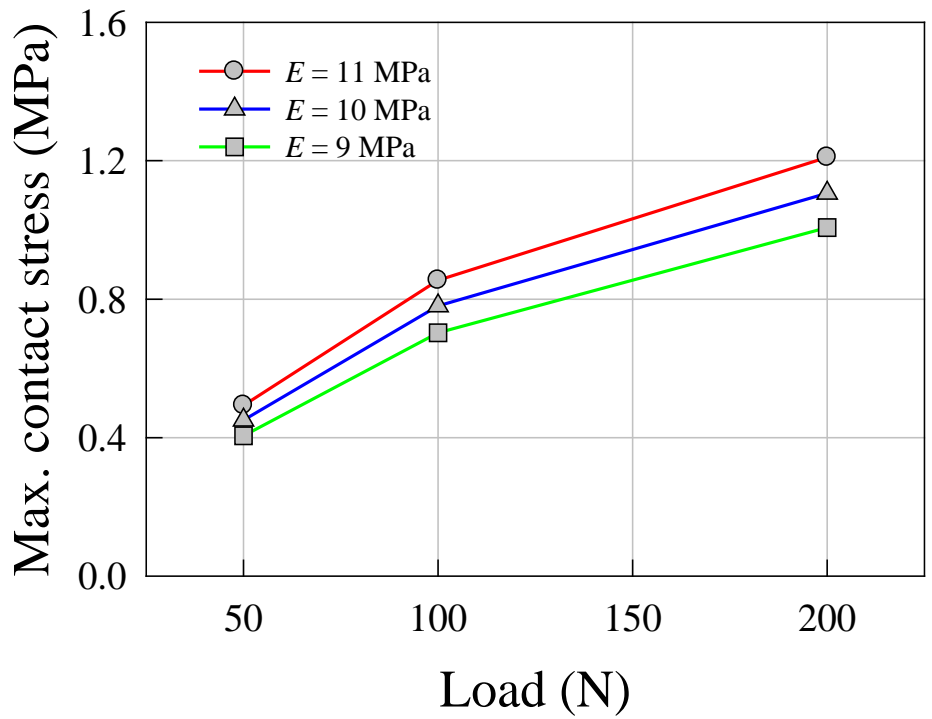
Figure 24. Average pressure with different cartilage thickness on radial head in (a) humeroradial and (b) radioulnar joints

4.4.2 Cartilage material properties

In the current study, cartilage was modeled as a linear elastic isotropic material and the stiffness of cartilage was determined only by its elastic modulus and Poisson's ratio. In order to investigate the sensitivity of cartilage stiffness on the FE results, 10% stiffer and 10% less stiff Young's moduli and Poisson's ratios were analyzed. The maximum contact stress, contact area and average pressure with three different Young's moduli (9, 10, and 11 MPa) for cartilage are shown in Figures 25, 26 and 27 respectively. The maximum contact stress and average pressure for humeroradial joint increased by approximately 8 and 7% respectively as Young's modulus increased from 9 to 11 MPa while contact area decreased by 6.3%. Differences in the maximum contact stress and average pressure for the radioulnar joint were approximately 21 and 24%, which was relatively higher than those for the humeroradial joint. However, there was no change in the contact area in the radioulnar joint for all three load cases. Figures 28, 29 and 30 represent maximum contact stress, contact area and average pressure with three different Poisson's ratios (0.36, 0.4 and 0.44) respectively. The maximum contact stress and average pressure for humeroradial joint increased by 15 and 11% respectively whereas contact area decreased by approximately 9% as Poisson's ratio increased from 0.36 to 0.44. The maximum contact stress and average pressure for the radioulnar joint increased approximately 30% while contact area remained same except 50 N with $\nu = 0.44$ and 200 N with $\nu = 0.36$. Overall, the maximum contact stress and average pressure were higher for cartilage and the contact area was smaller with higher Young's modulus and Poisson's ratio as expected. The difference in Poisson's ratio made slightly more effect on FE predictions than the difference in Young's modulus did.

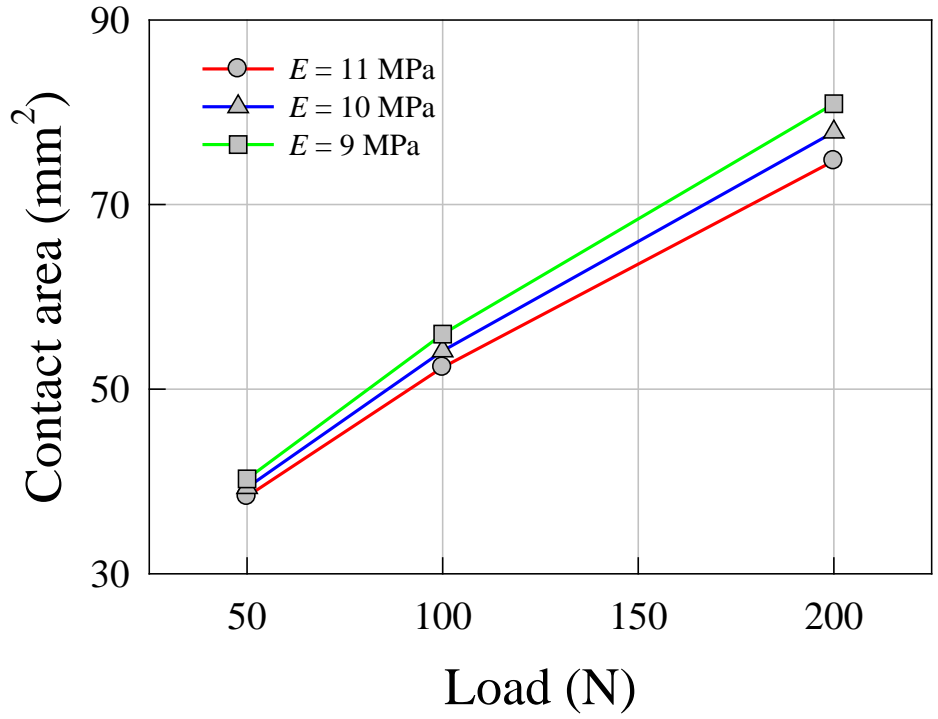


(a)

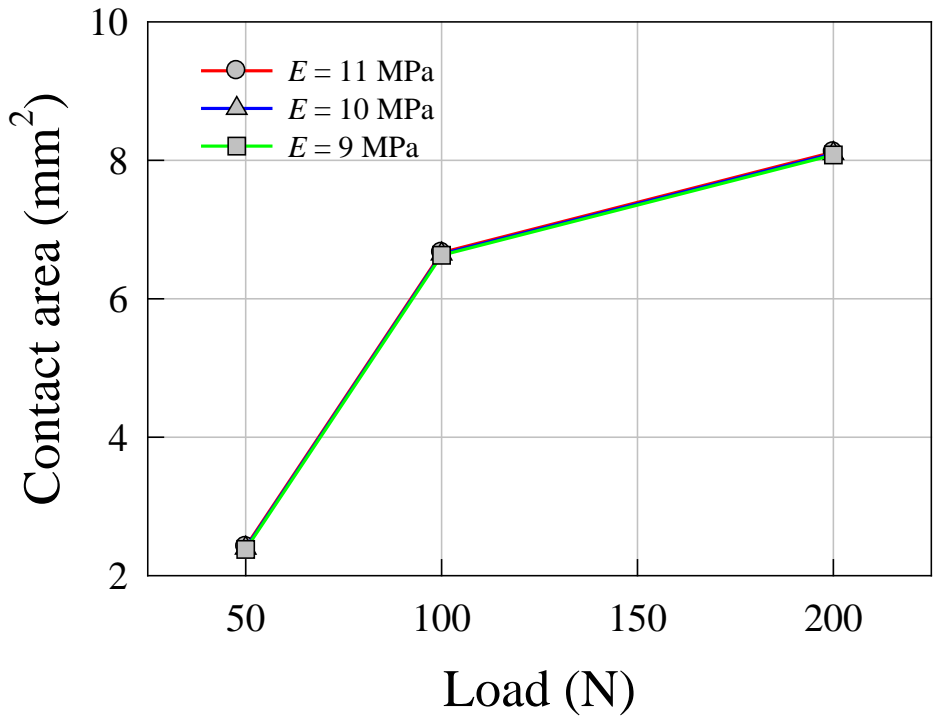


(b)

Figure 25. Maximum contact stress with different Young's modulus in (a) humeroradial and (b) radioulnar joints

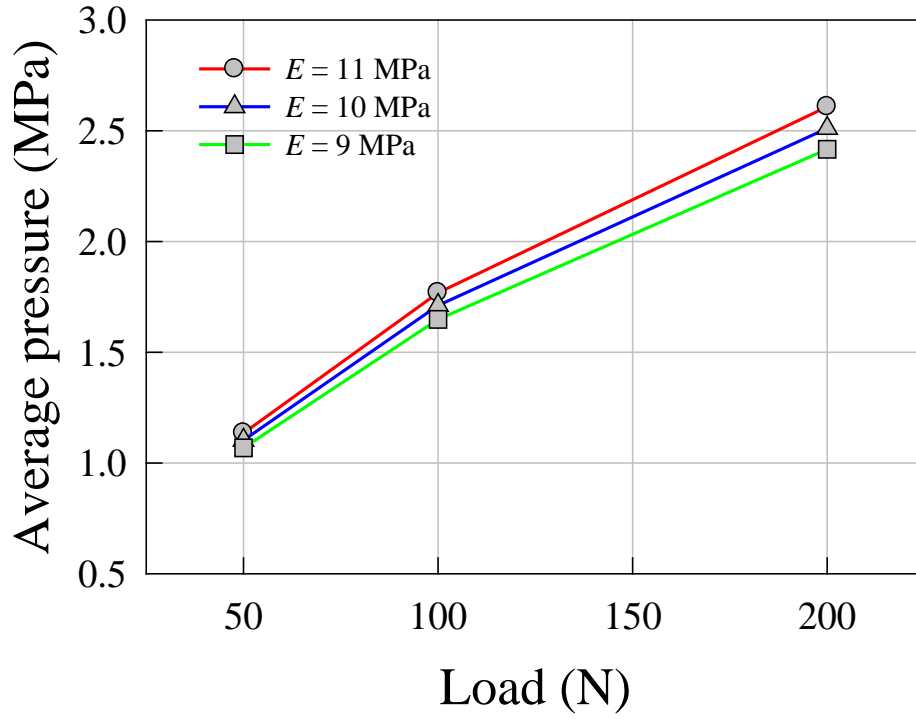


(a)

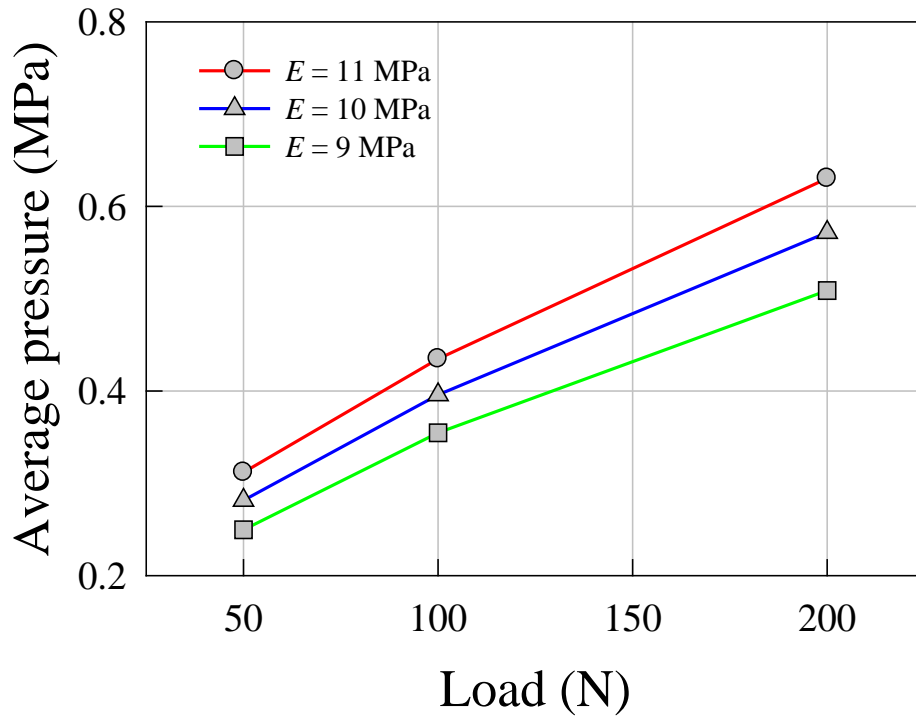


(b)

Figure 26. Contact area with different Young's modulus in (a) humeroradial and (b) radioulnar joints

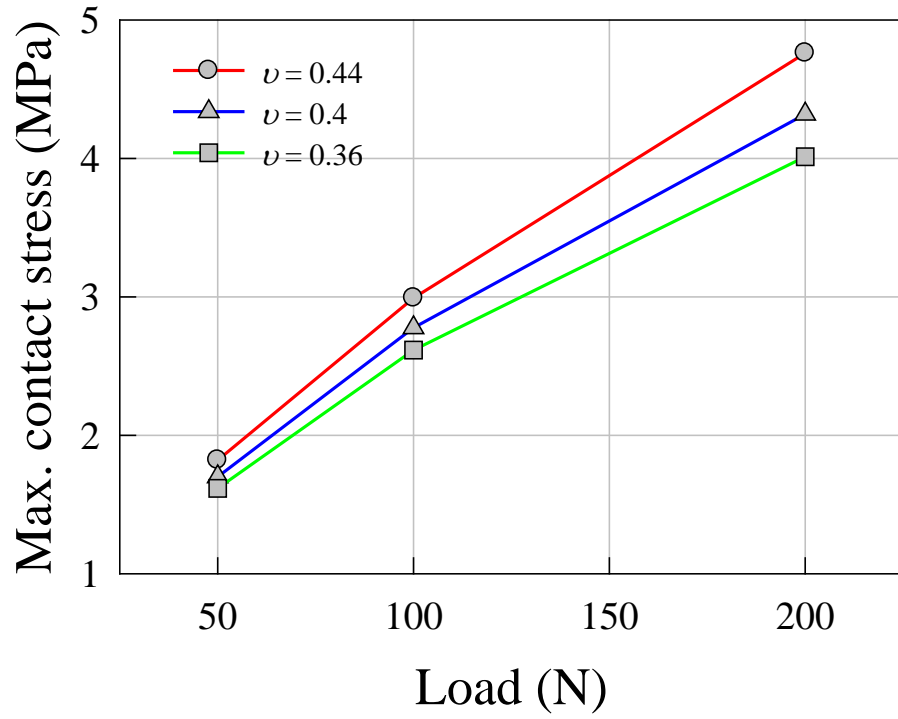


(a)

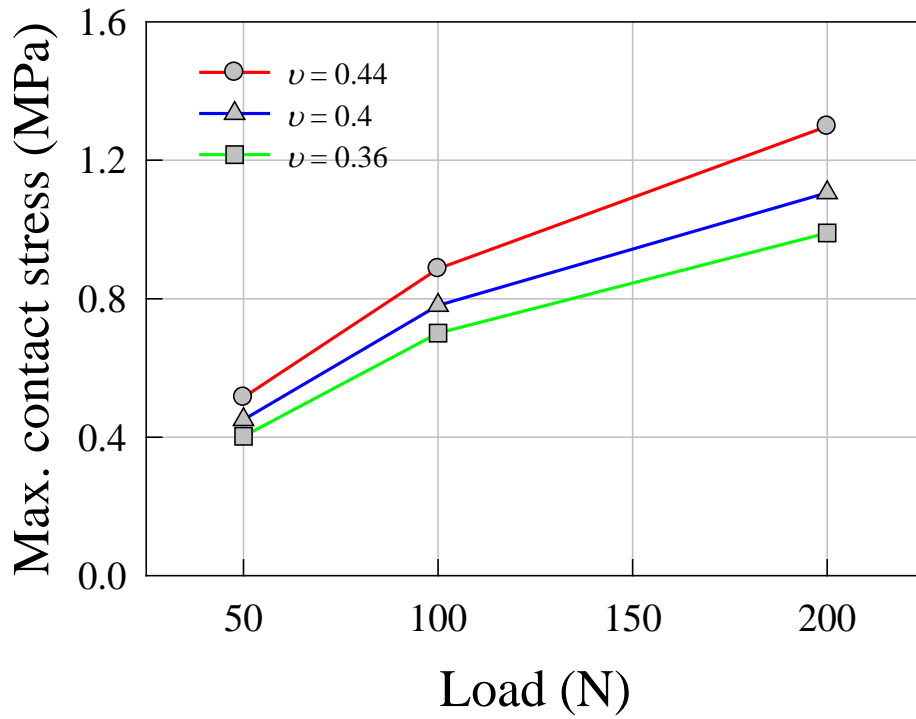


(b)

Figure 27. Average pressure with different Young's modulus in (a) humeroradial and (b) radioulnar joints

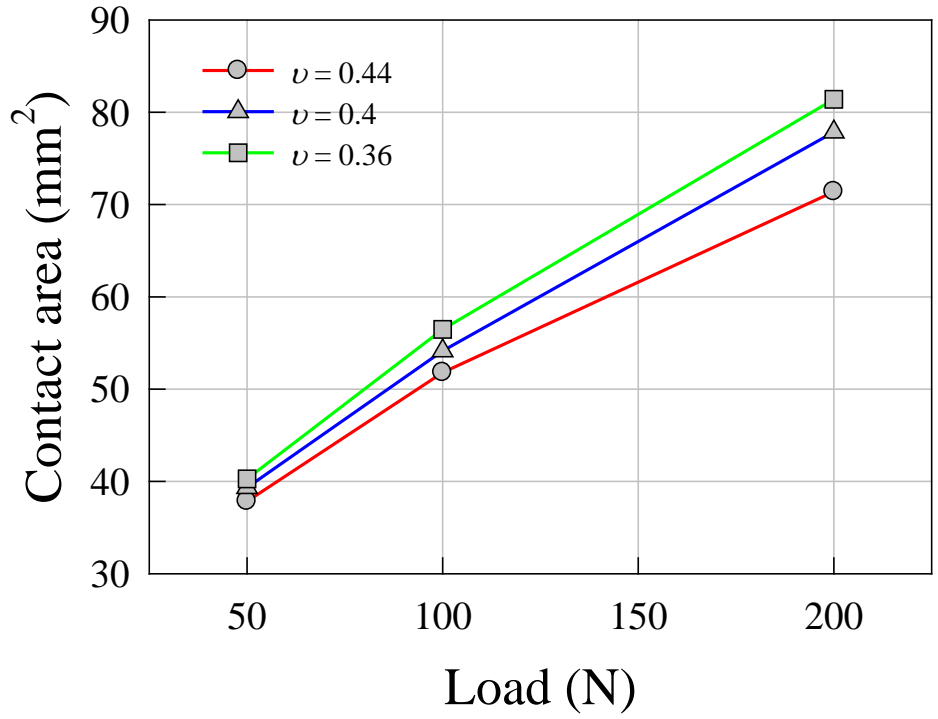


(a)

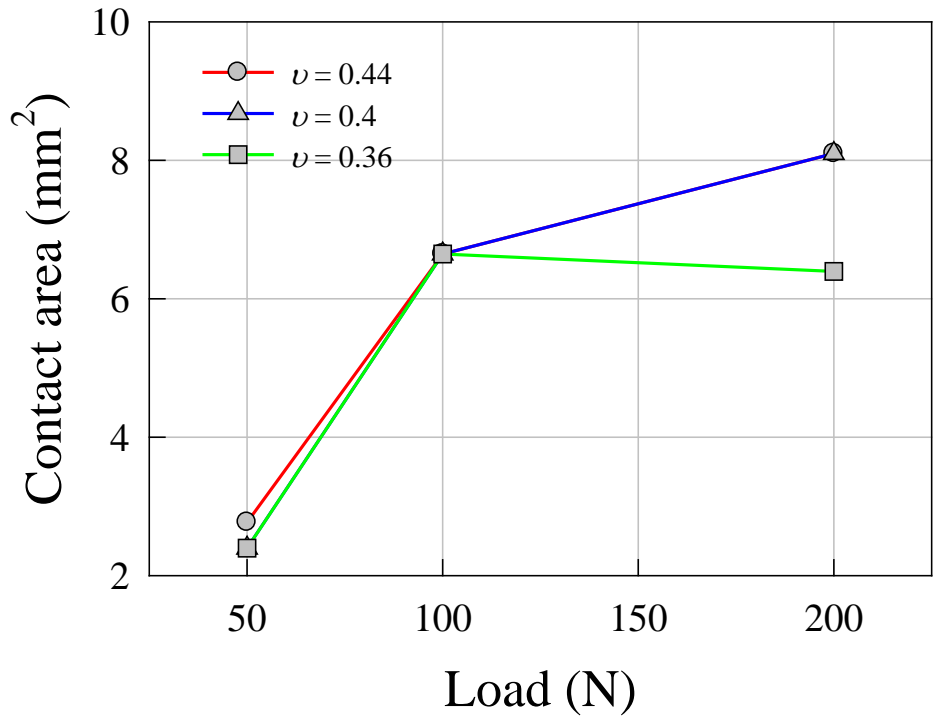


(b)

Figure 28. Maximum contact stress with different Poisson's ratio in (a) humeroradial and (b) radioulnar joints

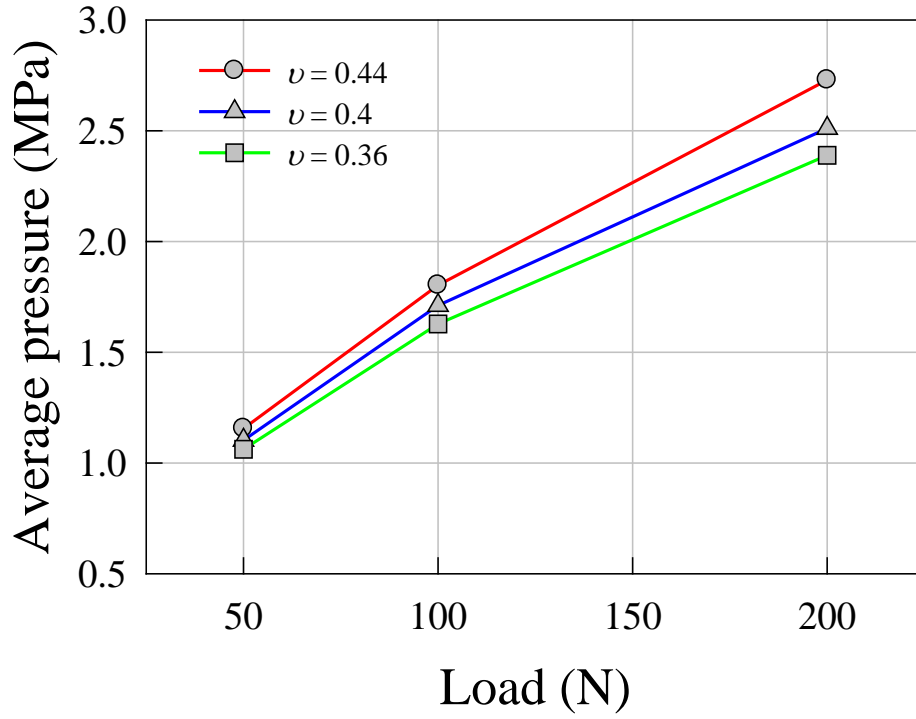


(a)

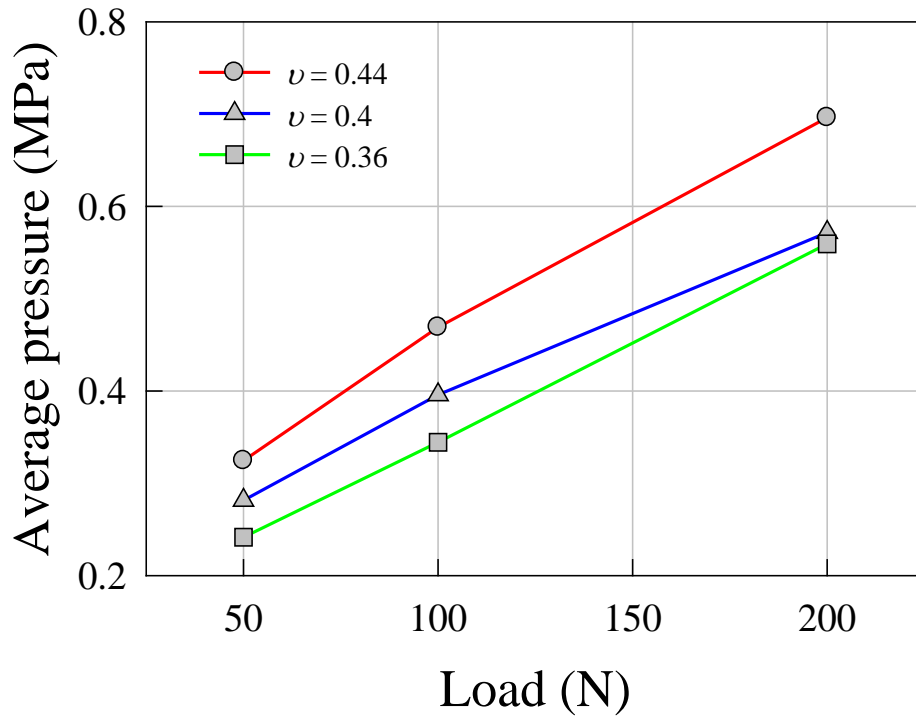


(b)

Figure 29. Contact area with different Poisson's ratio in (a) humeroradial and (b) radioulnar joints



(a)

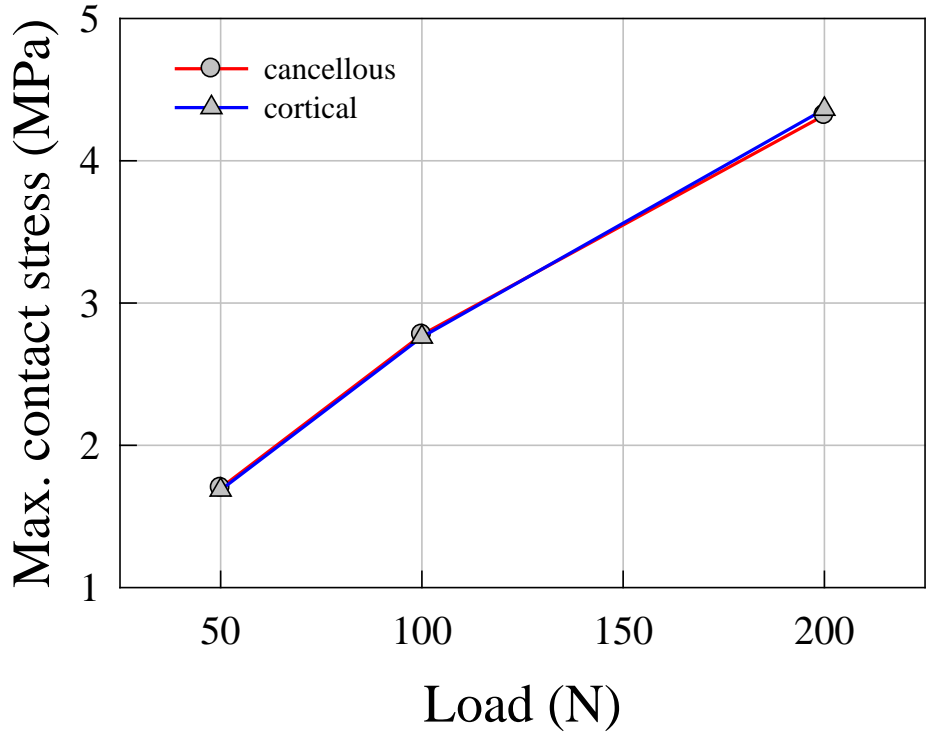


(b)

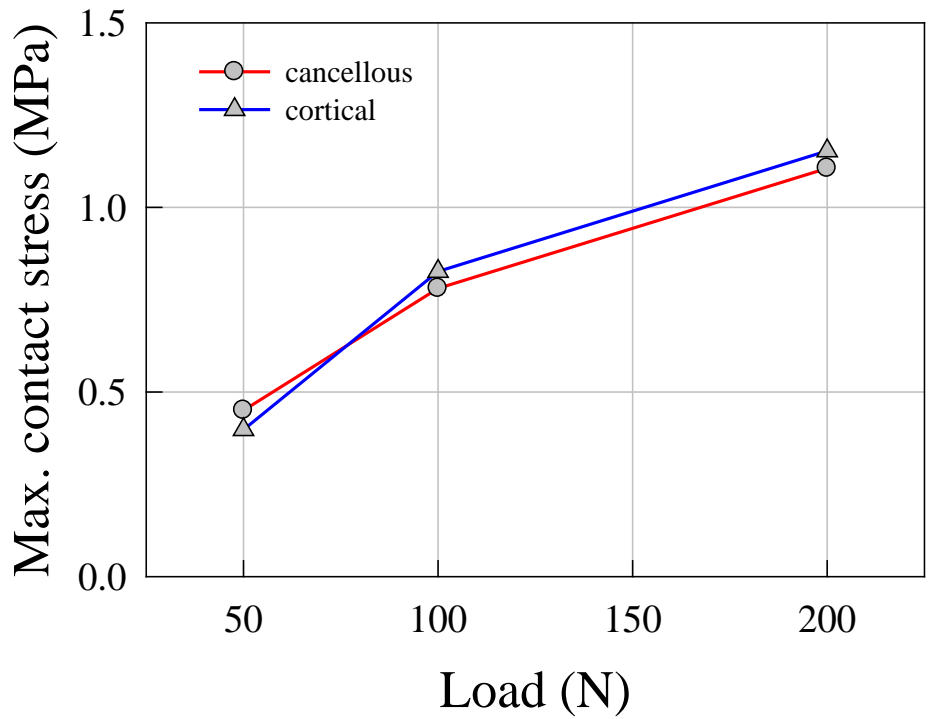
Figure 30. Average pressure with different Poisson's ratio in (a) humeroradial and (b) radioulnar joints

4.4.3 Bone material properties

All three bones were simply modeled as a linear isotropic material assuming that they were all cancellous bone. This assumption might sound unreasonable because a bone consists of cortical bone and cancellous bone. However, the focus here is the cartilage contact pressure. Additionally, the bones in the FE model is primarily subchondral bone, which is more like cancellous bone and much stiffer than cartilage. Thus, to show that this assumption could lead to acceptable results, two extremes (all bones were cancellous or cortical) were analyzed and compared. Material properties for cortical and cancellous bones were shown in Table 2. Figures 31, 32 and 33 show comparison of the maximum contact stress, contact area and average pressure between when the bones were modeled as whole cortical bone and whole cancellous bone. The difference in maximum contact stress, contact area, and average pressure for the humeroradial joint was relatively larger than that for the radioulnar joint due to the direction of the applied load which was perpendicular to the humeroradial contact surface and parallel to the radioulnar contact surface. The maximum contact stresses for both whole cancellous and whole cortical bone in humeroradial joint were almost identical for all three load cases. The difference in contact area and average pressure between whole cancellous and whole cortical bone in humeroradial joint was within 5%. Contact area for whole cancellous bone was slightly larger and average pressure was slightly lower than those for whole cortical bone. Therefore, considering that the maximum contact stress from a combination of cortical and cancellous bone would be in between whole cortical bone and whole cancellous bone cases, it is reasonable that three bones in this FE elbow model can be assumed to be whole cortical or whole cancellous even though the differences in the maximum contact stress, contact area and average pressure were somewhat greater in the radioulnar joint than the humeroradial joint.

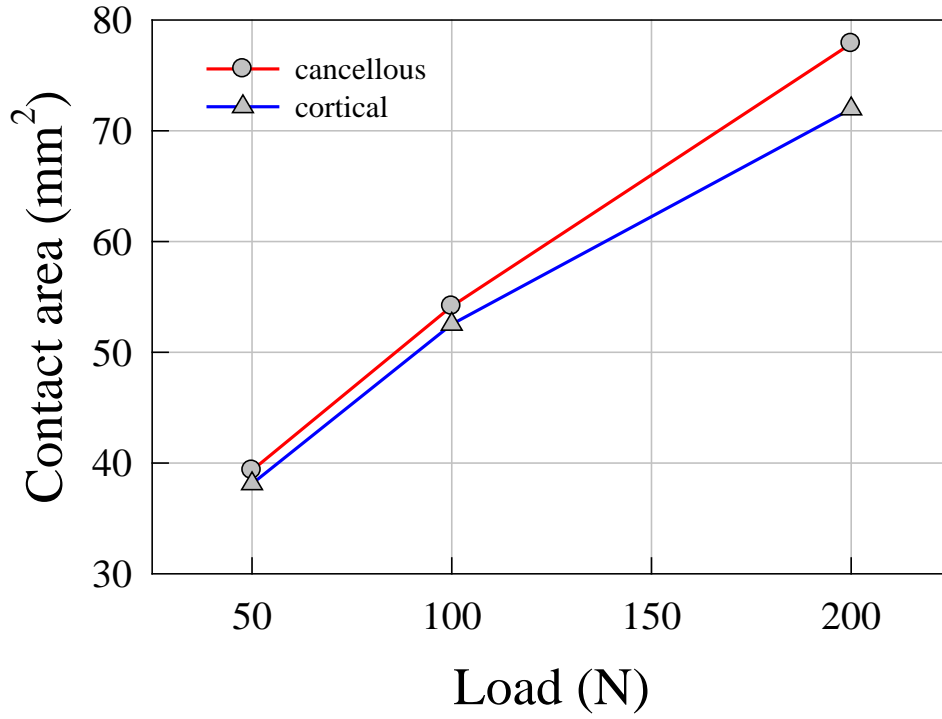


(a)

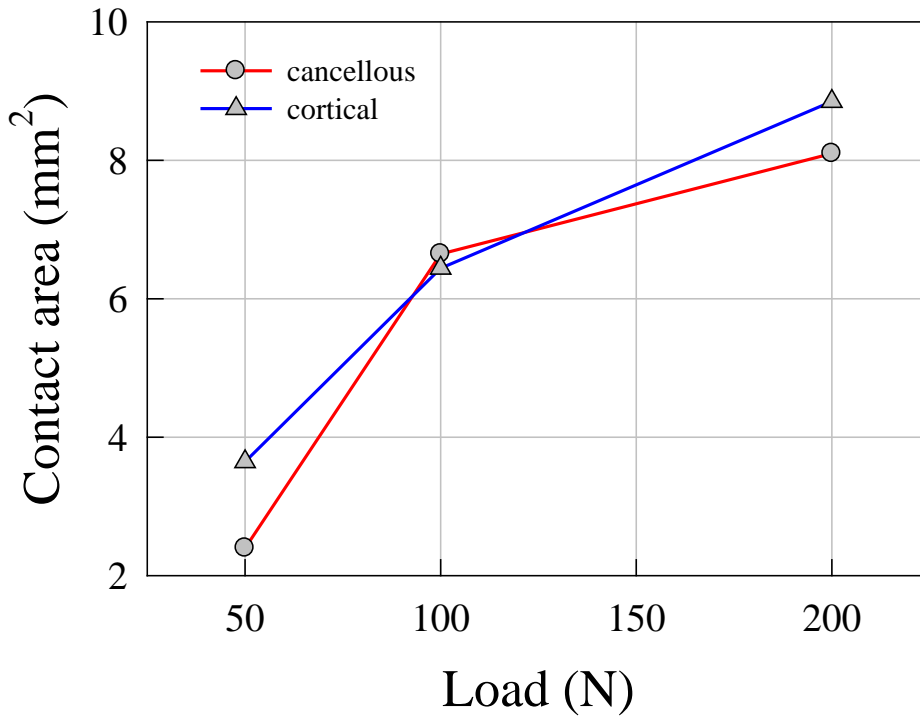


(b)

Figure 31. Max. contact stress with different bone material property in (a) humeroradial and (b) radioulnar joints

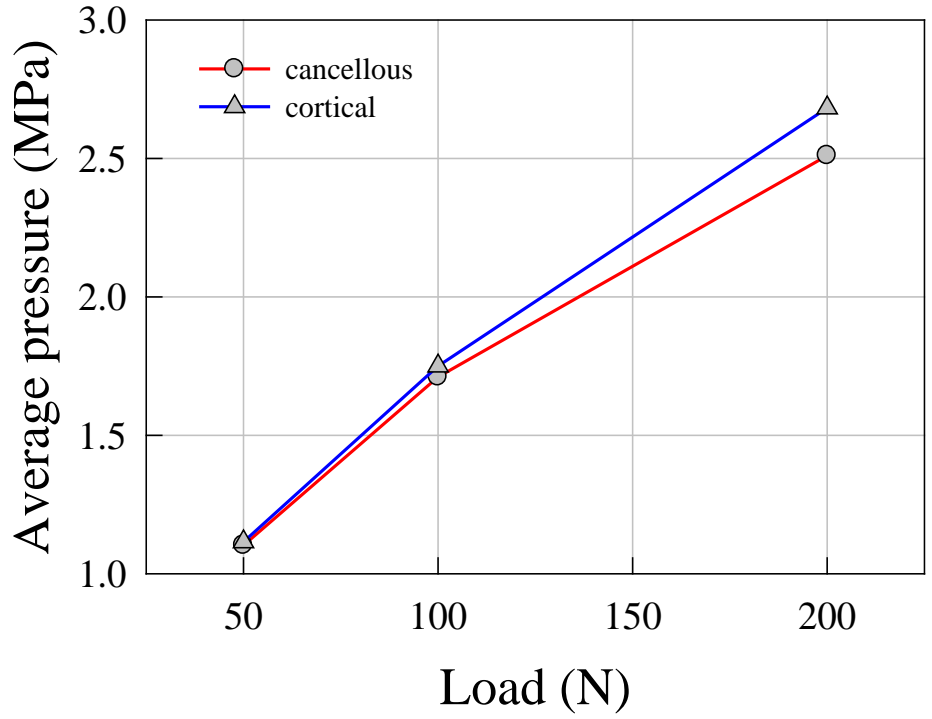


(a)

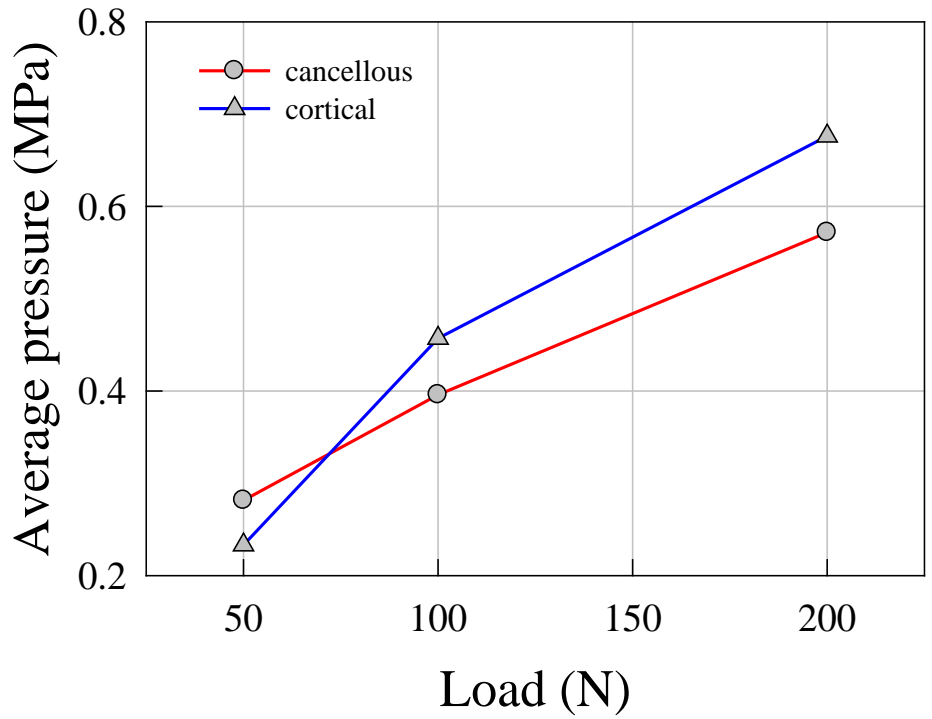


(b)

Figure 32. Contact area with different bone material property in (a) humeroradial and (b) radioulnar joints



(a)

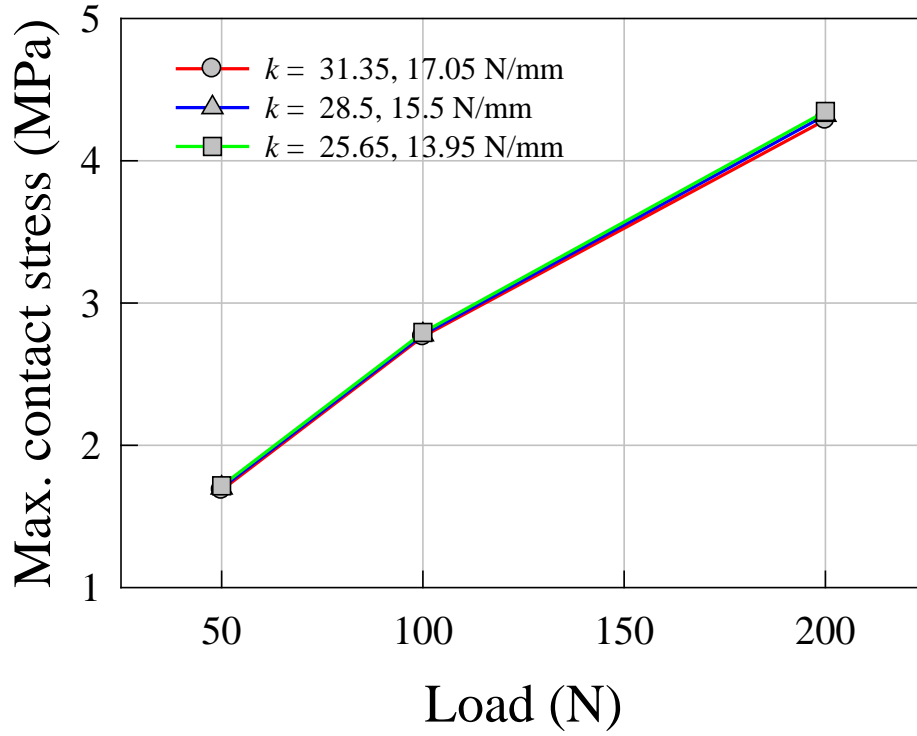


(b)

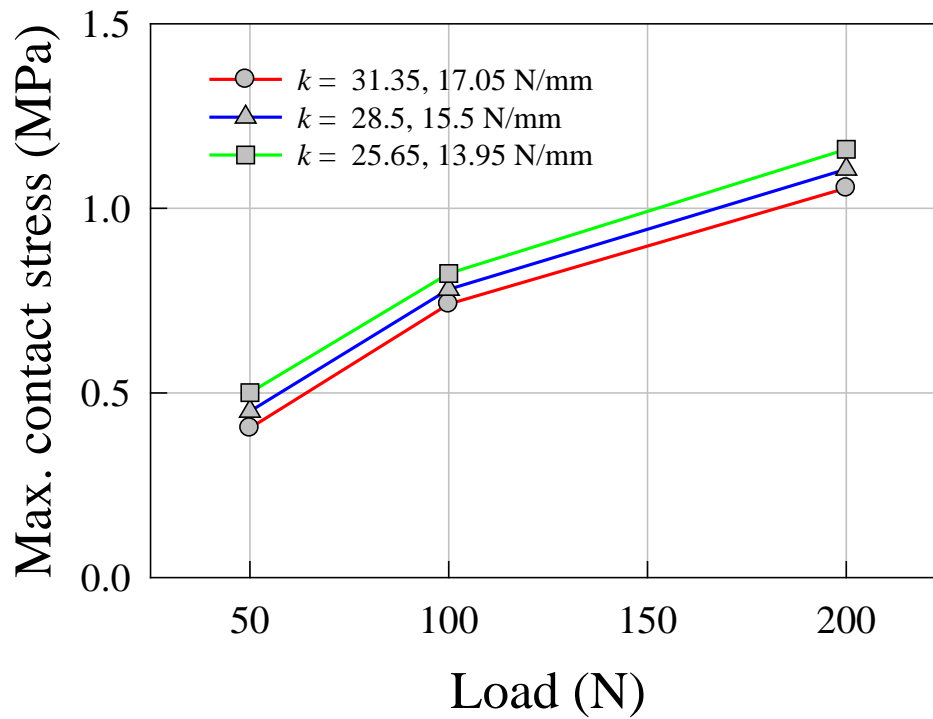
Figure 33. Average pressure with different bone material property in (a) humeroradial and (b) radioulnar joints

4.4.4 Ligament stiffness

The annular and lateral collateral ligaments in the FE model were modeled as linear spring elements characterized only by the spring stiffness. These elements held the three bones together and prevented independent rigid body motion of the radius. To examine the effect of the spring stiffness on FE results, 10% stiffer and 10% less stiff spring elements were analyzed. The maximum contact stress, contact area and average pressure with three different ligament stiffnesses are plotted in Figures 34, 35 and 36 respectively. Overall ligament stiffness had no significant effect on any of the maximum contact stress, contact area or average pressure for both the humeroradial and radioulnar joints. Average differences of the maximum contact stress, contact area and average pressure in the humeroradial and radioulnar joints were approximately 1 and 8% respectively.

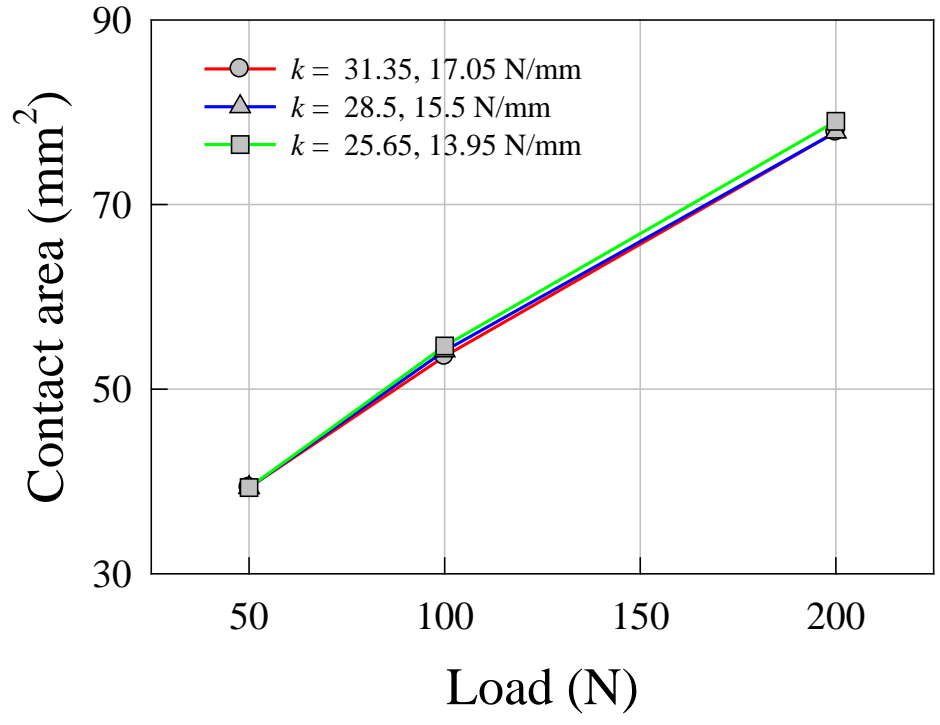


(a)

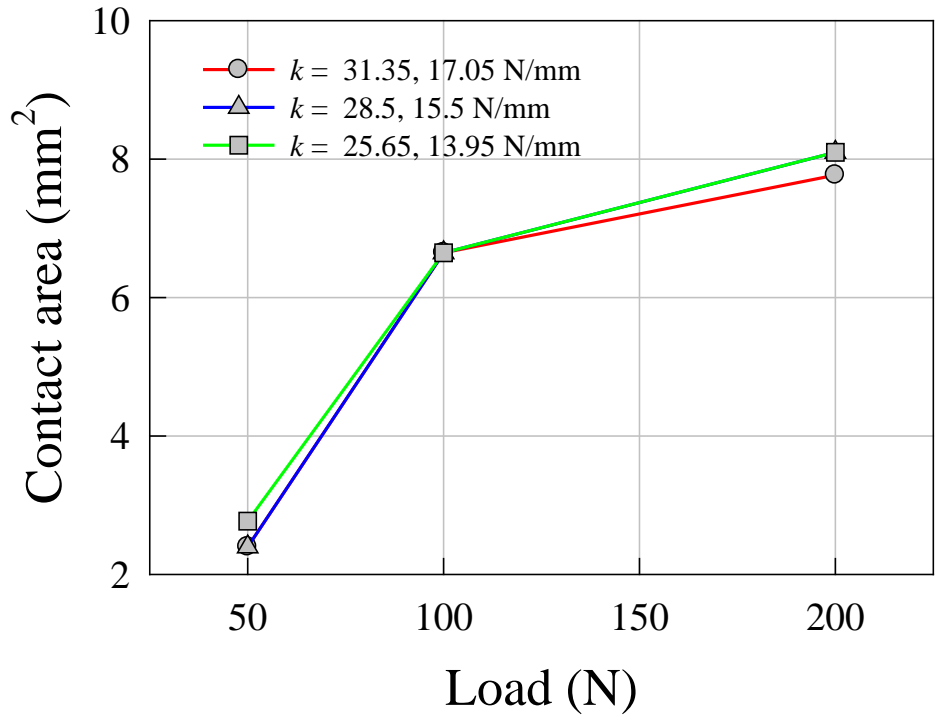


(b)

Figure 34. Maximum contact stress with different ligament stiffness in (a) humeroradial and (b) radioulnar joints

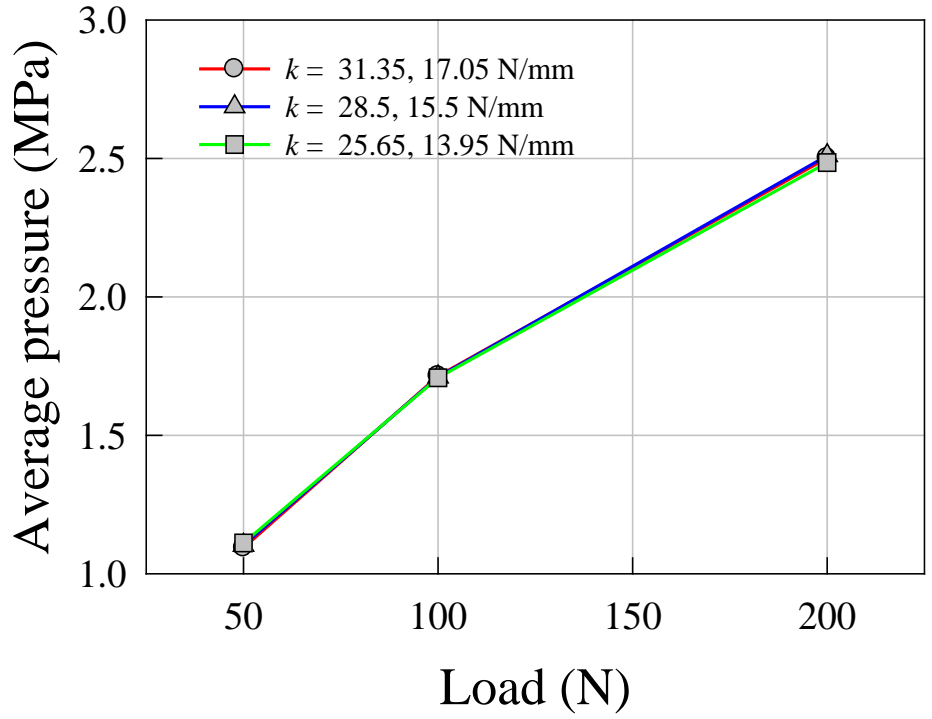


(a)

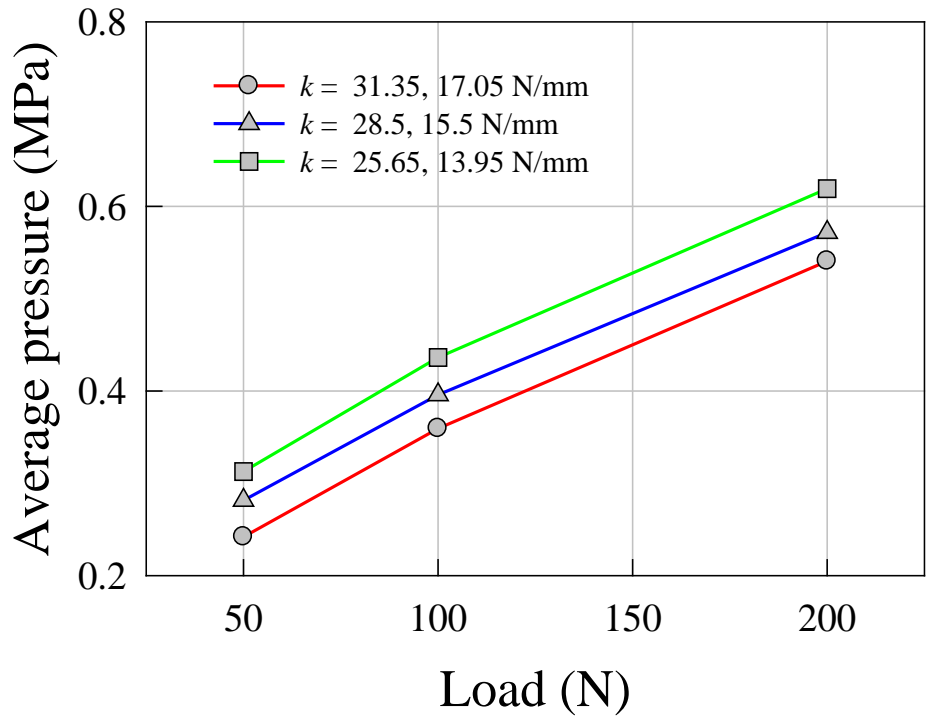


(b)

Figure 35. Contact area with different ligament stiffness in (a) humeroradial and (b) radioulnar joints



(a)



(b)

Figure 36. Average pressure with different ligament stiffness in (a) humeroradial and (b) radioulnar joints

5.0 RADIAL HEAD IMPLANT FE ANALYSIS

There has been research on the contact patterns of radiocapitellar joint in the intact elbow [127, 128]. However, there have been only very few studies about the effect of the radial head arthroplasty on the biomechanics of the elbow joint.

Surgeons often choose a specific implant by familiarity and experience. There is little information about comparison between basic two types of implants (monoblock and bipolar). In order to quantitatively compare those radial head implants, an FE model for each type was created based on the native FE model. For the monoblock type, the rHead (Small Bone Innovations, New York, NY) radial head prosthesis was selected and the Katalyst (Integra LifeScience, Plainsboro, NJ) implant was chosen for the bipolar type. The optimal size for each implant was chosen based on the circumference of the native radial head. The circumference of the native radial head was approximately 62.50 mm. The circumference of best matched implant was approximately 65.97 mm (diameter was 21 mm) for both types. The basic geometry (radius, width, and height) of the implants was obtained using an optical comparator and the radius of the curvature of the top surface of each implant was measured by coordinate measuring machine. One of the most difficult parts in making FE implant model was to establish the proper position of the implant. Additionally, for contact stress analysis in two articulations slight contact (penetration) between the implant and two bones (humerus and ulna) was required. Thus, the center of the curvature on the capitellum was calculated using sphere fitting and the implant was positioned so that its center was aligned with the center of the capitellum in the plane perpendicular to the longitudinal axis of the radius. For the slight initial contact between ulna and the implant, the ulna was moved toward the implant until the required condition for contact analysis was satisfied. As a parametric study to examine

the effect of the implant size on the contact stress and contact area, 10% bigger size and 10% smaller size of implants were included in the analysis.

5.1 MONOBLOCK IMPLANT MODEL

The rHead implant was chosen to represent the monoblock implant and only the implant head was included in the FE model (i.e., the stem was not included). The monoblock (rHead) implant was drawn in SolidWorks according to the measured dimensions, converted to an IGES file and exported into ANSYS. The intact radial head in the constructed FE model was then replaced with the implant, using the same alignment as the native head. The implant was meshed with 3-D tetrahedral elements and linear elastic material properties of cobalt-chrome alloy were assigned. The elastic modulus was 220 GPa and Poisson's ratio was 0.3. [129]. The front and side view of the constructed FE monoblock implant model was shown in Figure 37. The same boundary and loading conditions were applied to the implant as the native radial head. The maximum contact stress, contact area and average pressure with different implant sizes are shown in Figure 38, 39 and 40 respectively. There was no significant difference caused by implant size in the maximum contact stress, contact area and average pressure. The maximum contact stress and average pressure were larger and contact area was smaller with a larger implant due to larger radius of curvature leading to reduced contact surface between the implant and the capitellum. Figure 41 shows contact stress distribution on the capitellum with 50, 100 and 200 N of applied loads.

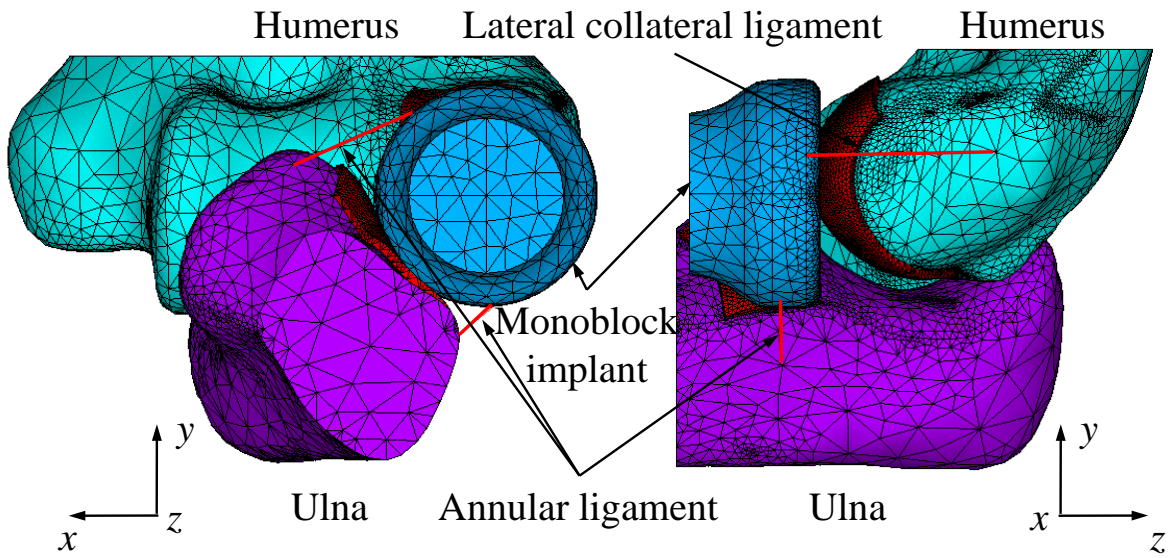


Figure 37. Front (left) and side view (right) of monoblock implant FE model mesh

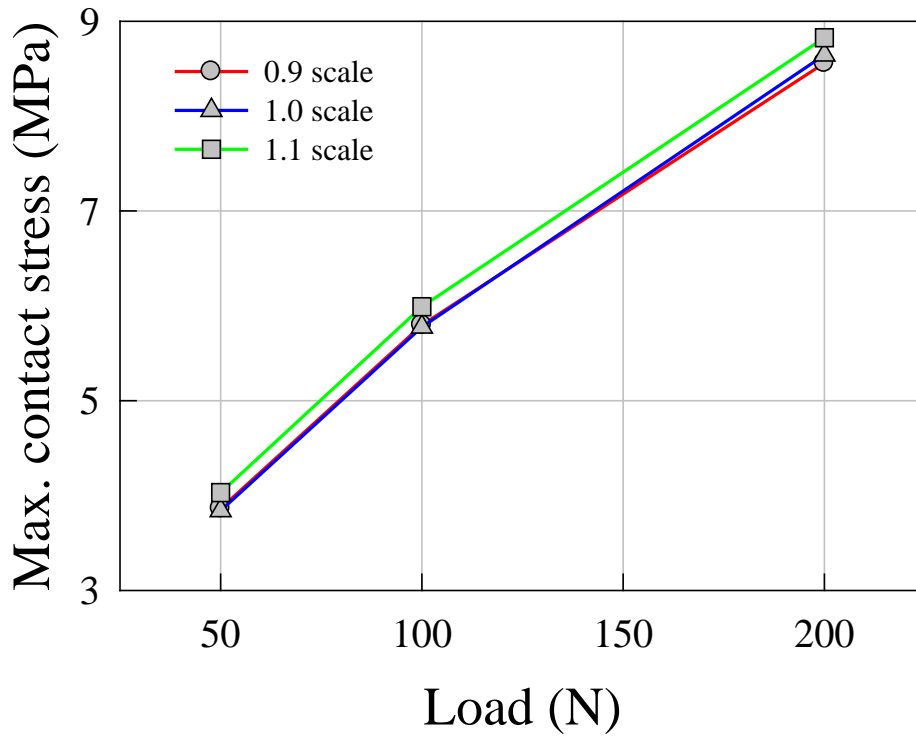


Figure 38. Maximum contact stress in humeroradial joint with different size of monoblock implant

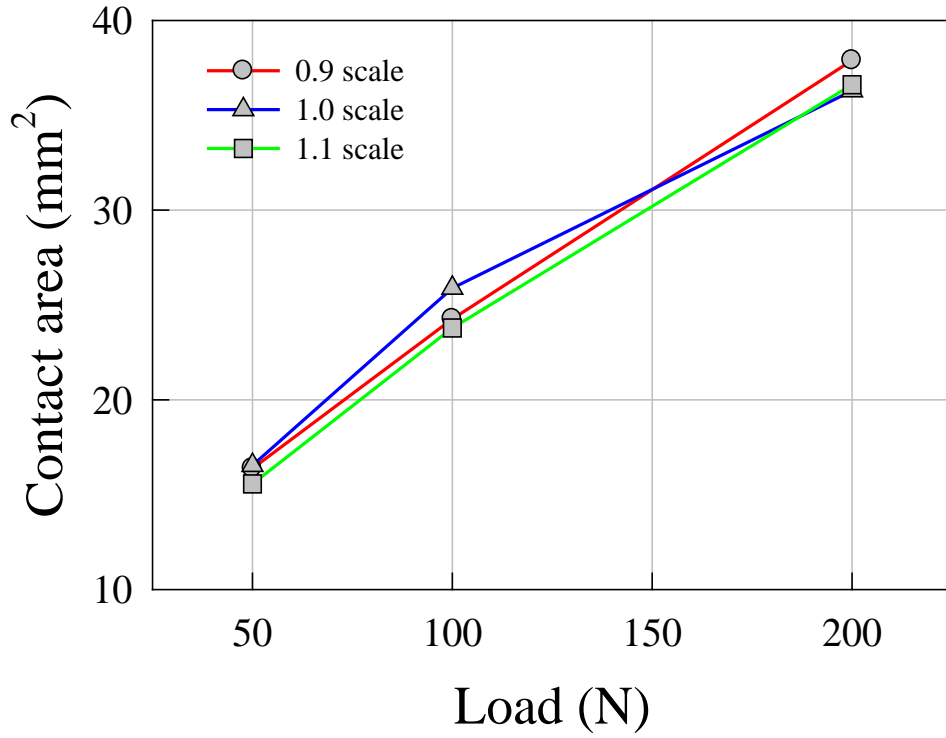


Figure 39. Contact area in humeroradial joint with different size of monoblock implant

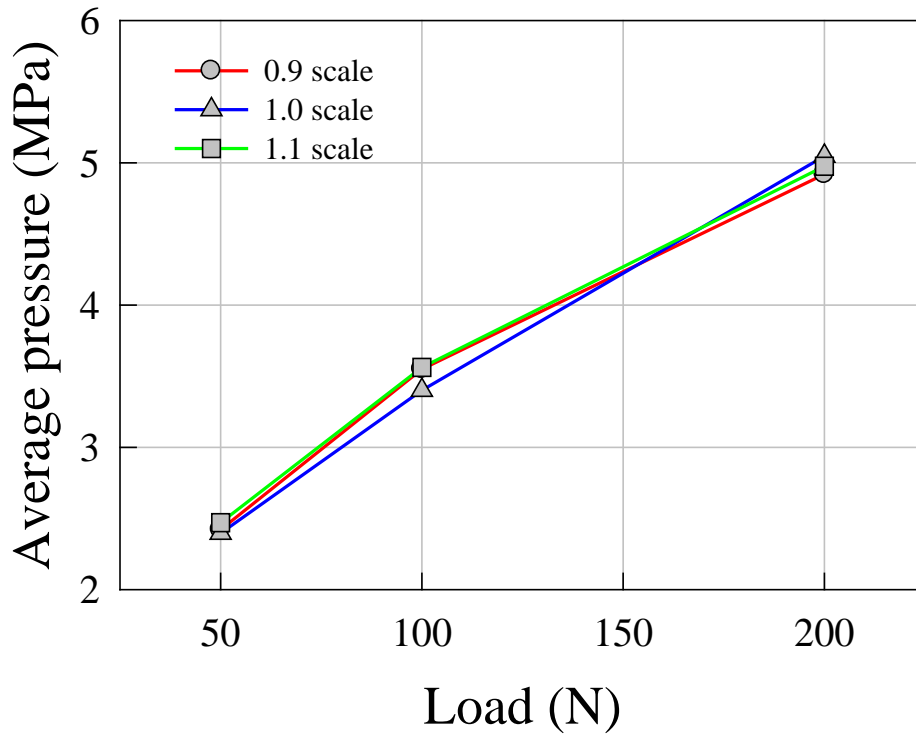


Figure 40. Average pressure in humeroradial joint with different size of monoblock implant

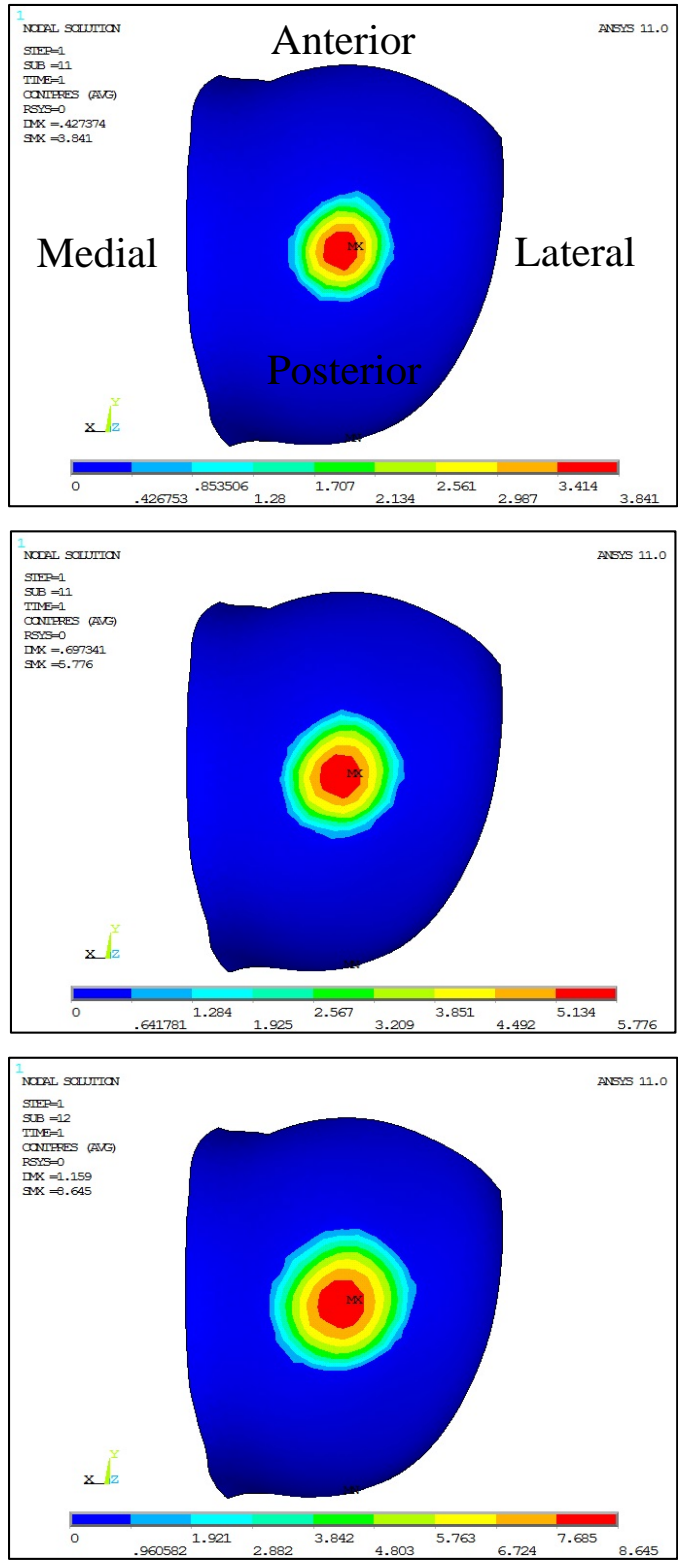


Figure 41. Contact stress distribution of capitulum with rHead implant under 50N (top), 100N (middle), and 200N (bottom)

5.2 BIPOLAR IMPLANT MODEL

The Katalyst implant model was constructed with the same procedure used for the monoblock implant model. Like the monoblock implant only the head of the Katalyst implant was included and modeled as a linear elastic material. Material properties of Cobalt-Chrome alloy were assigned. For the boundary conditions of the implant, the center node of the distal surface of the implant was constrained in medial-lateral and anterior-posterior directions so that the implant was free to rotate medial-laterally and anterior-posteriorly. The front and side view of the bipolar implant FE model were shown in Figure 42. The maximum contact stress, contact area and average pressure with three different implant sizes are shown in Figures 43, 44 and 45 respectively. The maximum contact stress and average pressure were larger and contact areas was smaller with larger implant due to the same reason as monoblock. However, the differences of the maximum contact stress, contact area, and average pressure were relatively larger than those for the monoblock. The maximum contact stress increased by approximately 6% as the implant size increased by 10%. Contact stress distribution with three different applied loads were shown in Figure 46.

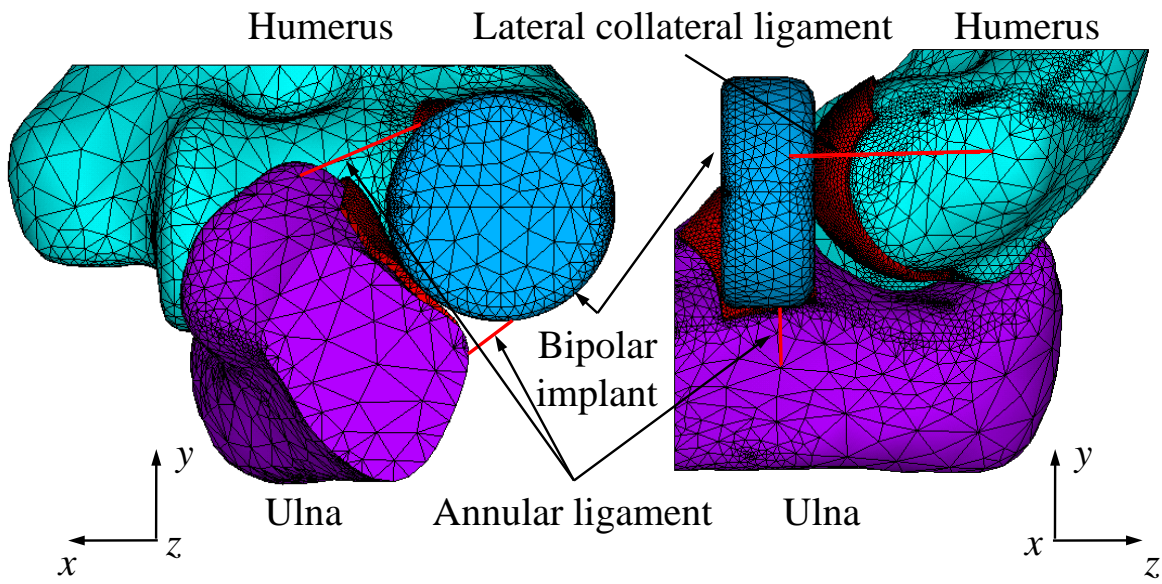


Figure 42. Front (left) and side view (right) of the bipolar implant FE model mesh

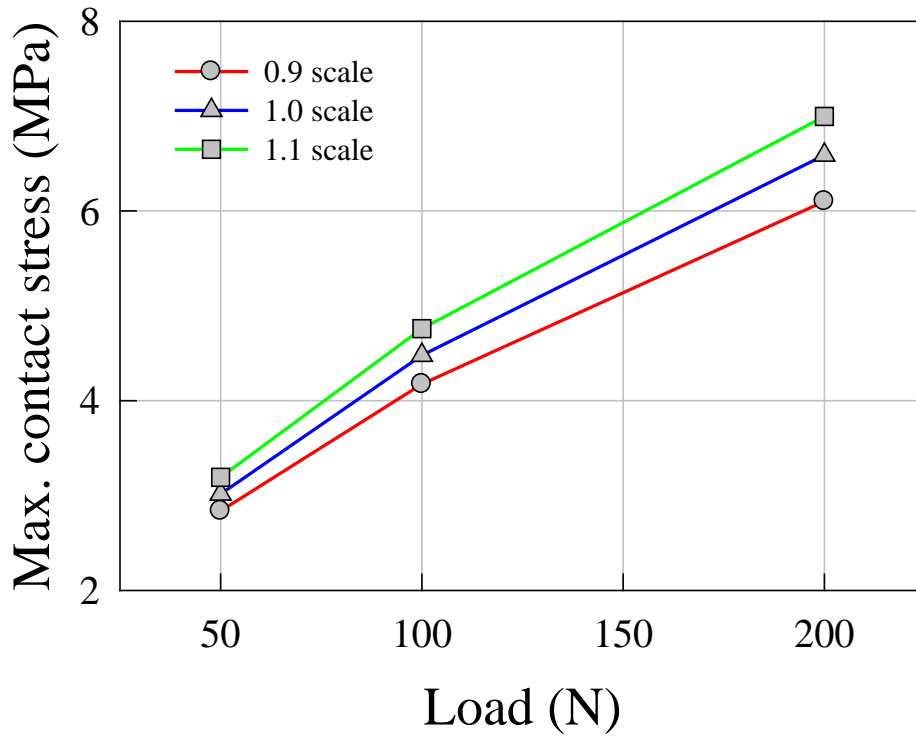


Figure 43. Maximum contact stress in humeroradial joint with different size of bipolar implant

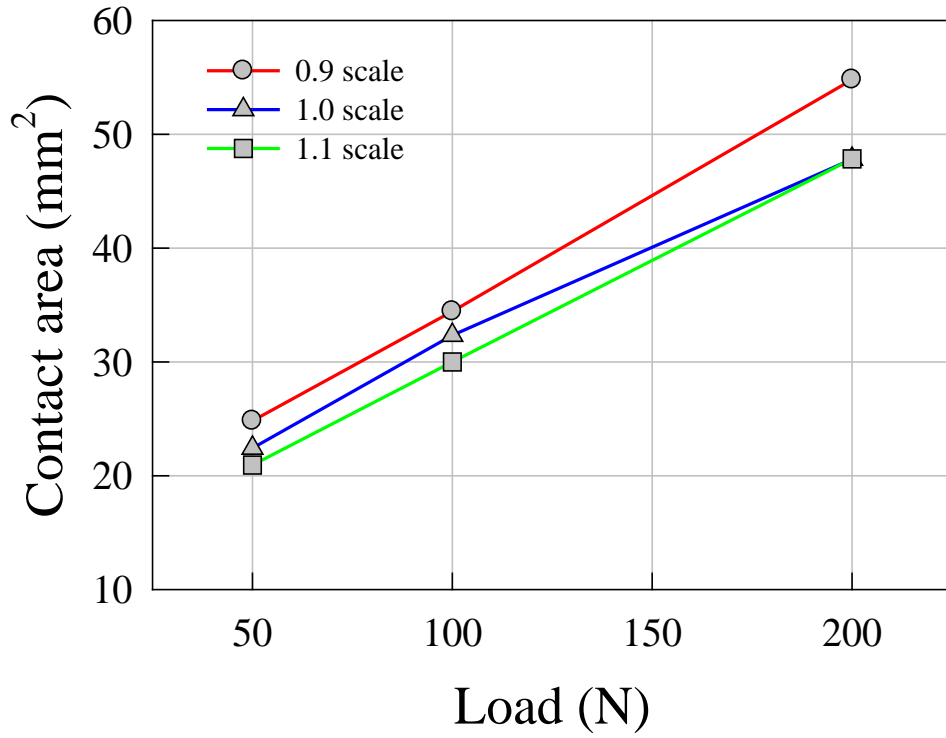


Figure 44. Contact area in humeroradial joint with different size of bipolar implant

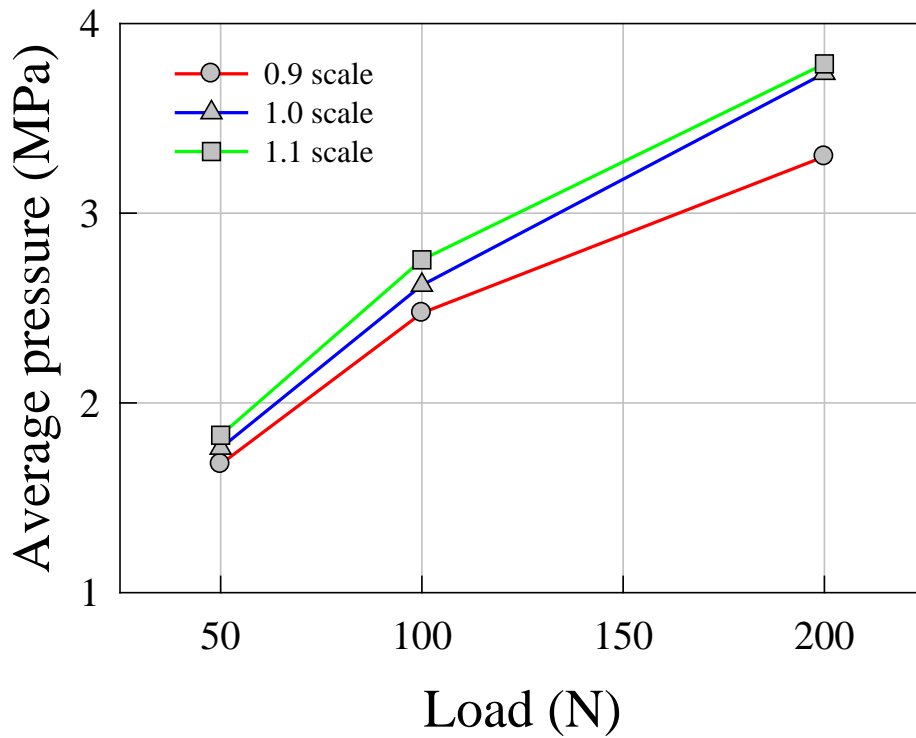


Figure 45. Average pressure in humeroradial joint with different size of bipolar implant

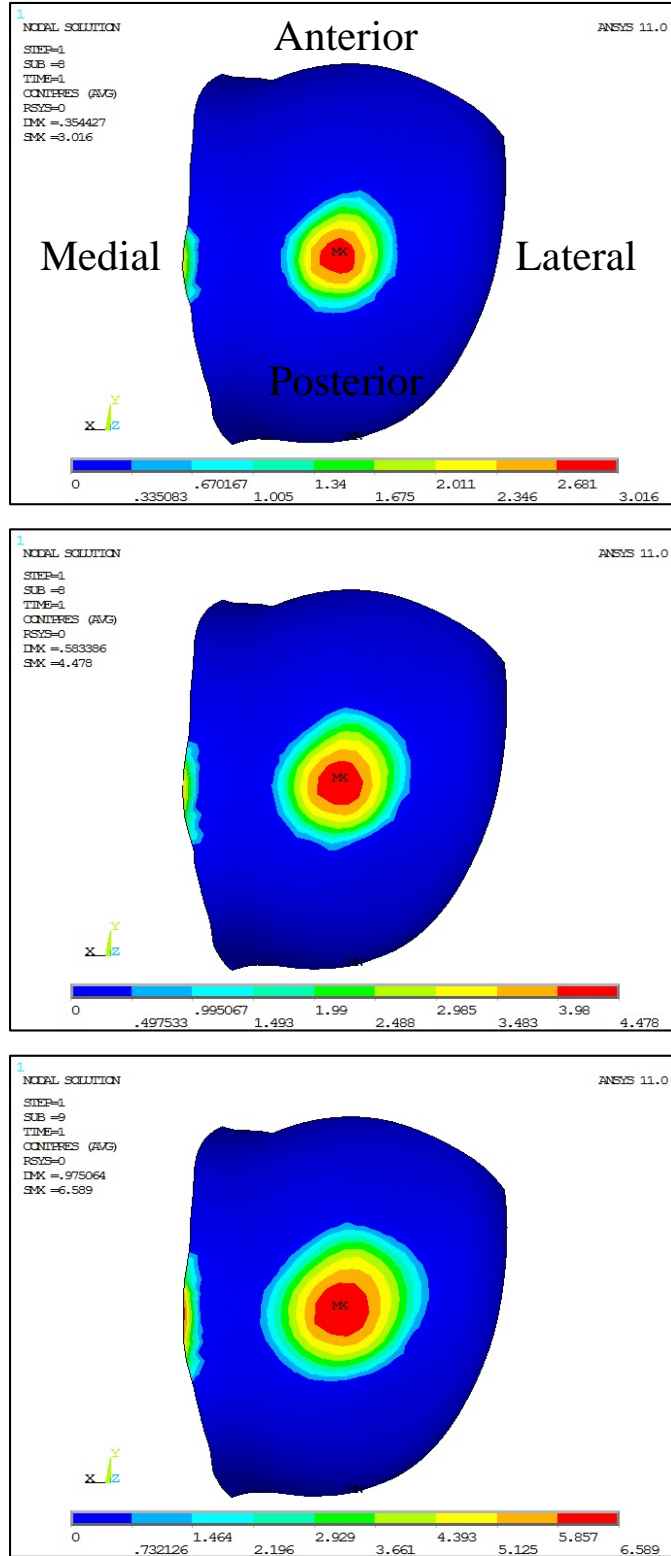


Figure 46. Contact stress distribution of capellum with Katalyst implant under 50N (top), 100N (middle), and

200N (bottom)

6.0 VALIDATION OF THE FE MODEL

The strongest model results are those that show agreement between model predications and physical measurements. Thus, a constructed FE model should be validated with physical experiments. Otherwise, the results from the model might not be meaningful. Four cadaveric elbows were tested to validate the FE models for the native and radial head implanted elbows by comparing the pressure, contact area and average pressure measured using Fuji pressure sensitive film with those calculated from the FE model.

6.1 EXPERIMENTAL SETTING

Due to the limited range of pressure that each Fuji film grade can detect, two different grades (super low and low) of Fuji film were prepared before the test to measure the maximum contact pressure and contact area. Super low film was used for calculating the contact area and low grade was used for the maximum contact stress when super low was saturated (reached the maximum pressure that it can measure). For each film grade, A and C films were cut into 20.637 mm (diameter) circles. Four cuts were made from the outside towards the center of the film, not completely cut the film into four pieces but left a little disk in the center of the film, to minimize artifacts from folding and buckling of the film under loading, which was one of the most difficult parts in dealing with pressure sensitive film. Then, A and C films were put together on a thin plastic wrap with active coating sides of both films contacting each other. A thin clear tape was applied on top of A and C film pairs to hold them together and prevent the permeation of the

moisture. A sample of super low Fuji film packet is shown in Figure 47. The thickness of the packet is 0.2 mm.



Figure 47. Fuji film packet (super low)

Four fresh frozen cadaveric elbows (3 male and 1 female, 2 right and 2 left) were thawed in the room temperature for 15 hours before the experiment. Average age of the specimens was 53 years old. All the soft tissues including skin, muscle and tendon were carefully dissected except the joint capsule, interosseous membrane and ligamentous structures in the elbow joint. Two 2 cm incisions near the humeroradial joint, one each on the anterior and the posterior of the joint capsule, were made for the insertion of the Fuji film packet. The ulna was excised at approximately 5 cm from the distal radioulnar joint so that the load was applied only to the radius. The proximal humerus and distal radius of the elbow were potted in PVC pipes using styrene-acrylic polymer resin, which is used for auto body repair, and then mounted in the MTS Bionix 858 (Eden Prairie, MN) for application of load. Custom made fixtures were used for both humerus and radius. The experimental set-up is shown in Figure. 48. Super low and low Fuji film packets were inserted one by one through the incision on the anterior side of the joint and pulled out from the posterior

incision before the load was applied. The loads of 50, 100, and 200 N were applied at a rate of 10 N/sec to the radius under load control. When the load reached a specified peak value, that load level was held for 1 minute for obtaining a good stain and then, specimen was unloaded at the same rate as it was loaded. For each load case, the maximum stress and contact area were measured three times.

After all the measurements for native elbow were finished, the annular ligament was cut and the native radial head was exposed, resected and replaced with one of two different types of radial head implants. Appropriate size of the implant was selected based on size of the resected radial head. Then, either the monoblock or bipolar implant was inserted and the annular ligament was reconstructed with suture. For the first two elbows, the bipolar implant was tested after monoblock implant was tested. Testing order was reversed for the third and the fourth elbows.

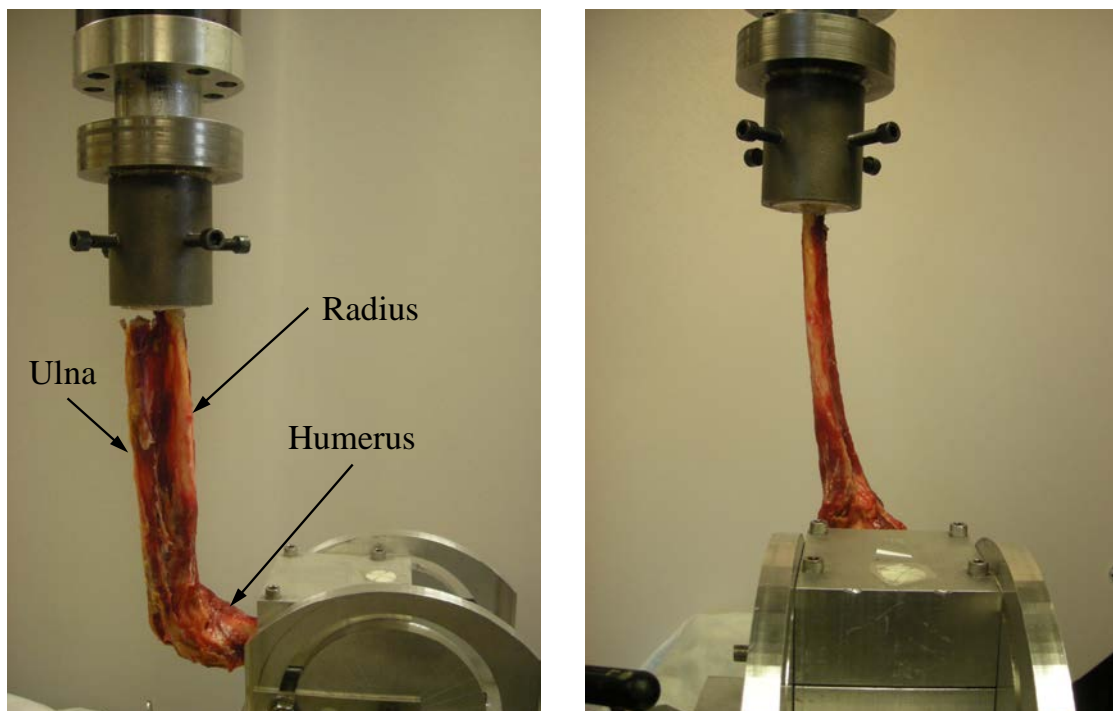


Figure 48. Experimental setup: cadaveric elbow mounted into MTS Bionix 858, side view (left) and front view (right).

6.2 FUJI FILM ANALYSIS

As soon as the load was removed, Fuji film packets were carefully removed from the cadaveric elbow, scanned by a flatbed scanner, HP Scanjet 5590, at a spatial resolution of 600 dpi and saved as 8 bit grayscale TIFF images. Scanned Fuji film images (superlow) are shown in Figure 49. It can be observed that stains were getting bigger and darker for all three cases as applied load increased. The maximum pressure and contact area from scanned images were calculated using custom MATLAB image processing program [130]. The scanned 8 bit grayscale images were loaded into the program and converted to pressure images using a fifth order polynomial fit. Noise was filtered after conversion under the assumption that it caused variations in the individual pixel value that was not correlated with the values of adjacent pixels. The filter replaced each individual pixel value with the average value of the pixels in the surrounding 25 x 25 pixel area.

The stain intensity of every pixel in the scanned images was converted into numbers from 0 to 256 and then finally into the pressure by comparing the numbers with the calibration data computed in the laboratory. A different converter was used for different film grade. Averaged maximum contact stress and the contact area are listed in Table 4. Stains from super low film were saturated except for native and bipolar cases under 50 N but those from low grade were not, which means the pressures from low grade did not reach the maximum limit of the film. For those two cases whose stains for super low were not saturated maximum contact stress and contact area were obtained from super low film and for all the other cases maximum contact stress and contact area were calculated from low and super low respectively. The maximum contact stresses for monoblock were almost twice as high as those for native elbow and maximum contact stress for bipolar was in between native and monoblock. Contact areas for bipolar under 50 and 100 N were slightly lower than those for native case but under 200 N there was approximately 30 mm²

difference between native and bipolar, which is approximately 36% of contact area for native elbow under 200 N.

A t-test for the maximum contact stress and contact area was conducted between native and bipolar, native and monoblock, and bipolar and monoblock. Statistical significance ($p < 0.05$) in the maximum contact stress was found in all the cases except for bipolar and monoblock under 100 N. For contact area, statistical significance was found except for native and bipolar under 50 and 100N, and bipolar and monoblock under 200N.

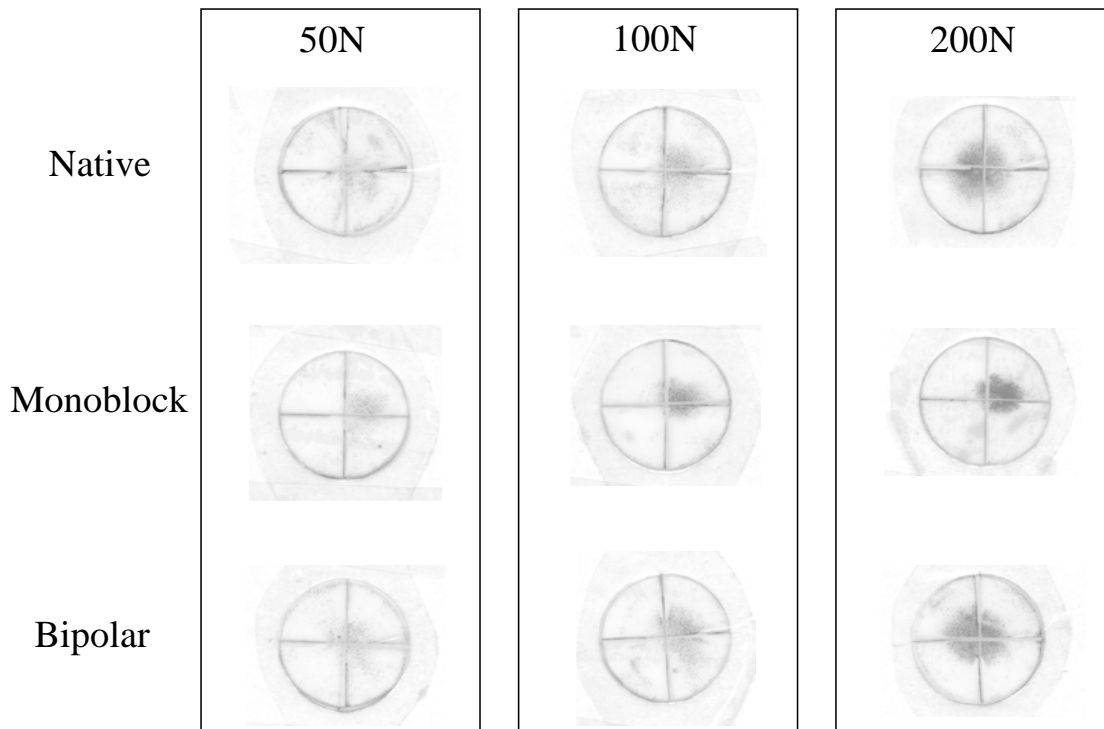


Figure 49. Scanned image of Fuji film (super low)

Table 4. Maximum contact stress and contact area calculated from Fuji film

Load (N)		Max. contact stress (MPa)	SD	Contact area (mm ²)	SD
50	Native	1.34	0.35	29.73	5.57
	Monoblock	3.74	0.69	21.07	3.60
	Bipolar	2.18	0.72	27.81	4.90
100	Native	2.48	0.47	46.33	8.62
	Monoblock	5.18	1.14	29.68	2.05
	Bipolar	3.98	0.36	39.37	8.78
200	Native	3.84	0.36	83.34	12.09
	Monoblock	7.62	0.56	42.30	4.12
	Bipolar	5.90	1.28	53.46	6.59

6.3 COMPARISON BETWEEN FE AND FUJI FILM

The maximum contact stresses, contact areas and average pressures from the FE analysis and Fuji film analysis are compared in Figures 50, 51 and 52 respectively. Average pressures from Fuji film were calculated by the approximation of combining average pressures of super low and low films. The FE prediction and the measurement using Fuji film for the maximum contact stress and contact area are in general agreement. FE predictions for maximum contact stress and average pressure were higher than those from Fuji analysis whereas FE predictions for contact area was lower compared to those from Fuji. Most predictions fell within 95% confidence intervals of the measurements and the trends of the model and the measurements were the same except in the contact area for the native case. For the contact area in the native case, the 50 and 100 N Fuji film measurements fell beneath the predicted model values, while all other comparisons in all other cases showed higher experimental measurements than model predictions. FE predictions were up to 16% higher in the maximum contact stress and lower in contact area than cadaveric testing. The monoblock pressures were always the highest and the areas, of course, commensurately the lowest. These differences in the maximum stresses and contact areas agreed with the differences in the radii of curvature of the contacting surfaces. The radius of curvature for the monoblock was approximately twice as large as that for the bipolar. The monoblock had higher stresses, smaller contact areas and the largest difference in the radii of curvature between the radial head and capitellum. The native case had the lowest stresses, the largest contact area and the smallest difference between the radii of curvature of the contacting surfaces. While the measurements and

the model predictions showed good overall agreement, the predictions did not all fall within the 95% confidence intervals of the measurements. Given that the trends were all in agreement, additional experimental measurements might produce overall agreement. The results concur with the experimental measurements by Liew et al. [105] who quantified contact areas of the native radial head and monoblock implant using dental impression material under 100 N of applied load and found a 68% reduction in contact joint area after radial head replacement. There was bigger discrepancy in average pressure between FE prediction and Fuji analysis than those in both maximum contact stress and contact area because the approximation of combining two different grades of Fuji film was not accurate and it was inevitable to get the artifacts of Fuji film from folding and bending especially with lower applied loads. Average pressure apparently involved more errors than the maximum stress and contact area due to artifacts of the film.

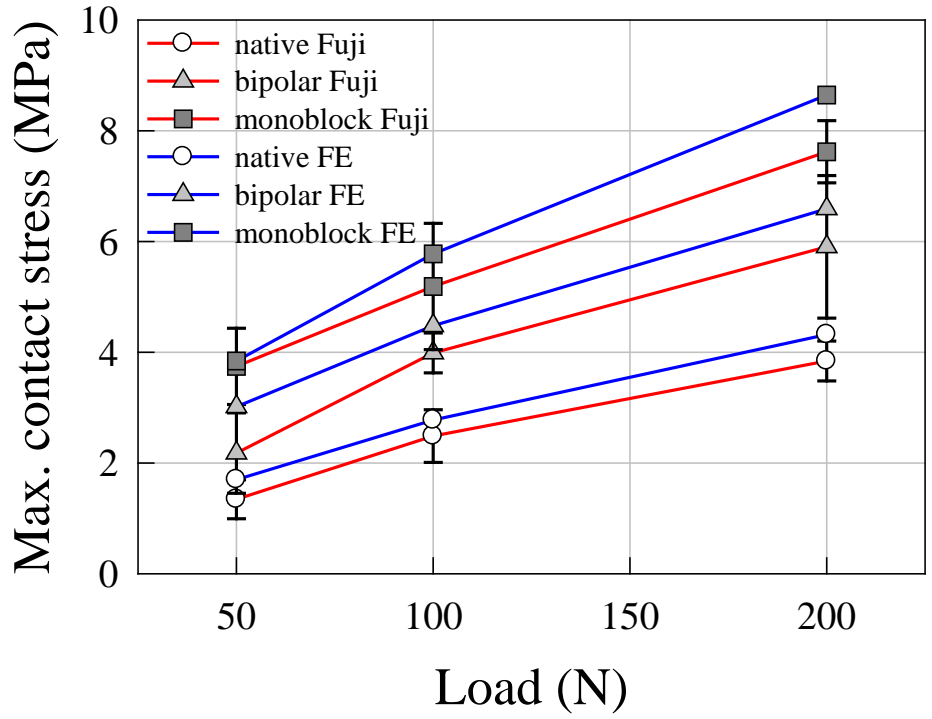


Figure 50. Maximum contact stress comparison

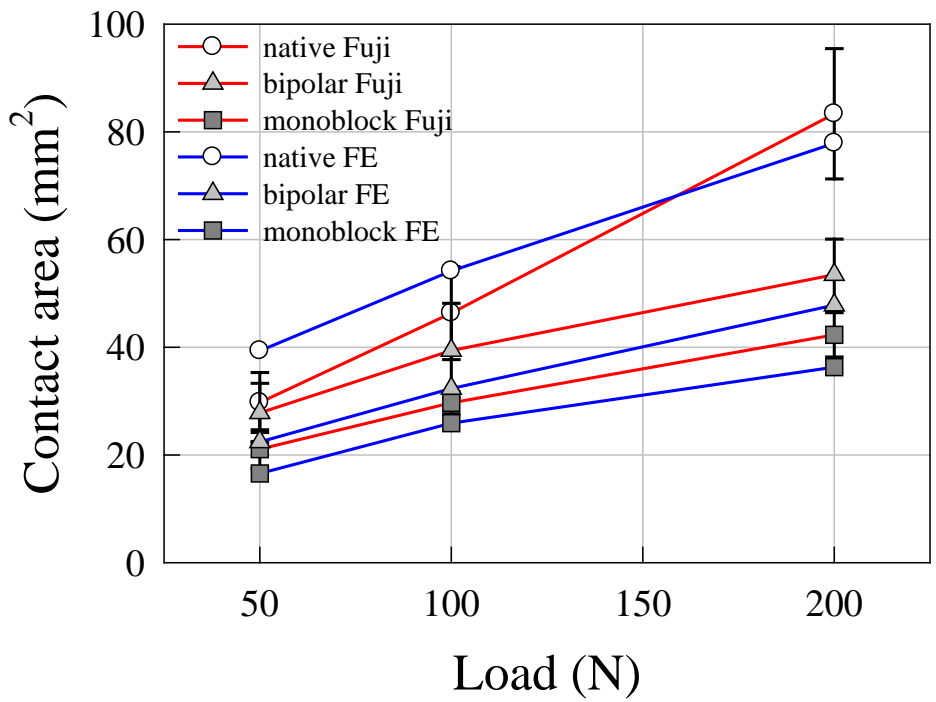


Figure 51. Contact area comparison

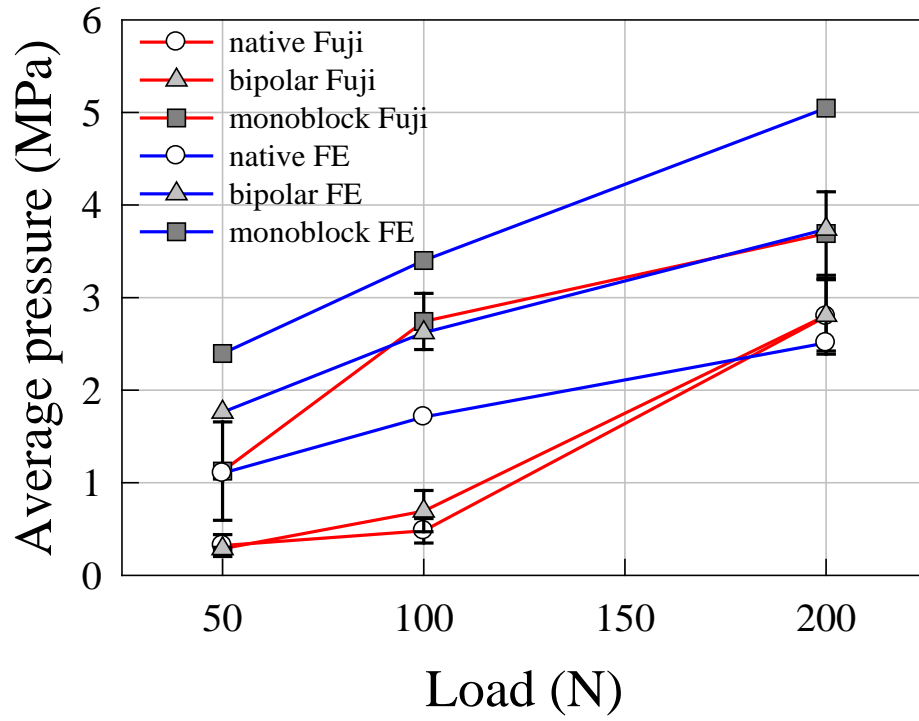


Figure 52. Average pressure comparison

7.0 DISCUSSION

In this study, two different radial head implants were compared with native radial head in terms of the maximum contact stress, contact area, and average pressure using FE models and cadaveric testing with Fuji pressure sensitive film. Even though FE predictions overestimated the maximum contact stress and underestimated contact area compared to measurements from cadaveric elbow testing, there was general agreement in the maximum contact stress and contact area between FE predictions and measurements from the testing with an average difference of 17%, which may seem like a big difference but it can be considered reasonable considering the accuracy of the Fuji film. Once A and C films are combined and sealed for use, the effective thickness of a film packet reaches 0.3 mm and the elastic modulus is approximately 100 MPa in compression [131], which is approximately 10 times stiffer than cartilage. Thus, inserting the film packet into the articular joint will alter the contact mechanics of the joint and lead to the discrepancies between actual contact characteristics and measured data from Fuji film [132-134]. The limitations of the Fuji pressure sensitive film including handling, sensitivity to shear stress, temperature, humidity, and a threshold effect have been reported [135, 136]. Additionally, the maximum contact stress and contact area calculated by custom MATLAB programs used in this study could involve up to 10% difference from the actual pressure and area [130]. Stewart et al. [137] compared the maximum contact pressure measured from Fuji film to one calculated from the linear elasticity theory and found that the maximum contact stress calculated from Fuji film was larger than that calculated from the theory. Szivek et al. [136] reported that Fuji film underestimated the contact stress and overestimated the contact area compared to the calibrated electrical resistance contact stress and area measurements. However, Harris et al. [138] compared contact areas measured from Fuji film

and K-scan sensor and found that contact areas from Fuji film were 11 to 36% lower than those measured by K-scan sensor. Wu et al. [132] constructed FE models with and without pressure sensitive film and compared the maximum contact stress. They concluded that inserting a pressure sensitive film can change the maximum contact stress by 10 to 26% depending on loading, geometry of the joints, and the mechanical properties of the cartilage. They also noted that the measured contact pressure using a pressure sensitive film may contain errors from 14 to 28% considering the measurement precision of the film (approximately 10%). Liao et al. [133-134] investigated the effect of inserting a Fuji film into tibiofemoral joint on measuring the maximum contact stress and the contact area using 2-D and 3-D FE models and reported that the maximum differences in the contact area and the maximum contact stress between FE predictions and measurements from Fuji film were 16.1 and 13% respectively. In this study, measured contact stress from Fuji film was always lower than FE predictions, which concurs with Stewart and Szivek's findings.

In order to reduce the discrepancy between FE predictions and the experimental measurements, FE analyses with several different combinations of the elastic properties for the bone and cartilage were conducted. The linear elastic material properties for the cartilage ranged from 10 to 15 MPa for elastic modulus and from 0.4 to 0.45 for Poisson's ratio from literature. After testing several different combinations for elastic material properties of the cartilage, 10 MPa and 0.4 were chosen as this combination produced the best matched results to the measurements from cadaveric testing. In addition, a neo Hookean hyperelastic model for the cartilage, which was used by some researchers [125, 139, 140] for FE modeling for the cartilage, was compared to a linear elastic model; it took longer computation time and did not make a significant difference in the maximum contact stress. Several different combinations for material properties of the bone

were also tested as well but there was no significant difference found. Other than material properties of the bone and cartilage, obtaining the exact shape of the cartilage and adding more soft tissues including muscles and interosseous membrane can help reducing the gap FE predictions and measurements.

Unlike the maximum contact stress and the contact area, there was a large difference in average pressure between FE predictions and measurements from Fuji film. The primary reason for this was that average pressures from cadaveric testing were calculated by combining averages from super low and low grades of film and that average pressure itself may involve larger errors than the maximum contact stress and contact area because average pressure could be affected more by artifacts of Fuji film such as folding, buckling and sliding. During the testing it was difficult to avoid the artifacts of Fuji film which led to mottled stains. Some regions in the defined stain boundary were darker and some spots were stainless or lighter especially for native and bipolar cases mainly due to the small radius of the curvature of the contacting surface. This subsequently led to lower average pressure. The monoblock was easiest to get a good stain on Fuji film for all three loading cases because the monoblock implant had the largest radius of curvature, which was more congruent with flat Fuji film than native or bipolar and produced less artifacts on the film.

The differences between the native, monoblock and bipolar cases in the maximum contact stress and contact area resulted mainly from the differences in radii of curvature, i.e., from the differences in congruency between contact areas (capitellum and radial head for native or capitellum and implant). The radii of curvature for the native, monoblock, and bipolar were approximately 13.30, 37.73, and 15.80 mm respectively. The native case showed the lowest maximum contact stresses and highest contact areas due to the smallest differences between radii of curvature of the contact surfaces. The difference between monoblock and bipolar in maximum

contact stress and contact area was as large as the difference between native and bipolar. Therefore, the radius of curvature was the most important factor to determine the contact stress in the radial head. The smaller the radius of curvature, the larger the contact area on the radial head and the lower the contact stress. In this study, only one design from each of two different types of radial head implant was evaluated and compared. Their shape is axisymmetric like most of other implants on the market. There is currently one anatomically shaped prosthesis (Acumed Anatomical Radial Head System, Hillboro, OR, USA) available for use, which relies on precise placement and secure fixation. This implant is supposed to have lower contact stress than two implants tested in this study. However, anatomical landmarks (biceps tuberosity and major axis of radial head) used for proper implant alignment have been shown to be poorly correlated with each other [141] and can be damaged during injury.

The stress level that can damage cartilage varies depending on types of loading (impact, cyclic, and slowly rising load), the magnitude of stress, stress rate, loading duration and so on. Single high impact larger than 20 MPa can lead to chondrocyte death associated with the damage of cartilage matrix [142-144]. Cell death and matrix damage with a slow loading rate were also reported [144]. Quinn et al. [145] observed chondrocyte death under 7 MPa using an extremely slow strain rate of 3×10^{-5} /s. For cyclic loading chondrocyte death was found at 4.5 to 5 MPa [146-148]. Comparing the maximum contact stresses obtained in this study with stress level that caused cartilage damage mentioned above, chondrocyte death is not likely to happen for the native elbow under 200 N of applied load, which can be exerted on the radial head during pushups for a 60 kg man, since both the measured and predicted maximum contact stresses were below 4.5 MPa whereas cartilage damage is more likely to happen to the bipolar and monoblock implanted elbow (the maximum contact stresses for the bipolar and monoblock were 5.9 MPa and 7.62 MPa from

the testing, and 6.59 MPa and 8.64 MPa from FE respectively). This elevated stress level for both implants could cause arthritis.

For the native elbow, there was approximately 1 MPa of the maximum contact stress between the radial head and ulnar notch under 200 N of applied load, which was relatively not a substantial amount of pressure compared to the pressure between the radial head and capitellum. This stress was produced because the center of the radial head was located more medially than the center of the capitellum of the humerus, which made the radial head move toward the ulnar notch and possibly contributed to reducing the contact stress on the radiocapitellar joint. However, FE models for monoblock and bipolar implant showed none or a little contact stress in the ulnar notch mainly due to boundary conditions and size of the implants. For both monoblock and bipolar implants, little or zero stress was found in the ulnar notch because best matched size to the native radial head was a little smaller than the native radial head in circumference and implants did not move as much as the native radial head towards the ulnar notch resulting in a slight contact and a little contact stress. For the bipolar implant, the node in the center of distal surface was constrained in medial-lateral and anterior-posterior directions so that the implant could rotate as if there were a ball and socket joint in the distal surface of the bipolar implant (native radial head and monoblock implant were free to move in any directions). Thus, the bipolar implant was not allowed to translate toward the ulnar notch, which resulted in no contact stress in the ulnar notch.

There are several limitations of the FE models created in this study. First, the native elbow FE model included only the radial head, not the whole radius and the two implant FE models did not include stem of prosthesis. Thus, there were differences in loading conditions between FE models and experimental settings. In the experimental settings, load was applied at the distal end of the radius whereas load was applied at the distal surface of the radial head in the FE models.

Since the radius is not straight, the axial load applied at the distal end of the radius would produce shear load and moment on the radial head. In addition, the ulna was attached to the radius through the joint capsule and interosseous membrane. Therefore, load applied to the distal radius could have been distributed to the ulna through interosseous membrane. Second, bones were modeled as a linear elastic material and assumed to be whole cancellous bone. Third, cartilage was also modeled as a linear elastic material and its thickness was assumed to be uniform. Fourth, annular and radial collateral ligaments were modeled using a straight line element and no pre-tension was involved. Last, FE models did not include soft tissues such as muscles, joint capsule, and interosseous membrane.

8.0 CONCLUSION AND FUTURE WORK

Two basic types of radial head prosthesis were compared with the native radial head in terms of the maximum contact stress, contact area, and average pressure using FE analysis and Fuji pressure-sensitive film. A significant increase in the maximum contact stress and a significant reduction in the contact area were found when the native radial head was replaced with a prosthesis. The monoblock implant had the highest maximum contact stress and lowest contact area due to large difference in the radii of curvature between the implant and the capitellum. The native case had the lowest maximum contact stress and largest contact area due to the smallest difference in the radii of curvature between the radial head and the capitellum.

Constructed elbow FE models showed reasonable predictions in the maximum contact stress and the contact area with an average difference of 17% with experimental measurements. The maximum contact stress and average pressure for a bipolar implant were lower than those for a monoblock implant whereas the contact area for a bipolar implant was higher than that for a monoblock implant due to lower radius of curvature leading to better congruency with the capitellum. Thus, a radial head implant with more conforming design will potentially extend the life of prosthesis by reducing contact stress.

For the future work, various radial head implants with different design features including an anatomical implant can be analyzed using the created FE models. Various loading conditions including cyclic and impact loading can be tested at different flexion/extension angles and forearm rotations for more thorough comparison between implants and native radial head. Tactile sensors can be used for cyclic loading to investigate history of contact pressure and area during the course of loading. More soft tissues including muscles and interosseous membrane, exact geometry of

cartilage using CT arthrography or MRI, stem of the implant, and whole radius and ulna can be added to the FE models and will produce more accurate predictions. The effect of a ball and socket joint in the bipolar implant on the contact stress should be further evaluated since the radius of the curvature seemed to be the most important factor in determination of the contact stress in the static analysis. A ball and socket joint would be more influential to contact mechanics while the elbow is under dynamic motion. Furthermore, ligament and muscle forces can be compared using new FE models.

APPENDIX A

MATLAB CODE FOR CALCULATING CONTACT AREA FROM ANSYS DATA

ANSYS does not provide contact area from contact analysis. Thus, MATLAB code was written to calculate contact area using ANSYS contact analysis data.

```
close all;clc;clear all;
% read pressure data
f=fopen('P_KMI_1.1_300N01.txt','r'); % this file has node and pressure
g=fopen('N_KMI_1.1_300N01.txt','r'); % this file has node number and its
coordinates
h=fopen('E_KMI_1.1_300N01.txt','r'); % this file has element number and its
node numbers

x=0;
while (~feof(f))
    x1=cell2mat(textscan(f,'%n%n'));
    if x==0
        pressure=x1;
    else
        pressure=[pressure;x1];
    end
    x=x+1;
    hd=textscan(f,'%s',2);
end

% read node data
x=0;
while (~feof(g))
    hd=textscan(g,'%s',4);
    x1=cell2mat(textscan(g,'%n%n%n%n'));
    if x==0
        node=x1;
    else
        node=[node;x1];
    end
    x=x+1;
end

% read element data
x=0;
```

```

while (~feof(h))
    hd=textscan(h,'%s',1);
    x1=cell2mat(textscan(h,'%n%n%n%n'));
    if x==0
        element=x1;
    else
        element=[element;x1];
    end
    x=x+1;
end

fclose(f);fclose(g);fclose(h);

% find all the nodes with nonzero pressure and
% store those nodes in "Pnode"
N=length(pressure);k=1;
for i=1:N
    if pressure(i,2)~=0
        Pnode(k,1)=pressure(i,1);
        Pnode(k,2)=pressure(i,2);
        k=k+1;
    end
end

% find elements which include nodes with nonzero pressure and
% store those elements in "Pele"
N=0;
for i=1:length(Pnode)
    [P,Q]=find(element==Pnode(i,1));
    for j=1:length(P)
        if Q(j)~=1
            Pele(N+1)=element(P(j),1);
            N=length(Pele);
        end
    end
    N=length(Pele);
end

% find contact elements and store in "Cele"
% select elements referred only three times

k=1;
for i=1:N-2
    l=0;
    for j=i+1:N
        if Pele(i)==Pele(j)
            l=l+1;
        end
    end
    if l==2
        Cele(k)=Pele(i);
        k=k+1;
    end
end

% O=fopen('element.txt','wt');

```

```

% for i=1:length(Cele)
%     fprintf(0,'esel,a,,,%i\n',Cele(i));
% end
% fclose(0);

% calculate the contact area and average contact pressure
pp=zeros(3,1);
X1=zeros(1,3);X2=X1;X3=X1;
for i=1:length(Cele)
    % find node numbers
    a=element(find(element(:,1)==Cele(i)),2);
    b=element(find(element(:,1)==Cele(i)),3);
    c=element(find(element(:,1)==Cele(i)),4);
    % find coordinates of nodes
    X1(1,1:3)=node(find(node(:,1)==a),2:4);
    X2(1,1:3)=node(find(node(:,1)==b),2:4);
    X3(1,1:3)=node(find(node(:,1)==c),2:4);
    A1=X2-X1;
    A2=X3-X1;
    Area(i)=1/2*norm(cross(A1,A2));% contact area
    % find contact pressure of nodes
    pp(1,1)=Pnode(find(Pnode(:,1)==a),2);
    pp(2,1)=Pnode(find(Pnode(:,1)==b),2);
    pp(3,1)=Pnode(find(Pnode(:,1)==c),2);
    p_ave=mean(pp);
    Load(i)=Area(i)*p_ave;% load of element = average pressure*area
end
cont_area=sum(Area)% total contact area
ave_cont_pressure=sum(Load)/cont_area% average contact pressure

```

APPENDIX B

MATLAB CODE FOR CALCULATING THE MAXIMUM PRESSURE AND CONTACT

AREA FROM FUJI FILM

1. Converter for super low grade film

```
% Converts files from intensity to stress using the
% packed super low calibration curve. Fuji film calibration
%
%tic
clear converted
value = [0.482607402528207 -6.81061939900793 ...
        35.8010236729056 -80.3941366180204 49.3947595012293 ...
        202.710120235178]; % AGH(MM) cal 10/29/2009
%value = [-6.1077 63.5702 -222.9934 309.8493 -183.6146 236.83];
% value = [1.4794 -24.8158 151.2773 -407.2953 434.5182 57.4009];%230 recal
6/21/06
% similar to 220 threshold on 7/25/2007
converted = zeros(size(easy));
[row,col] = size(easy);
sl_root = zeros(1,256);

hl = waitbar(0,' Working? ');

for no = 1:256,
    newvalue = value;
    newvalue(6) = newvalue(6) - (no-1); % Subtract intensity from last
    all_roots(no,:) = roots(newvalue); % number in polynomial
    if isempty(all_roots(no,:)) == 1,% Check for no roots
        sl_root(no) = 0;
    % elseif no >= 203,
    %     sl_root(no) = 0;
    % elseif no < 203,
    else
        rcount = 0;% Number of real roots of polynomial
        for real_check = 1:5,
            crappily(real_check) = isreal(all_roots(no,real_check));
        end
        index_crap = find(crappily == 1);
        index_positive = find(all_roots(no,index_crap)>0);
        if sum(crappily == 1) > 1,
            if sum(index_crap(index_positive)== 4 ) == 1,
                sl_root(no) = all_roots(no,4);
            else
```

```

        sl_root(no) = min(all_roots(no,index_crap(index_positive)));
    end
elseif isempty(index_positive) == 1 && no < 160,
    sl_root(no) = 4;
%
%   else
%       sl_root(no) = all_roots(no,find(crappily == 1));
elseif isempty(index_positive) == 0 && no > 212,
    sl_root(no) = 0.2;
%
%       sl_root(no) = all_roots(no,find(crappily == 1));
end
%
%   for number = 1:5,
%       if (isreal(all_roots(number)) == 1 && all_roots(number)>0),
%           rcount = rcount + 1;
%           real_roots(rcount) = all_roots(number);
%       end
%   end
%   if exist('real_roots') == 1,% Over calibration range, min. root
%       mincheck = real_roots > 1;
%       x = find(mincheck == 1);
%       if size(real_roots,2) > 1 && max(mincheck) == 1,
%           sl_root(no) = min(real_roots(x));% is the desired root
%       else
%           sl_root(no) = min(real_roots);
%       end
%       clear real_roots
%   else
%       sl_root(no) = 0;
%   end
end
end

for k = 1:row,% Getting the stress intensities
    for l = 1:col,
        no = double(easy(k,l)) + 1;
        converted(k,l) = sl_root(no);
    end
    waitbar(k/row,h1,round(1000*k/row)/10) % Keeps track of place in
conversion process
end
close(h1)
%toc
clear h1 k l row col value all_roots rcount temp no x mincheck

```

2. Converter for low grade film

```

% Converts files from intensity to stress using the
% packed low calibration curve. Fuji film calibration
%
%tic
clear converted
value = [-0.037130174801952 0.815333434066532 ...
        -6.99345756917711 31.2803961669103 -88.6486495110474 ...
        308.91358173628];% AGH(MM) cal 10/29/2009
%value = [-.0072 .1894 -1.5757 3.3845 -.213 195.0508];%215
%value = [-.0012 -.0016 0.739 -9.6942 30.5435 188.177];%230

```

```

%value = [-.007 .2373 -2.6476 11.0821 -25.6138 255.2056];%245
[row,col] = size(easy);
converted = zeros(size(easy));

h1 = waitbar(0,' Working? ');

for no = 1:256,
    newvalue = value;
    newvalue(6) = newvalue(6) - (no-1);      % Subtract intensity from last
    all_roots(no,:) = roots(newvalue);      % number in polynomial
    for real_check = 1:5,
        crappily(real_check) = isreal(all_roots(no,real_check));
    end
    l_root(no) = all_roots(no,find(crappily == 1));
end

for k = 1:row,% Getting the stress intensities
    for l = 1:col,
        no = double(easy(k,l)) + 1;
        converted(k,l) = l_root(no);
    end
    waitbar(k/row,h1,round(1000*k/row)/10) % Keeps track of place in
conversion process
end
close(h1)
%toc
clear h1 k l row col value all_roots rcount temp no

```

3. Program to calculate the maximum contact stress and the contact area for super low grade film

```

% Fuji film processing
%
% Select area in easy that is of interest and
% defines it to be 0(zero) using im2bw on easy.
format compact
set(0,'recursionlimit',750)
done1 = 1;
while done1 == 1,
    done1 = menu('Load Next Super Low *.mat file?',' YES!! ',' No ');

    switch done1
        case 2
            % end of run
        case 1
            done= 0;
            % Load and plot next mat file
            [file,pathname] = uigetfile('*.mat','Load Mat File');
            fullfile(pathname,file)
            easy = importdata(fullfile(pathname,file));

            while done ~=1,
                done = menu('Choose an action','Done',...
                    'Select Fuji Stain','A and P Calculation');
                switch done

```

```

case 1,      % Action = done
    %close(h+1);
case 2,      % Action = select stain from mat file
    figure(1)
    imagesc(easy,[0 4]), colorbar horiz,
    axis image, [maxrow,maxcol] = size(easy);
    title(file)
    [X,Y] = ginput(2); % Input X,Y coordinates of
    X = ceil(X);      % scanned fuji film
    Y = ceil(Y);
    for n = 1:2,
        if X(n) > maxcol, %Ensure X is within bounds
            X(n) = maxcol;
        elseif X(n) < 1,
            X(n) = 1;
        end
        if Y(n) > maxrow, % Ensure Y is within bounds
            Y(n) = maxrow;
        elseif Y(n) < 1,
            Y(n) = 1;
        end
    end
    easy1 = easy(min(Y):max(Y),min(X):max(X));
    imagesc(easy1,[0 4]),colormap('jet'),
    axis image, colorbar horiz, title(file)
case 3,      % Calculate areas and pressures
    figure(2),

%
        binary = im2bw(easy1,0.8);
        %Select polygonal area for calculation
        crappymatlab(:,:,1) = easy1;
        crappymatlab(:,:,2) = easy1;
        crappymatlab(:,:,3) = easy1;
        maxcrap = max(max(max(crappymatlab)));
%
        bw = roipoly(binary);
        bw = roipoly(crappymatlab/maxcrap);
        clear maxcrap crappymatlab

    imagesc(easy1.*bw,[0 4]), colorbar('horiz'), axis
image,
    colormap('jet'), title('Area used in Calculation')
% Making our filters
%
    h1 = fspecial('average',3);
    h2 = fspecial('average',5);
%
    h3 = fspecial('average',7);      h4 =
fspecial('average',9);
%
    h5 = fspecial('average',11);     h6 =
fspecial('average',13);
%
    h7 = fspecial('average',15);     h8 =
fspecial('average',17);
%
    h9 = fspecial('average',19);     h10 =
fspecial('average',21);
%
    h11 = fspecial('average',23);
    h12 = fspecial('average',25);
%h13 = fspecial('average',35);     h14 =
fspecial('average',45);

```

```

% Filtering the areas after ensuring max value is
% 3MPa
clear rows cols
[rows,cols] = find(easy1.*bw >=3);
if isempty(rows) == 0,
    %[maxrow1,maxcol1] = size(easy1);
    maxrow1 = length(rows);
    maxrow1 = (max(rows) - min(rows))+1;
    hbar = waitbar(0,'Going');
    for n = 1:maxrow1,
        k = find(easy1(n+min(rows)-1,:) >= 3);
        easy1(n+min(rows)-1,k) = 3;

waitbar(n/maxrow1,hbar,round(1000*n/maxrow1)/10);
        %easy1(rows(n),cols(n)) = 3;
%
waitbar(n/maxrow1,hbar,round(1000*n/maxrow1)/10);
        end% Maximum value
        close(hbar)
    end
%
% no1 = imfilter(easy1.*bw,h1); no2 =
imfilter(easy1.*bw,h2);
% no3 = imfilter(easy1.*bw,h3); no4 =
imfilter(easy1.*bw,h4);
% no5 = imfilter(easy1.*bw,h5); no6 =
imfilter(easy1.*bw,h6);
% no7 = imfilter(easy1.*bw,h7); no8 =
imfilter(easy1.*bw,h8);
% no9 = imfilter(easy1.*bw,h9); no10 =
imfilter(easy1.*bw,h10);
% no11 = imfilter(easy1.*bw,h11);
no12 = medfilt2(easy1.*bw,[5 5]);
% no12 = imfilter(easy1.*bw,h2);% changed from h12
% no13 = imfilter(easy1.*bw,h13); no14 =
imfilter(easy1.*bw,h14);
% Calculating areas
% area1 = roicolor(no1,0.1,20); areas(1) =
bwarea(area1)*(25.4/600)^2;
% area2 = roicolor(no2,0.1,20); areas(2) =
bwarea(area2)*(25.4/600)^2;
% area3 = roicolor(no3,0.1,20); areas(3) =
bwarea(area3)*(25.4/600)^2;
% area4 = roicolor(no4,0.1,20); areas(4) =
bwarea(area4)*(25.4/600)^2;
% area5 = roicolor(no5,0.1,20); areas(5) =
bwarea(area5)*(25.4/600)^2;
% area6 = roicolor(no6,0.1,20); areas(6) =
bwarea(area6)*(25.4/600)^2;
% area7 = roicolor(no7,0.1,20); areas(7) =
bwarea(area7)*(25.4/600)^2;
% area8 = roicolor(no8,0.1,20); areas(8) =
bwarea(area8)*(25.4/600)^2;
% area9 = roicolor(no9,0.1,20); areas(9) =
bwarea(area9)*(25.4/600)^2;
% area10 = roicolor(no10,0.1,20); areas(10) =
bwarea(area10)*(25.4/600)^2;

```

```

%           area11 = roicolor(no11,0.1,20); areas(11) =
bwarea(area11)*(25.4/600)^2;
%           area12 = roicolor(no12,0.1,20); areas =
bwarea(area12)*(25.4/600)^2;
%           area13 = roicolor(no13,0.1,20); areas(13) =
bwarea(area13)*(25.4/600)^2;
%           area14 = roicolor(no14,0.1,20); areas(14) =
bwarea(area14)*(25.4/600)^2;
%           Calculating max. and avg. pressures
%           maxpress(1) = max(max(no1)); maxpress(2) =
max(max(no2));
%           maxpress(3) = max(max(no3)); maxpress(4) =
max(max(no4));
%           maxpress(5) = max(max(no5)); maxpress(6) =
max(max(no6));
%           maxpress(7) = max(max(no7)); maxpress(8) =
max(max(no8));
%           maxpress(9) = max(max(no9)); maxpress(10) =
max(max(no10));
%           maxpress(11) = max(max(no11));
maxpress = max(max(no12));
%           maxpress(13) = max(max(no13)); maxpress(14) =
max(max(no14));

%           avgpress(1) = sum(sum(no1.*area1))/bwarea(area1);
%           avgpress(2) = sum(sum(no2.*area2))/bwarea(area2);
%           avgpress(3) = sum(sum(no3.*area3))/bwarea(area3);
%           avgpress(4) = sum(sum(no4.*area4))/bwarea(area4);
%           avgpress(5) = sum(sum(no5.*area5))/bwarea(area5);
%           avgpress(6) = sum(sum(no6.*area6))/bwarea(area6);
%           avgpress(7) = sum(sum(no7.*area7))/bwarea(area7);
%           avgpress(8) = sum(sum(no8.*area8))/bwarea(area8);
%           avgpress(9) = sum(sum(no9.*area9))/bwarea(area9);
%           avgpress(10) =
sum(sum(no10.*area10))/bwarea(area10);
%           avgpress(11) =
sum(sum(no11.*area11))/bwarea(area11);
%           avgpress = sum(sum(no12.*area12))/bwarea(area12);
%           avgpress(13) =
sum(sum(no11.*area13))/bwarea(area13);
%           avgpress(14) =
sum(sum(no12.*area14))/bwarea(area14);
%           maxpress;
%           avgpress;
%           areas
%           clipboard('copy',areas);
%           maxpress
%           maxpress_zero = max(max(easy1.*bw));
%           area0 = roicolor(easy1,3,20); areas_zero =
bwarea(area0)*(25.4/600)^2;
%           avgpress_zero =
sum(sum(easy1.*bw.*area0))/bwarea(area0);
%           figure(3), subplot(221), imagesc(easy1.*bw,[0 4]),
%           set(gca,'XTickLabel',''), set(gca,'YTickLabel',''),
%           subplot(222), imagesc(no4,[0 4]),
set(gca,'XTickLabel',''),

```

```

%                                     set(gca,'YTickLabel',''), subplot(223),
imagesc(no8,[0 4]),
%                                     set(gca,'XTickLabel',''), set(gca,'YTickLabel',''),
%                                     subplot(224), imagesc(no12,[0 4]),
set(gca,'XTickLabel',''),
%                                     set(gca,'YTickLabel','')
        end% switch done
    end%while done
end% switch donel
end% while donel

clear done maxcol maxrow number h X Y rown coln n easy i j bw bw2 bw3
clear ha bw maxcoll maxrowl

```

4. Program to calculate the maximum contact stress and the contact area for low grade film

```

% Fuji film processing
%
% Select area in easy that is of interest and
% defines it to be 0(zero) using im2bw on easy.
%
% Muturi, 31st May 2005
%       , 25th Jan 2006
%       , 2nd Nov 2009 medfilt2 instead of imfilter
format compact
set(0,'recursionlimit',750)
donel = 1;
while donel == 1,
    donel = menu('Load Next LOW *.mat file?',' YES!! ',' No ');

    switch donel
        case 2
            % end of run
        case 1
            done= 0;
            % Load and plot next mat file
            [file,pathname] = uigetfile('*.mat','Load Mat File');
            fullfile(pathname,file)
            cd(pathname)
            easy = importdata(fullfile(pathname,file));

            while done ~=1,
                done = menu('Choose an action','Done',...
                    'Select Fuji Stain','A and P Calculation');
                switch done
                    case 1, % Action = done
                        %close(h+1);
                    case 2, % Action = select stain from mat file
                        figure(1)
                        imagesc(easy,[3 10]), colorbar horiz,
                        axis image, [maxrow,maxcol] = size(easy);
                        [X,Y] = ginput(2); % Input X,Y coordinates of
                        X = ceil(X); % scanned fuji film
                        Y = ceil(Y);
                        for n = 1:2,
                            if X(n) > maxcol, %Ensure X is within bounds

```

```

        X(n) = maxcol;
    elseif X(n) < 1,
        X(n) = 1;
    end
    if Y(n) > maxrow, % Ensure Y is within bounds
        Y(n) = maxrow;
    elseif Y(n) < 1,
        Y(n) = 1;
    end
end
easy1 = easy(min(Y):max(Y),min(X):max(X));
imagesc(easy1,[0 10]),colormap('jet'),
axis image, colorbar horiz, title(file)
case 3, % Calculate areas and pressures
figure(2),
% Select polygonal area for calculation
%
%
    binary = im2bw(easy1-3,1);
    bw = roipoly(binary);
crappymatlab(:,:,1) = easy1;
crappymatlab(:,:,2) = easy1;
crappymatlab(:,:,3) = easy1;
maxcrap = max(max(max(crappymatlab)));
bw = roipoly(crappymatlab/maxcrap);
clear maxcrap crappymatlab

%
%
    bw = roipoly(easy1-3);
image imagesc(easy1.*bw,[3 10]), colorbar('horiz'), axis
    colormap('jet'), title('Area used in Calculation')
% Making our filters
%
%
    h1 = fspecial('average',3);    h2 =
    h3 = fspecial('average',7);    h4 =
    h5 = fspecial('average',11);   h6 =
    h7 = fspecial('average',15);   h8 =
    h9 = fspecial('average',19);   h10 =
    h11 = fspecial('average',23);
    h12 = fspecial('average',25);
    h13 = fspecial('average',35);  h14 =
%
%
    fspecial('average',45);
% Filtering the areas after ensuring max value is
% 3MPa
clear rows cols
[rows,cols] = find(easy1.*bw >=9.58);
if isempty(rows) == 0,
    %[maxrow1,maxcol1] = size(easy1);
    maxrow1 = length(rows);
    maxrow1 = (max(rows) - min(rows)) + 1;
    hbar = waitbar(0,'Going');
    for n = 1:maxrow1,
        k = find(easy1(n+min(rows)-1,:) >= 9.58);
        easy1(n+min(rows)-1,k) = 9.58;
    %
        easy1(rows(n),cols(n)) = 9.58;
    %

```

```

waitbar(n/maxrow1,hbar,round(1000*n/maxrow1)/10);
        end% Maximum value
        close(hbar)
    end
%
%       no1 = imfilter(easy1.*bw,h1,3);   no2 =
imfilter(easy1.*bw,h2,3);
%       no3 = imfilter(easy1.*bw,h3,3);   no4 =
imfilter(easy1.*bw,h4,3);
%       no5 = imfilter(easy1.*bw,h5,3);   no6 =
imfilter(easy1.*bw,h6,3);
%       no7 = imfilter(easy1.*bw,h7,3);   no8 =
imfilter(easy1.*bw,h8,3);
%       no9 = imfilter(easy1.*bw,h9,3);   no10 =
imfilter(easy1.*bw,h10,3);
%       no11 = imfilter(easy1.*bw,h11,3);
%       no12 = imfilter(easy1.*bw,h12,3);
%       no12 = medfilt2(easy1.*bw,[5 5]);
%       no13 = imfilter(easy1.*bw,h13,3); no14 =
imfilter(easy1.*bw,h14,3);
%       Calculating areas
%       area1 = roicolor(no1,3,20);   areas(1) =
bwarea(area1)*(25.4/600)^2;
%       area2 = roicolor(no2,3,20);   areas(2) =
bwarea(area2)*(25.4/600)^2;
%       area3 = roicolor(no3,3,20);   areas(3) =
bwarea(area3)*(25.4/600)^2;
%       area4 = roicolor(no4,3,20);   areas(4) =
bwarea(area4)*(25.4/600)^2;
%       area5 = roicolor(no5,3,20);   areas(5) =
bwarea(area5)*(25.4/600)^2;
%       area6 = roicolor(no6,3,20);   areas(6) =
bwarea(area6)*(25.4/600)^2;
%       area7 = roicolor(no7,3,20);   areas(7) =
bwarea(area7)*(25.4/600)^2;
%       area8 = roicolor(no8,3,20);   areas(8) =
bwarea(area8)*(25.4/600)^2;
%       area9 = roicolor(no9,3,20);   areas(9) =
bwarea(area9)*(25.4/600)^2;
%       area10 = roicolor(no10,3,20); areas(10) =
bwarea(area10)*(25.4/600)^2;
%       area11 = roicolor(no11,3,20); areas(11) =
bwarea(area11)*(25.4/600)^2;
%       area12 = roicolor(no12,3,20); areas =
bwarea(area12)*(25.4/600)^2;
%       area13 = roicolor(no13,3,20); areas(13) =
bwarea(area13)*(25.4/600)^2;
%       area14 = roicolor(no14,3,20); areas(14) =
bwarea(area14)*(25.4/600)^2;
%       Calculating max. and avg. pressures
%       maxpress(1) = max(max(no1));   maxpress(2) =
max(max(no2));
%       maxpress(3) = max(max(no3));   maxpress(4) =
max(max(no4));
%       maxpress(5) = max(max(no5));   maxpress(6) =
max(max(no6));

```

```

%           maxpress(7) = max(max(no7));       maxpress(8) =
max(max(no8));
%           maxpress(9) = max(max(no9));       maxpress(10) =
max(max(no10));
%           maxpress(11) = max(max(no11));
maxpress = max(max(no12))
clipboard('copy',maxpress);
%           maxpress(13) = max(max(no13));     maxpress(14) =
max(max(no14));
%           avgpress(1) = sum(sum(no1.*area1))/bwarea(area1);
%           avgpress(2) = sum(sum(no2.*area2))/bwarea(area2);
%           avgpress(3) = sum(sum(no3.*area3))/bwarea(area3);
%           avgpress(4) = sum(sum(no4.*area4))/bwarea(area4);
%           avgpress(5) = sum(sum(no5.*area5))/bwarea(area5);
%           avgpress(6) = sum(sum(no6.*area6))/bwarea(area6);
%           avgpress(7) = sum(sum(no7.*area7))/bwarea(area7);
%           avgpress(8) = sum(sum(no8.*area8))/bwarea(area8);
%           avgpress(9) = sum(sum(no9.*area9))/bwarea(area9);
%           avgpress(10) =
sum(sum(no10.*area10))/bwarea(area10);
%           avgpress(11) =
sum(sum(no11.*area11))/bwarea(area11);
%           avgpress = sum(sum(no12.*area12))/bwarea(area12);
%           avgpress(13) =
sum(sum(no13.*area11))/bwarea(area13);
%           avgpress(14) =
sum(sum(no14.*area12))/bwarea(area14);
%           maxpress
%           avgpress
%           areas(12)
maxpress_zero = max(max(easy1.*bw));
area0 = roicolor(easy1,3,20);   areas_zero =
bwarea(area0)*(25.4/600)^2;
%           avgpress_zero =
sum(sum(easy1.*bw.*area0))/bwarea(area0)
%           figure(3), subplot(221), imagesc(easy1.*bw,[0 10]),
%           set(gca,'XTickLabel',''), set(gca,'YTickLabel',''),
%           subplot(222), imagesc(no4,[0 10]),
set(gca,'XTickLabel',''),
%           set(gca,'YTickLabel',''), subplot(223),
imagesc(no8,[0 10]),
%           set(gca,'XTickLabel',''), set(gca,'YTickLabel',''),
%           subplot(224), imagesc(no12,[0 10]),
set(gca,'XTickLabel',''),
%           set(gca,'YTickLabel','')
end% switch done
end%while done
end% switch done1
end% while done1

clear done maxcol maxrow number h X Y rown coln n easy i j bw bw2 bw3
clear ha bw maxcol1 maxrow1

```

BIBLIOGRAPHY

1. Morrey, B.F., *The elbow and its disorders*. 3rd ed. 2000, Philadelphia: Saunders.
2. Taylor, T.K. and B.T. O'Connor, *The Effect Upon the Inferior Radio-Ulnar Joint of Excision of the Head of the Radius in Adults*. J Bone Joint Surg Br, 1964. **46**: p. 83-8.
3. Morrey, B.F., *Current concepts in the treatment of fractures of the radial head, the olecranon, and the coronoid*. Instr Course Lect, 1995. **44**: p. 175-85.
4. Calfee, R., I. Madom, and A.P. Weiss, *Radial head arthroplasty*. J Hand Surg Am, 2006. **31**(2): p. 314-21.
5. Mason, M.L., *Some observations on fractures of the head of the radius with a review of a hundred cases*. Br J Surg, 1954. **42**: p. 123-32.
6. Morrey, B.F., L. Askew, and E.Y. Chao, *Silastic prosthetic replacement for the radial head*. J Bone Joint Surg Am, 1981. **63**(3): p. 454-8.
7. Vanderwilde, R.S., et al., *Inflammatory arthritis after failure of silicone rubber replacement of the radial head*. J Bone Joint Surg Br, 1994. **76**(1): p. 78-81.
8. Worsing, R.A., Jr., W.D. Engber, and T.A. Lange, *Reactive synovitis from particulate silastic*. J Bone Joint Surg Am, 1982. **64**(4): p. 581-5.
9. Harrington, I.J., et al., *The functional outcome with metallic radial head implants in the treatment of unstable elbow fractures: a long-term review*. J Trauma, 2001. **50**(1): p. 46-52.
10. Knight, D.J., et al., *Primary replacement of the fractured radial head with a metal prosthesis*. J Bone Joint Surg Br, 1993. **75**(4): p. 572-6.
11. Moro, J.K., et al., *Arthroplasty with a metal radial head for unreconstructible fractures of the radial head*. J Bone Joint Surg Am, 2001. **83-A**(8): p. 1201-11.
12. Morrey, B.F., L.J. Askew, and E.Y. Chao, *A biomechanical study of normal functional elbow motion*. J Bone Joint Surg Am, 1981. **63**(6): p. 872-7.
13. Margareta Nordin, V.H.F., *Basic biomechanics of the musculoskeletal system*. 3rd edition ed. 2001: Lippincott Williams & Wilkins.
14. An, K.N., K.R. Kaufman, and E.Y. Chao, *Physiological considerations of muscle force through the elbow joint*. J Biomech, 1989. **22**(11-12): p. 1249-56.

15. Askew, L.J., et al., *Isometric elbow strength in normal individuals*. Clin Orthop Relat Res, 1987(222): p. 261-6.
16. Bennett, J.M. and T.L. Mehlhoff, *Reconstruction of the medial collateral ligament of the elbow*. J Hand Surg Am, 2009. **34**(9): p. 1729-33.
17. Morrey, B.F., S. Tanaka, and K.N. An, *Valgus stability of the elbow. A definition of primary and secondary constraints*. Clin Orthop Relat Res, 1991(265): p. 187-95.
18. Morrey, B.F. and K.N. An, *Articular and ligamentous contributions to the stability of the elbow joint*. Am J Sports Med, 1983. **11**(5): p. 315-9.
19. Doria, A., et al., *Recurrent dislocation of the elbow*. Int Orthop, 1990. **14**(1): p. 41-5.
20. Durig, M., et al., *The operative treatment of elbow dislocation in the adult*. J Bone Joint Surg Am, 1979. **61**(2): p. 239-44.
21. Josefsson, P.O., O. Johnell, and B. Wendeborg, *Ligamentous injuries in dislocations of the elbow joint*. Clin Orthop Relat Res, 1987(221): p. 221-5.
22. O'Driscoll, S.W., D.F. Bell, and B.F. Morrey, *Posterolateral rotatory instability of the elbow*. J Bone Joint Surg Am, 1991. **73**(3): p. 440-6.
23. O'Driscoll, S.W., et al., *Elbow subluxation and dislocation. A spectrum of instability*. Clin Orthop Relat Res, 1992(280): p. 186-97.
24. Dunning, C.E., et al., *Ligamentous stabilizers against posterolateral rotatory instability of the elbow*. J Bone Joint Surg Am, 2001. **83-A**(12): p. 1823-8.
25. Hotchkiss, R.N. and A.J. Weiland, *Valgus stability of the elbow*. J Orthop Res, 1987. **5**(3): p. 372-7.
26. Berquist, T.H., *MRI of Musculoskeletal System*. 5th edition ed. 2005: Lippincott Williams & Wilkins.
27. King, G.J., et al., *An anthropometric study of the radial head: implications in the design of a prosthesis*. J Arthroplasty, 2001. **16**(1): p. 112-6.
28. Swieszkowski, W., et al., *The anatomic features of the radial head and their implication for prosthesis design*. Clin Biomech (Bristol, Avon), 2001. **16**(10): p. 880-7.
29. van Riet, R.P., et al., *The noncircular shape of the radial head*. J Hand Surg Am, 2003. **28**(6): p. 972-8.
30. Nordin, M. and F.V. H., *Basic biomechanics of the musculoskeletal system*. 2001: Lippincott Williams & Wilkins.
31. Halls, A.A. and A. Travill, *Transmission of Pressures across the Elbow Joint*. Anat Rec, 1964. **150**: p. 243-7.

32. Amis, A.A., D. Dowson, and V. Wright, *Elbow joint force predictions for some strenuous isometric actions*. J Biomech, 1980. **13**(9): p. 765-75.
33. Amis, A.A., J.H. Miller, and D. Dowson, *Biomechanical aspects of the elbow; joint forces related to prosthesis design*. Eng Med, 1981. **10**: p. 65-8.
34. King, G.J., *Management of radial head fractures with implant arthroplasty*. J of the American society for surgery of the hand, 2004. **4**: p. 11-26.
35. Sabo, M.T., et al., *A morphological analysis of the humeral capitellum with an interest in prosthesis design*. J Shoulder Elbow Surg, 2011. **20**(6): p. 880-4.
36. Rho, J.Y., L. Kuhn-Spearing, and P. Zioupos, *Mechanical properties and the hierarchical structure of bone*. Med Eng Phys, 1998. **20**(2): p. 92-102.
37. Stolk, J., et al., *Finite element and experimental models of cemented hip joint reconstructions can produce similar bone and cement strains in pre-clinical tests*. J Biomech, 2002. **35**(4): p. 499-510.
38. Yoon, H.S. and J.L. Katz, *Ultrasonic wave propagation in human cortical bone-I. Theoretical considerations for hexagonal symmetry*. J Biomech, 1976. **9**(6): p. 407-12.
39. Ashman, R.B., et al., *A continuous wave technique for the measurement of the elastic properties of cortical bone*. J Biomech, 1984. **17**(5): p. 349-61.
40. Frankel, V.H. and M. Nordin, *Basic biomechanics of the skeletal system*. 1980: Philadelphia: Lea & Febiger.
41. Schenck, R.C., Jr., et al., *A biomechanical analysis of articular cartilage of the human elbow and a potential relationship to osteochondritis dissecans*. Clin Orthop Relat Res, 1994(299): p. 305-12.
42. Shepherd, D.E. and B.B. Seedhom, *Thickness of human articular cartilage in joints of the lower limb*. Ann Rheum Dis, 1999. **58**(1): p. 27-34.
43. Armstrong, C.G. and D.L. Gardner, *Thickness and distribution of human femoral head articular cartilage. Changes with age*. Ann Rheum Dis, 1977. **36**(5): p. 407-12.
44. Wyler, A., et al., *Comparison of MR-arthrography and CT-arthrography in hyaline cartilage-thickness measurement in radiographically normal cadaver hips with anatomy as gold standard*. Osteoarthritis Cartilage, 2009. **17**(1): p. 19-25.
45. Springer, V., et al., *[Noninvasive analysis of cartilage volume and cartilage thickness in the human elbow joint using MRI]*. Ann Anat, 1998. **180**(4): p. 331-8.
46. Naish, J.H., et al., *MR measurement of articular cartilage thickness distribution in the hip*. Osteoarthritis Cartilage, 2006. **14**(10): p. 967-73.

47. Adam, C., et al., *The distribution of cartilage thickness within the joints of the lower limb of elderly individuals*. J Anat, 1998. **193 (Pt 2)**: p. 203-14.
48. Goldsmith, A.A., A. Hayes, and S.E. Clift, *Application of finite elements to the stress analysis of articular cartilage*. Med Eng Phys, 1996. **18(2)**: p. 89-98.
49. Elmore, S.M., et al., *Nature of "imperfect" elasticity of articular cartilage*. J of Appl Physiol, 1963. **18(2)**: p. 393-6.
50. Sokoloff, L., *Elasticity of aging cartilage*. Fed Proc, 1966. **25(3)**: p. 1089-95.
51. Kempson, G.E., M.A. Freeman, and S.A. Swanson, *The determination of a creep modulus for articular cartilage from indentation tests of the human femoral head*. J Biomech, 1971. **4(4)**: p. 239-50.
52. Hori, R.Y. and L.F. Mockros, *Indentation tests of human articular cartilage*. J Biomech, 1976. **9(4)**: p. 259-68.
53. Hayes, W.C. and L.F. Mockros, *Viscoelastic properties of human articular cartilage*. J Appl Physiol, 1971. **31(4)**: p. 562-8.
54. Parsons, J.R. and J. Black, *The viscoelastic shear behavior of normal rabbit articular cartilage*. J Biomech, 1977. **10(1)**: p. 21-9.
55. Mow, V.C., et al., *Biphasic creep and stress relaxation of articular cartilage in compression: Theory and experiments*. J Biomech Eng, 1980. **102(1)**: p. 73-84.
56. McCutchen, C.W., *Cartilage is poroelastic, not viscoelastic (including an exact theorem about strain energy and viscous loss, and an order of magnitude relation for equilibration time)*. J Biomech, 1982. **15(4)**: p. 325-7.
57. Bachrach, N.M., V.C. Mow, and F. Guilak, *Incompressibility of the solid matrix of articular cartilage under high hydrostatic pressures*. J Biomech, 1998. **31(5)**: p. 445-51.
58. Van C. Mow, R.H., *Basic orthopaedic biomechanics and mechano-biology*. 3rd ed. 2005: Lippincott Williams & Wilkins: Philadelphia. 720.
59. Kennedy, J.C., et al., *Tension studies of human knee ligaments. Yield point, ultimate failure, and disruption of the cruciate and tibial collateral ligaments*. J Bone Joint Surg Am, 1976. **58(3)**: p. 350-5.
60. Broberg, M.A. and B.F. Morrey, *Results of treatment of fracture-dislocations of the elbow*. Clin Orthop Relat Res, 1987(216): p. 109-19.
61. Herbertsson, P., et al., *Uncomplicated Mason type-II and III fractures of the radial head and neck in adults. A long-term follow-up study*. J Bone Joint Surg Am, 2004. **86-A(3)**: p. 569-74.

62. Akesson, T., et al., *Primary nonoperative treatment of moderately displaced two-part fractures of the radial head*. J Bone Joint Surg Am, 2006. **88**(9): p. 1909-14.
63. Burkhart, K.J., et al., *Stability of radial head and neck fractures: a biomechanical study of six fixation constructs with consideration of three locking plates*. J Hand Surg [Am], 2007. **32**(10): p. 1569-75.
64. Pike, J.M., et al., *Radial head fractures--an update*. J Hand Surg Am, 2009. **34**(3): p. 557-65.
65. Beingessner, D.M., et al., *The effect of radial head excision and arthroplasty on elbow kinematics and stability*. J Bone Joint Surg Am, 2004. **86-A**(8): p. 1730-9.
66. Jensen, S.L., B.S. Olsen, and J.O. Sojbjerg, *Elbow joint kinematics after excision of the radial head*. J Shoulder Elbow Surg, 1999. **8**(3): p. 238-41.
67. King, G.J., D.C. Evans, and J.F. Kellam, *Open reduction and internal fixation of radial head fractures*. J Orthop Trauma, 1991. **5**(1): p. 21-8.
68. Ikeda, M., et al., *Open reduction and internal fixation of comminuted fractures of the radial head using low-profile mini-plates*. J Bone Joint Surg Br, 2003. **85**(7): p. 1040-4.
69. Boulas, H.J. and B.F. Morrey, *Biomechanical evaluation of the elbow following radial head fracture. Comparison of open reduction and internal fixation vs. excision, silastic replacement, and non-operative management*. Chir Main, 1998. **17**(4): p. 314-20.
70. Hotchkiss, R.N., *Displaced Fractures of the Radial Head: Internal Fixation or Excision?* J Am Acad Orthop Surg, 1997. **5**(1): p. 1-10.
71. Ring, D., J. Quintero, and J.B. Jupiter, *Open reduction and internal fixation of fractures of the radial head*. J Bone Joint Surg Am, 2002. **84-A**(10): p. 1811-5.
72. Speed, K., *Ferrule cups for the head of the radius*. Surg Gynecol Obstet, 1941. **73**: p. 845-850.
73. Key, J.A., *Treatment of fractures of the head and neck of the radius*. J Am Med Assoc, 1931. **96**: p. 101-4.
74. King, B.B., *Resection of the radial head and neck. An end-result study of thirteen cases*. J Bone Joint Surg, 1939. **21**: p. 839-57.
75. Newwirth, A.A., *Nonsplinting treatment of fractures of the elbow joint*. J Am Med Assoc, 1942. **12**: p. 971-2.
76. Sutro, C.J., *Regrowth of bone at the proximal end of the radius following resection in this region*. J Bone Joint Surg, 1935. **17**: p. 867-78.

77. Gupta, G.G., G. Lucas, and D.L. Hahn, *Biomechanical and computer analysis of radial head prostheses*. J Shoulder Elbow Surg, 1997. **6**(1): p. 37-48.
78. King, G.J., et al., *Metallic radial head arthroplasty improves valgus stability of the elbow*. Clin Orthop Relat Res, 1999(368): p. 114-25.
79. Pribyl, C.R., et al., *The effect of the radial head and prosthetic radial head replacement on resisting valgus stress at the elbow*. Orthopedics, 1986. **9**(5): p. 723-6.
80. Cherry, J.C., *Use of acrylic prosthesis in the treatment of fracture of the head of the radius*. J Bone Joint Surg, 1953. **35-B**: p. 70-1.
81. Dickey, L.E. and W.P. Barnes, Jr., *A Salvage Procedure for Certain Fractures of the Radial Head*. South Med J, 1964. **57**: p. 711-3.
82. Mackay, I., B. Fitzgerald, and J.H. Miller, *Silastic replacement of the head of the radius in trauma*. J Bone Joint Surg Br, 1979. **61-B**(4): p. 494-7.
83. Carn, R.M., et al., *Silicone rubber replacement of the severely fractured radial head*. Clin Orthop Relat Res, 1986(209): p. 259-69.
84. Stoffelen, D.V. and B.J. Holdsworth, *Excision or Silastic replacement for comminuted radial head fractures. A long-term follow-up*. Acta Orthop Belg, 1994. **60**(4): p. 402-7.
85. Dotzis, A., et al., *Comminuted fractures of the radial head treated by the Judet floating radial head prosthesis*. J Bone Joint Surg Br, 2006. **88**(6): p. 760-4.
86. Brinkman, J.M., et al., *Treatment of sequelae of radial head fractures with a bipolar radial head prosthesis: good outcome after 1-4 years follow-up in 11 patients*. Acta Orthop, 2005. **76**(6): p. 867-72.
87. Herald, J. and S. O'Driscoll, *Complete dissociation of a bipolar radial head prosthesis: a case report*. J Shoulder Elbow Surg, 2008. **17**(6): p. e22-3.
88. Popovic, N., et al., *Midterm results with a bipolar radial head prosthesis: radiographic evidence of loosening at the bone-cement interface*. J Bone Joint Surg Am, 2007. **89**(11): p. 2469-76.
89. Gabrion, A., et al., *[Recent fractures of the radial head associated with elbow instability treated with floating Judet prosthesis]*. Rev Chir Orthop Reparatrice Appar Mot, 2005. **91**(5): p. 407-14.
90. Moon, J.G., et al., *Radiocapitellar joint stability with bipolar versus monopolar radial head prostheses*. J Shoulder Elbow Surg, 2009. **18**(5): p. 779-84.
91. Courant, R., *Variational methods for the solution of problems of equilibrium and vibrations*. Bulletin of the American Mathematical Society, 1943. **49**: p. 1-23.

92. Brekelmans, W.A., H.W. Poort, and T.J. Slooff, *A new method to analyse the mechanical behaviour of skeletal parts*. Acta Orthop Scand, 1972. **43**(5): p. 301-17.
93. Afoke, N.Y., P.D. Byers, and W.C. Hutton, *Contact pressures in the human hip joint*. J Bone Joint Surg Br, 1987. **69**(4): p. 536-41.
94. Haut, R.C., *Contact pressures in the patellofemoral joint during impact loading on the human flexed knee*. J Orthop Res, 1989. **7**(2): p. 272-80.
95. Hehne, H.J., et al., [*A new method for the determination of the weight-dependent course of pressure and contact in the articular surface*]. Morphol Med, 1981. **1**(2): p. 95-106.
96. Fukubayashi, T. and H. Kurosawa, *The contact area and pressure distribution pattern of the knee. A study of normal and osteoarthrotic knee joints*. Acta Orthop Scand, 1980. **51**(6): p. 871-9.
97. Werner, F.W., D.J. Murphy, and A.K. Palmer, *Pressures in the distal radioulnar joint: effect of surgical procedures used for Kienbock's disease*. J Orthop Res, 1989. **7**(3): p. 445-50.
98. Merz, B., et al., *Mechanical implications of humero-ulnar incongruity--finite element analysis and experiment*. J Biomech, 1997. **30**(7): p. 713-21.
99. Miyanaga, Y., T. Fukubayashi, and H. Kurosawa, *Contact study of the hip joint. Load-deformation pattern, contact area and contact pressure*. Arch Orthop Trauma Surg, 1984. **103**(1): p. 13-7.
100. Wang, C.L., et al., *Contact areas and pressure distributions in the subtalar joint*. J Biomech, 1995. **28**(3): p. 269-79.
101. Takatori, K., et al., *Analysis of stress distribution in the humeroradial joint*. J Orthop Sci, 2002. **7**(6): p. 650-7.
102. Chantelot, C., et al., *Intra-articular compressive stress of the elbow joint in extension: an experimental study using Fuji films*. Surg Radiol Anat, 2008. **30**(2): p. 103-11.
103. Diab, M., et al., *The biomechanical effect of radial shortening on the radiocapitellar articulation*. J Bone Joint Surg Br, 2005. **87**(6): p. 879-83.
104. Mounghondo, F., et al., *Radiocapitellar joint contacts after bipolar radial head arthroplasty*. J Shoulder Elbow Surg, 2010. **19**(2): p. 230-5.
105. Liew, V.S., et al., *The effect of metallic radial head arthroplasty on radiocapitellar joint contact area*. Clin Biomech (Bristol, Avon), 2003. **18**(2): p. 115-8.
106. Sabo, M.T., et al., *The impact of capitellar arthroplasty on elbow contact mechanics: Implications for implant design*. Clin Biomech (Bristol, Avon), 2011. **26**(5): p. 458-63.

107. Van Glabbeek, F., et al., *Detrimental effects of overstuffing or understuffing with a radial head replacement in the medial collateral-ligament deficient elbow*. J Bone Joint Surg Am, 2004. **86-A**(12): p. 2629-35.
108. Doornberg, J.N., et al., *Radial head arthroplasty with a modular metal spacer to treat acute traumatic elbow instability*. J Bone Joint Surg Am, 2007. **89**(5): p. 1075-80.
109. Grewal, R., et al., *Comminuted radial head fractures treated with a modular metallic radial head arthroplasty. Study of outcomes*. J Bone Joint Surg Am, 2006. **88**(10): p. 2192-200.
110. Pomianowski, S., et al., *Contribution of monoblock and bipolar radial head prostheses to valgus stability of the elbow*. J Bone Joint Surg Am, 2001. **83-A**(12): p. 1829-34.
111. Lim, Y.J. and B.K. Chan, *Short-term to medium-term outcomes of cemented Vitallium radial head prostheses after early excision for radial head fractures*. J Shoulder Elbow Surg, 2008. **17**(2): p. 307-12.
112. Chien, H.Y., et al., *Short- to medium-term outcomes of radial head replacement arthroplasty in posttraumatic unstable elbows: 20 to 70 months follow-up*. Chang Gung Med J, 2010. **33**(6): p. 668-78.
113. Burkhart, K.J., et al., *Mid- to long-term results after bipolar radial head arthroplasty*. J Shoulder Elbow Surg, 2010. **19**(7): p. 965-72.
114. Huiskes, R., et al., *Interface stresses in the resurfaced hip. Finite element analysis of load transmission in the femoral head*. Acta Orthop Scand, 1985. **56**(6): p. 474-8.
115. Rappoport, D.J., D.R. Carter, and D.J. Schurman, *Contact finite element stress analysis of the hip joint*. J Orthop Res, 1985. **3**(4): p. 435-46.
116. Hopkins, A.R., et al., *Finite element analysis of unicompartmental knee arthroplasty*. Med Eng Phys, 2010. **32**(1): p. 14-21.
117. Wake, H., et al., *Biomechanical analysis of the mechanism of elbow fracture-dislocations by compression force*. J Orthop Sci, 2004. **9**(1): p. 44-50.
118. Tarnita, D., et al., *The three-dimensional modeling of the complex virtual human elbow joint*. Rom J Morphol Embryol, 2010. **51**(3): p. 489-95.
119. Simon, W.H., *Scale effects in animal joints. I. Articular cartilage thickness and compressive stress*. Arthritis Rheum, 1970. **13**(3): p. 244-56.
120. Ateshian, G.A., L.J. Soslowsky, and V.C. Mow, *Quantitation of articular surface topography and cartilage thickness in knee joints using stereophotogrammetry*. J Biomech, 1991. **24**(8): p. 761-76.

121. von Eisenhart, R., et al., *Quantitative determination of joint incongruity and pressure distribution during simulated gait and cartilage thickness in the human hip joint*. J Orthop Res, 1999. **17**(4): p. 532-9.
122. Jeffrey, D.R. and I. Watt, *Imaging hyaline cartilage*. Br J Radiol, 2003. **76**(911): p. 777-87.
123. Pena, E., et al., *A three-dimensional finite element analysis of the combined behavior of ligaments and menisci in the healthy human knee joint*. J Biomech, 2006. **39**(9): p. 1686-701.
124. Gislason, M.K., B. Stansfield, and D.H. Nash, *Finite element model creation and stability considerations of complex biological articulation: The human wrist joint*. Med Eng Phys, 2010. **32**(5): p. 523-31.
125. Harris, M.D., et al., *Finite element prediction of cartilage contact stresses in normal human hips*. J Orthop Res, 2012. **30**(7): p. 1133-9.
126. Regan, W.D., et al., *Biomechanical study of ligaments around the elbow joint*. Clin Orthop Relat Res, 1991(271): p. 170-9.
127. Goel, V.K., D. Singh, and V. Bijlani, *Contact areas in human elbow joints*. J Biomech Eng, 1982. **104**(3): p. 169-75.
128. Stormont, T.J., et al., *Elbow joint contact study: comparison of techniques*. J Biomech, 1985. **18**(5): p. 329-36.
129. Hojjatie, B. and K.J. Anusavice, *Three-dimensional finite element analysis of glass-ceramic dental crowns*. J Biomech, 1990. **23**(11): p. 1157-66.
130. Muriuki, M.G., L.G. Gilbertson, and C.D. Harner, *Characterization of the performance of a custom program for image processing of pressure sensitive film*. J Biomech Eng, 2009. **131**(1): p. 014503.
131. Hale, J.E. and T.D. Brown, *Contact stress gradient detection limits of Pressensor film*. J Biomech Eng, 1992. **114**(3): p. 352-7.
132. Wu, J.Z., W. Herzog, and M. Epstein, *Effects of inserting a pressensor film into articular joints on the actual contact mechanics*. J Biomech Eng, 1998. **120**(5): p. 655-9.
133. Liao, J.J., et al., *The influence of inserting a Fuji pressure sensitive film between the tibiofemoral joint of knee prosthesis on actual contact characteristics*. Clin Biomech (Bristol, Avon), 2001. **16**(2): p. 160-6.
134. Liao, J.J., et al., *Effect of Fuji pressure sensitive film on actual contact characteristics of artificial tibiofemoral joint*. Clin Biomech (Bristol, Avon), 2002. **17**(9-10): p. 698-704.

135. Ateshian, G.A., et al., *A stereophotogrammetric method for determining in situ contact areas in diarthrodial joints, and a comparison with other methods.* J Biomech, 1994. **27**(1): p. 111-24.
136. Szivek, J.A., L. Cutignola, and R.G. Volz, *Tibiofemoral contact stress and stress distribution evaluation of total knee arthroplasties.* J Arthroplasty, 1995. **10**(4): p. 480-91.
137. Stewart, T., et al., *Experimental and theoretical study of the contact mechanics of five total knee joint replacements.* Proc Inst Mech Eng H, 1995. **209**(4): p. 225-31.
138. Harris, M.L., et al., *An improved method for measuring tibiofemoral contact areas in total knee arthroplasty: a comparison of K-scan sensor and Fuji film.* J Biomech, 1999. **32**(9): p. 951-8.
139. Buchler, P., et al., *A finite element model of the shoulder: application to the comparison of normal and osteoarthritic joints.* Clin Biomech (Bristol, Avon), 2002. **17**(9-10): p. 630-9.
140. Anderson, A.E., et al., *Validation of finite element predictions of cartilage contact pressure in the human hip joint.* J Biomech Eng, 2008. **130**(5): p. 051008.
141. Katchky, R.N., Johnson, J.A., King, G.J., and Athwal, G.S., *Anatomic radial head arthroplasty: A lack of reliable landmarks for alignment.* 2011: p. 164-165.
142. Repo, R.U. and J.B. Finlay, *Survival of articular cartilage after controlled impact.* J Bone Joint Surg Am, 1977. **59**(8): p. 1068-76.
143. Torzilli, P.A., et al., *Effect of impact load on articular cartilage: cell metabolism and viability, and matrix water content.* J Biomech Eng, 1999. **121**(5): p. 433-41.
144. Ewers, B.J., et al., *The extent of matrix damage and chondrocyte death in mechanically traumatized articular cartilage explants depends on rate of loading.* J Orthop Res, 2001. **19**(5): p. 779-84.
145. Quinn, T.M., et al., *Matrix and cell injury due to sub-impact loading of adult bovine articular cartilage explants: effects of strain rate and peak stress.* J Orthop Res, 2001. **19**(2): p. 242-9.
146. Chen, C.T., et al., *Chondrocyte necrosis and apoptosis in impact damaged articular cartilage.* J Orthop Res, 2001. **19**(4): p. 703-11.
147. Levin, A., et al., *Intercellular signaling as a cause of cell death in cyclically impacted cartilage explants.* Osteoarthritis Cartilage, 2001. **9**(8): p. 702-11.
148. Loening, A.M., et al., *Injurious mechanical compression of bovine articular cartilage induces chondrocyte apoptosis.* Arch Biochem Biophys, 2000. **381**(2): p. 205-12.